

**Towards the Industrial Application  
of  
Spark Ablation  
for  
Nanostructured Functional Materials**

**Proefschrift**

ter verkrijging van de graad van doctor  
aan de Technische Universiteit Delft,  
op gezag van de Rector Magnificus Prof. ir. K. Ch. A. M. Luyben,  
voorzitter van het College voor Promoties,  
in het openbaar te verdedigen op maandag 13 oktober 2014 om 15:00 uur

door

Tobias Vincent PFEIFFER

Scheikundig ingenieur  
geboren te Neuchâtel, Zwitserland

Dit proefschrift is goedgekeurd door de promotor:

Prof. dr. A. Schmidt-Ott

Samenstelling promotiecommissie:

Rector Magnificus	Technische Universiteit Delft, voorzitter
Prof. dr. A. Schmidt-Ott	Technische Universiteit Delft, promotor
Prof. dr. K. Deppert	Lund University
dr. S. W. H. Eijt	Technische Universiteit Delft
apl. Prof. Dr.-Ing. E. Kruis	Universität Duisburg-Essen
Prof. dr. F. M. Mulder	Technische Universiteit Delft
Prof. Dr.-Ing. habil L. Mädler	IWT Bremen
Prof. dr. A. Züttel	EMPA Materials Science and Technology
Prof. dr. S. J. Picken	Technische Universiteit Delft, reservelid

© T. V. Pfeiffer, 2014.

Cover artwork © F. Oikonomopoulou & T. V. Pfeiffer, 2014.

ISBN 978-94-6186-373-7

All rights reserved. The author encourages the communication of scientific contents and explicitly allows reproduction for scientific, non-commercial purposes, provided the proper citation of the source. Parts of the thesis are published in scientific journals and copyright is subject to different terms and conditions.

voor Ernst



## Abstract

Nanostructuring of functional materials is an essential part in the design of energy related devices – but the industrial tools we have to make these materials are lacking. This dissertation explores the green, flexible, and scalable spark discharge process for the fabrication of complex nanostructured materials, and the application of said materials in energy devices.

A novel spark generator concept with a 60-fold increased mass production rate was developed, where spark energy and spark repetition rate have been decoupled from gas and material properties. The application of spark discharge materials in two types of energy storage and conversion devices was studied: amorphous-Si photovoltaic cells,  $\text{MgH}_2$ -based hydrogen storage. The possibility of using spark discharge to functionalize nanoparticles with metal coatings was investigated using two spark generators in series.

The new spark generator provides true scaling: it produces materials identical to that of the old designs, and the mass production rate – about a gram per day – scales linearly with the spark repetition rate. Arrays of  $\sim 100$  nm high-purity silver nanospheres were deposited as scattering agents in solar cells, improving their external quantum efficiency by 30%. A method for synthesizing  $\text{MgH}_2$  nanoparticles was developed, which show promising hydrogen storage properties. Nanocomposites of Mg with  $\text{NbO}_x$  catalyst nanoparticles were synthesized using two sparks in series, increasing the  $\text{H}_2$  desorption rate of  $\text{MgH}_2$ . Using a hollow electrode spark, 40 nm gold nanoparticles were coated with silver, and *vice versa*.

The possibility to make useful quantities of high-quality nanomaterials – e.g. high-purity metals or light metal hydrides – from nearly any element makes spark discharge a powerful tool in materials design. The new spark generator provides sufficient quantities to make it economical to develop an industrial nanoparticle facility using multiple sparks in parallel.



# Contents

List of Figures . . . . .	x
List of Tables . . . . .	xiii
List of Symbols . . . . .	xv
<b>1 Introduction</b>	<b>1</b>
1.1 Energy needs . . . . .	2
1.2 Energy use: Transportation . . . . .	2
1.3 Nanostructured functional materials . . . . .	4
1.4 It starts with a spark . . . . .	5
1.5 Nanoparticle production by spark discharge . . . . .	7
1.6 Scope of this thesis . . . . .	10
<b>2 Design of a 25 kHz Spark Generator</b>	<b>11</b>
2.1 Introduction . . . . .	12
2.1.1 Spark discharge generators . . . . .	12
2.1.2 Design concept . . . . .	13
2.2 Theory . . . . .	14
2.2.1 Gas discharges and breakdown . . . . .	14
2.2.2 Spark generators . . . . .	17
2.3 Experimental . . . . .	19
2.3.1 New power supply . . . . .	19
2.3.2 Reactor . . . . .	23
2.3.3 Measurements . . . . .	23
2.4 Results and Discussion . . . . .	25
2.4.1 Plasma ignition . . . . .	26
2.4.2 Formative time lag . . . . .	27
2.4.3 Glow discharge . . . . .	29
2.4.4 Spark energy . . . . .	31
2.4.5 Power dissipation . . . . .	33

2.5	Conclusion . . . . .	34
<b>3</b>	<b>Nanoparticles from a 25 kHz Spark Generator</b>	<b>37</b>
3.1	Introduction . . . . .	38
3.2	Theory . . . . .	38
3.3	Experimental . . . . .	43
3.4	Results . . . . .	44
3.5	Discussion . . . . .	47
	3.5.1 Electrode melting . . . . .	47
	3.5.2 Oxidation . . . . .	48
3.6	Conclusion . . . . .	49
<b>4</b>	<b>Plasmonic Ag nanospheres in Solar Cells</b>	<b>51</b>
4.1	Introduction . . . . .	52
4.2	Experimental . . . . .	53
	4.2.1 Deposition of Ag nanoparticles . . . . .	53
	4.2.2 Thin-film solar cells . . . . .	54
	4.2.3 Characterization . . . . .	55
4.3	Results . . . . .	56
	4.3.1 Aerosol production . . . . .	56
	4.3.2 Films of deposited Ag nanospheres . . . . .	57
	4.3.3 Economic evaluation . . . . .	62
	4.3.4 Optical properties . . . . .	63
	4.3.5 Solar cells . . . . .	65
4.4	Conclusions . . . . .	68
<b>5</b>	<b>Synthesis of MgH<sub>2</sub> by Spark Discharge</b>	<b>71</b>
5.1	Introduction . . . . .	72
5.2	Theory . . . . .	73
5.3	Experimental . . . . .	75
	5.3.1 Synthesis . . . . .	75
	5.3.2 Characterization . . . . .	76
5.4	Results . . . . .	76
	5.4.1 Production Rate and Yield . . . . .	76
	5.4.2 Mobility measurements . . . . .	78
	5.4.3 Morphology and Structure . . . . .	79
	5.4.4 Hydrogen content . . . . .	86
5.5	Discussion . . . . .	88
	5.5.1 Particle charging . . . . .	88

5.5.2	Structural Characterization . . . . .	89
5.5.3	Production Rate and Yield . . . . .	90
5.5.4	Hydride formation . . . . .	92
5.6	Conclusion . . . . .	94
<b>6</b>	<b>Nanoscale Dispersion of Nb and NbO<sub>x</sub> in Mg</b>	<b>95</b>
6.1	Introduction . . . . .	96
6.2	Theory . . . . .	96
6.3	Experimental . . . . .	99
6.4	Results and discussion . . . . .	101
6.4.1	Electrostatic losses . . . . .	101
6.4.2	Bulk composition . . . . .	102
6.4.3	Local composition - catalyst distribution . . . . .	107
6.4.4	Hydrogen storage properties . . . . .	109
6.5	Conclusions . . . . .	110
<b>7</b>	<b>Coating by Spark Discharge</b>	<b>111</b>
7.1	Introduction . . . . .	112
7.2	Theory . . . . .	114
7.2.1	Smoluchowski Coagulation . . . . .	114
7.2.2	Coalescence of Metal Nanoparticles . . . . .	115
7.2.3	Coating model . . . . .	116
7.3	Experimental . . . . .	119
7.3.1	Coating setup . . . . .	119
7.3.2	Characterization . . . . .	120
7.4	Results . . . . .	120
7.4.1	Coating model . . . . .	120
7.4.2	Au on PSL . . . . .	122
7.4.3	Au on Ag . . . . .	125
7.4.4	Ag on Au . . . . .	127
7.4.5	Raman spectroscopy . . . . .	129
7.5	Discussion . . . . .	130
7.6	Conclusion . . . . .	132
	<b>Bibliography</b>	<b>133</b>
	<b>Samenvatting</b>	<b>149</b>
	<b>Summary</b>	<b>155</b>

<b>Acknowledgments</b>	<b>159</b>
<b>Curriculum Vitae</b>	<b>163</b>

# List of Figures

1.1	Classic spark circuit. . . . .	6
1.2	Schematic overview of processes in a developing spark. . . . .	7
1.3	Particle formation mechanisms in spark discharge. . . . .	8
1.4	Metal clusters from a spark generator. . . . .	9
1.5	Three approaches to atomic mixing in spark discharge. . . . .	10
2.1	The spark as an RLC circuit. (a) Spark generator circuit. (b) Current and voltage traces of a spark discharge [30] . . . . .	17
2.2	Capacitor voltage vs. time. . . . .	18
2.3	Spark circuit with decoupled charging cycles. . . . .	18
2.4	Internal structure of generic Power MOSFET and IGBT. . . . .	20
2.5	Spark topology using three high voltage switches. . . . .	21
2.6	Expanded circuit with a pulled up cathode. . . . .	22
2.7	Timing sequence of switches from Figure 2.6 . . . . .	23
2.8	Spark generator prototype. (a) Generator with top removed, (b) View of sparks between two electrodes. . . . .	24
2.9	Oscilloscope traces for a typical spark event. . . . .	25
2.10	Current-voltage characteristic of the circuit with a resistive load or a spark gap. . . . .	26
2.11	Ignition of a spark at $f_{\text{rep}} = 1$ kHz. . . . .	27
2.12	Current onset delay or formative time lag for different gap spacings at 1.5 kV in Ar. . . . .	28
2.13	Current and voltage traces of the glow regime: capacitive discharges and glow discharge. . . . .	29
2.14	A single microdischarge, 0.5 mm gap in Ar. . . . .	30
2.15	Decay of $U_{\text{cathode}}$ for 20 sequential discharges. . . . .	31
2.16	$E_{\text{SG}}$ during discharge for several gap spacings. . . . .	32
2.17	Oscilloscope traces at $f_{\text{rep}} = 17$ kHz. . . . .	33

3.1	Flow focussing using an orifice . . . . .	40
3.2	Flow requirements for independent sparks. . . . .	41
3.3	Process schematic of the closed loop spark generator. . . . .	43
3.4	Optical micrographs of Nb cathodes after use in Ar. . . . .	45
3.5	XRD of nanoparticles produced from Nb rods. . . . .	45
3.6	TEM micrographs of NbO <sub>x</sub> . . . . .	46
4.1	Calculated extinction efficiencies for Ag nanoparticles in TCO. . . . .	52
4.2	Schematic of the experimental setup. . . . .	54
4.3	Solar cell configuration. . . . .	55
4.4	Mobility size distributions of furnace- and spark-generated Ag. . . . .	57
4.5	SEM micrographs for different deposition times. . . . .	58
4.6	Deposited Ag nanoparticles produced by spark discharge. . . . .	59
4.7	Measured scattering and absorption of spark Ag nanoparticles. . . . .	64
4.8	Simulated scattering of Ag particles with an Ag <sub>2</sub> S shell. . . . .	65
4.9	Age effect in scattering and absorption of Ag nanoparticles. . . . .	66
4.10	Wavelength dependent performance of single junction solar cells. . . . .	67
4.11	<i>JV</i> -curves of the assembled cells. . . . .	67
5.1	Experimental setup. . . . .	75
5.2	Power input and yield vs. H <sub>2</sub> concentration . . . . .	77
5.3	Self-charging in 100 % Ar. . . . .	78
5.4	Mobility size distributions for various H <sub>2</sub> concentrations. . . . .	80
5.5	TEM micrographs of spark-generated MgH <sub>x</sub> . . . . .	81
5.6	Electron diffraction pattern for MgH <sub>2</sub> . . . . .	81
5.7	XRD for various H <sub>2</sub> concentrations. . . . .	83
5.8	Rietveld refinement results of MgH <sub>2</sub> . . . . .	84
5.9	IR transmission spectrum for MgH <sub>2</sub> . . . . .	85
5.10	Thermal desorption spectrum of MgH <sub>2</sub> . . . . .	87
6.1	Schematic process of catalyst addition. . . . .	97
6.2	Capacitor voltage vs. time for classic and pulsed operation mode. . . . .	98
6.3	Schematic of the double spark generator. . . . .	99
6.4	Effect of pulsing the Nb spark on the size distributions of positively self-charged agglomerates. . . . .	102
6.5	Mass ratio of Nb to Mg vs. relative power input. . . . .	103
6.6	XRD pattern of Mg + Nb composite. . . . .	104
6.7	Normalized XRD pattern of Mg + Nb composite before and after hydrogen ab- and desorption. . . . .	105

6.8	TEM images of Mg-Nb composites. . . . .	107
6.9	Elemental composition of Mg-Nb agglomerates by TEM/EDX. .	108
6.10	Normalized hydrogen desorption of spark-generated MgH <sub>2</sub> with Nb and Pd catalyst. . . . .	109
7.1	Schematic of the coating procedure using a hollow spark. . . .	117
7.2	Process schematic including substrate particle generation, particle coating, and size selection and collection. . . . .	119
7.3	Normalized $K_{12}$ vs. relative particle size. . . . .	121
7.4	Results of coagulation model. . . . .	122
7.5	TEM micrographs of gold-decorated PSL spheres. . . . .	123
7.6	Au clusters and agglomerates on carbon foil. . . . .	124
7.7	Other observed structures. . . . .	124
7.8	TEM Size distribution of Au-coated Ag nanoparticles. . . . .	125
7.9	HRTEM micrographs of Au-coated Ag nanoparticles. . . . .	126
7.10	TEM micrographs of Ag-coated Au-core nanoparticles. . . . .	127
7.11	TEM micrographs of the Ag-coating on Au nanoparticles. . . .	128
7.12	Raman spectra for Au-coated Ag and vice versa. . . . .	129



# List of Tables

2.1	Reference conditions for spark discharge. . . . .	14
2.2	Properties of dielectric gases . . . . .	16
3.1	Production runs with niobium . . . . .	44
4.1	Molar composition of Ag nanoparticles. . . . .	60
4.2	Summary of solar cell parameters. . . . .	68
5.1	Scherrer crystallite sizes . . . . .	82
5.2	Mass fractions in % m/m as determined by Rietveld analysis. . . . .	82
5.3	Initial hydrogen content determined by TDS. See text. . . . .	86
5.4	Equilibrium temperatures of selected metal hydrides. . . . .	93
6.1	Operating conditions, ICP and EDX for Mg + Nb sparks. . . . .	100
6.2	Results of Rietveld analysis. . . . .	105
7.1	Interface energies of Ag and Au . . . . .	116



# List of Symbols

## Lower case symbols

$d_p$	Particle diameter	m
$d_{\text{gap}}$	Gap distance between electrodes	m
$e$	Elementary charge	$1.6022 \times 10^{-19} \text{ C}$
$f_{\text{rep}}$	Repetition rate of sparks	Hz
$f_{\text{spark}}$	Frequency of an oscillating spark discharge	Hz
$l$	Length (of tube, rod, etc.)	m
$m$	Mass (of particle)	kg
$n$	Molar concentration	$\text{m}^3$
$n_e$	Electron concentration	$\text{m}^{-1}$
$p$	Pressure	Pa
$r$	Radius	m
$t$	Time or duration of an event	s
$\bar{v}$	Mean (thermal) velocity	$\text{m s}^{-1}$
$x$	Length or thickness	m

## Upper case symbols

$C$	Capacitance	F
$D$	Diffusion coefficient	$\text{m}^2 \text{ s}^{-1}$

$D_f$	Fractal dimension	-
$E$	Energy	J
$E$	Electric field	$\text{V m}^{-1}$
$E_b$	Dielectric strength	$\text{V m}^{-1}$
$E_C$	Energy stored in capacitor	J
$E_L$	Energy stored in inductor	J
$I$	Current	A
$K$	Coagulation kernel	$\text{m}^3 \text{s}^{-1}$
$L$	Inductance	H
$M$	Molar mass	$\text{kg mol}^{-1}$
$N$	Particle number concentration	$\text{m}^3$
$N_A$	Avogadro's constant	$6.022 \times 10^{23} \text{ mol}^{-1}$
$N_{pp}$	Number of primary particles	-
$\mathbb{P}$	Penetration of particles through a tube	-
$P$	Power	W
$Q$	Volumetric flow rate	$\text{m}^3 \text{s}^{-1}$
$R$	Resistance	$\Omega$
$R_g$	Radius of gyration	m
$T_e$	Electron temperature	K
$U$	Electric potential	V
$U_b$	Breakdown voltage	V
$U_d$	Voltage at which a specific discharge formed	V
$U_C$	Potential difference over capacitor	V
$V$	Volume	$\text{m}^3$

## Greek symbols

$\gamma$	Surface tension or surface free energy	$\text{J m}^{-2}$ eV
$\kappa$	$K_{\text{continuum}}/K_{\text{free molecular}}$	-
$\rho$	Specific density	$\text{kg m}^{-3}$
$\sigma$	Conductivity	$\Omega^{-1} \text{m}^{-1}$
$\sigma_g$	Geometric standard deviation	-
$\tau_f$	Formative time lag	s

*Unless explicitly noted otherwise, values are reported under standard conditions, i.e.  $p = 101\,325 \text{ Pa}$  and  $T = 293.15 \text{ K}$ , and the term particle size refers to the diameter of the volume-equivalent sphere of said particle.*



# Chapter 1

## Introduction

**N**ANOSTRUCTURING ENABLES US to engineer novel functional materials that can help us supply our energy demands from renewable sources. The global energy demand is however huge, and novel solutions must not only provide materials of high quality, but also in large quantity.

Spark discharge allows the synthesis of novel phases and composites, using nothing but two metal rods and electrical power. The aerosol method uses no solvents, surfactants, or precursors; all sources of contaminants and pollution.

The particles form by a coagulation process, allowing the production of spherical particles from 1 to 100 nm, and agglomerated structures thereof. At every stage of the growth the particles can be manipulated, mixed and modified while suspended in a gas. This makes it possible to produce composite materials where the distribution of the constituents can be controlled down to atomic length scales.

This chapter describes recent work on spark discharge, and provides a context for an attempt to develop new materials, and to scale up their production.

---

Parts of this chapter are based on T. V. Pfeiffer, J. Feng, and A. Schmidt-Ott “New developments in spark production of nanoparticles” *Advanced Powder Technology* (2014), **25**, 56-70.

## 1.1 Energy needs

The global annual energy use in 2010 was  $5.5 \times 10^{20}$  J, and is expected to grow to  $8.7 \times 10^{20}$  J by 2040 [1]. This is equivalent to a mean power use of  $2.7 \times 10^{13}$  W. The sources we can turn to are the sun, the tides, the internal heat of the earth, and nuclear power, of which the sun is by far the most bountiful.  $1.2 \times 10^{17}$  W of sunlight penetrates the upper atmosphere [2], most of which is used to keep us warm<sup>1</sup>. Hence, an overall conversion efficiency of 0.02% will suffice to sustainably feed our energy need for decades to come.

Sequestered sunlight, commonly referred to as fossil fuel, currently makes up  $\sim 80\%$  of our energy use [1]. And while new reserves are regularly discovered, fossil fuels are depleted faster than they form, making them a finite resource. To complicate matters, their use leads to the production of carbon dioxide, which is intricately linked with the globe's energy balance, often together with other harmful compounds and particulates. Replacing a significant part of these finite fuels with renewable sources should be the primary target in securing energy security.

The challenge lies in the broad range of energy uses. The fuel can be solid (coal, cokes), liquid (oil), or gaseous (natural gas), and varies in composition from source to source. The chemical energy stored within these fuels is directly converted into heat or kinetic energy, which in turn can be used to generate electricity. The reactors used to execute this conversion range in scale from  $10^{-6}$  to  $10^3$  m<sup>3</sup>, and comprise countless technologies. Clearly, no one-size-fits-all solution for a switch to renewables can exist. For now, we shall limit ourselves to one example energy use: the transportation of people.

## 1.2 Energy use: Transportation

Of the six primary modes of transport (foot, bicycle, automobile, tram/train, boat, airplane), the automobile warrants special attention. Not only is the energy efficiency poor ( $\sim \frac{1}{10}$ -th of a bicycle), their ground level emissions present a direct health hazard to those using more efficient modes of transport, especially in urban areas. For this reason, replacing fossil fuels with sustainable 'biofuels', e.g. ethanol, vegetable oil, is a non-ideal solution.

Electric vehicles have two big advantages over the modern automobile. In addition to allowing the use of zero emission<sup>2</sup> energy sources, an elec-

---

<sup>1</sup>Or cold, in a windy country.

<sup>2</sup>At point of use.

tric motor has a much higher efficiency than an internal combustion engine (ICE). Modern electric vehicles have an overall energy consumption of  $3.7 \pm 0.7 \times 10^5 \text{ J km}^{-1}$ , five times less than a comparable diesel ICE vehicle ( $1.77 \times 10^6 \text{ J km}^{-1}$ ) [3]. By the end of 2013, Dutch roads counted  $3 \times 10^4$  electric vehicles, up from  $1.6 \times 10^3$  in 2011 [4]. The Dutch government has set a target to reach 1 million electric vehicles by 2025 [4]. To put this in perspective: 10 million motorized vehicles were registered in the Netherlands in 2013 [5].

In order to maintain a comparable action radius to ICE vehicles, our electric vehicle must carry  $\sim 2 \times 10^8 \text{ J}$  of electrical energy in its fully loaded ‘tank’. Li-ion based rechargeable batteries are the current state of the art. On a cell level, they can reach specific energy densities<sup>3</sup> of  $7.2 \times 10^5 \text{ J kg}^{-1}$ , resulting in a final battery weight of  $>290 \text{ kg}$ . Other battery technologies with higher energy densities are being developed, such as lithium-sulfur (up to  $2.3 \times 10^6 \text{ J kg}^{-1}$  [6]) or lithium-air ( $\sim 3.6 \times 10^6 \text{ J kg}^{-1}$  [7]). However, they still face significant challenges, and are far from commercialization.

An alternative solution, which has seen significant interest over the last decades, is the direct conversion of fuel to electricity in a so called fuel cell. This becomes worthwhile if the energy density of the fuel is large enough to compensate for the conversion loss in the fuel cell. As we’re keen to have no harmful emissions, we will limit our fuel options to hydrogen, which has water as its only combustion product. The advantage of hydrogen is its very high gravimetric energy density of  $1.2 \times 10^8 \text{ J kg}^{-1}$ . The disadvantage that it is a gas with a low boiling point, resulting in awkward handling and a low volumetric energy density. In order to fit in a typical car, the hydrogen is pressurized to 700 bar and/or cooled to cryogenic temperatures [8].

A better solution is to chemically or physically bind the hydrogen into a support matrix. Light metal/metal hydride systems are considered for use as hydrogen storage materials for a number of reasons: 1) high volumetric energy density, 2) acceptable mass energy density, and 3) safe storage [9]. Slow reaction rates, high temperature requirements, and problems with reversibility currently prohibit the use of these hydrogen storage systems in automotive applications.  $\text{MgH}_2$  has gained significant attention, on account of the abundance of Mg, the high hydrogen content of 7.66 % m/m, i.e.  $9 \times 10^6 \text{ J kg}^{-1}$ , and the relative simplicity of the hydrogen sorption reaction. The problem with  $\text{MgH}_2$  is that the material is too stable, resulting in low equilibrium pressures, and is slow to react due to poor hydrogen splitting performance.

---

<sup>3</sup>For sake of argument we’re ignoring specific power ( $\text{W kg}^{-1}$ ), which is equally important.

### 1.3 Nanostructured functional materials

A functional material is a material in which specific properties or functions have been deliberately designed or engineered. The properties and functions can be chemical, mechanical, magnetic, optical and electrical in nature, and are typically added in the form of chemical groups or nanoparticles of specific composition and shape, either on the surface or within the bulk of the material. As an example, we can add the missing hydrogen-splitting function to  $\text{MgH}_2$  by the addition of a suitable catalyst such as Pd [10]. Other examples of functional materials are anti-microbial polymers containing nanosilver [11], polymers made conductive by halogen doping [12] or by incorporating conductive carbon particles [13], but also a semiconductor with dopant-tunable band gap can be considered a functional material.

Generalizable methods of producing functional materials allow greater freedom in designing an actual device, as the range of properties of its constituent materials becomes limited only by the imagination of the material scientist. Functions are preferably added on a scale only slightly larger than the size of individual atoms and molecules, i.e.  $\sim 1$  nanometer, to ensure a homogeneous distribution, and to avoid the use of excess material.

In energy storage applications the main advantage of such nanostructured materials often is the strongly enhanced specific interface area. Large surface areas combined with short transport path lengths allow slow solid-state diffusion to be bypassed, allowing batteries to be operated at higher currents and higher power densities [14]. Hydrogen storage in metals, such as Mg, is accelerated by the reduced diffusion distances, especially when catalyst materials are included in the nanostructure [10]. Otherwise impossible solid-solid reactions become feasible, such as the hydrogenation of  $\text{NaH} + \text{Al}$  to form  $\text{NaAlH}_4$ , where the addition of  $\text{TiCl}_3$  leads to the formation of grain-refining nanocrystallites that keep the reactant domain sizes small [15]. Nanostructured semiconducting transition metal oxides form the basis for dye-sensitized solar cells [16]. Plasmonic metal nanoparticles incorporated in back reflectors of Si-based solar cells can trap light in solar cells, improving solar cell efficiency [17].

Nanostructured materials can be obtained through one of two approaches: top-down or bottom-up. In the first approach the nanostructured material is formed by reducing the size of a bulk material, e.g. by grinding down a solid. High-energy ball mills are used to induce nanocrystallinity in bulk powders. For larger scales rolling mills are attractive despite a lower milling intensity, as demonstrated by Lang and Huot [18] using 300 Mesh  $\text{MgH}_2$ . The ball-mill-

induced grain boundaries allow fast diffusion of hydrogen atoms through the ‘bulk’ of  $\text{MgH}_2$  microparticles, drastically increasing hydrogen ab- and desorption rates [19].

In the second approach, the nanostructured material is built up from the constituent atoms and molecules, e.g. by condensation or precipitation. This can be done in either the gas or the liquid phase.

Liquid phase methods provide highly monodisperse nanocrystals –ideal for use as quantum dots– through well-controlled nucleation-and-growth processes. Precursors, solvents and surfactants are however required, resulting in troublesome particle purification and large waste streams.

Waste streams can be greatly reduced when gas phase synthesis methods are used. Aerosol processes tend to be continuous, and conveniently allow in-line particle modification and size selection [20, 21]. Particles form either through decomposition or condensation of a gaseous substance, or through precipitation or reaction in aerosolized droplets. Liquid or soluble feedstocks are brought into the gas phase by spraying the liquid under pressure or under an electric field. Solid feedstocks are evaporated using e.g. heat, plasma or lasers.

## 1.4 It starts with a spark

A spark forms when a medium, typically a gas, is subjected to an electric field stronger than its dielectric field strength, and starts to ionize. If sufficient ionization occurs the medium becomes conductive and the formed plasma presents a short circuit, rapidly drawing energy from the external circuit. A plasma sustained by a continuous current supply, either AC or DC, is called an arc. When the current supplied is finite, e.g. a discharging capacitor or inductor, the plasma starts to decay as the ionization rate drops with decreasing current, and the lifetime of the channel is short. This last type of gas discharge is called a spark. Familiar examples of sparks are those formed by a spark plug in a combustion engine, and those formed between two people attempting to shake hands in a dry, carpeted office. When a highly charged cloud passes too close to a grounded object, such as a tree or a building, it will dissipate its charge through the air, forming a spark kilometers in length, better known as lightning.

Early radio transmitters used spark gaps to send broadband radio waves, with a circuit essentially identical to that used by Schwyn, Garwin, and Schmidt-Ott to make nanoparticles (Figure 1.1). A spark led Hertz to his discovery of

ultra-violet light [23]. Xenon flashtubes find application in photography, for their bright white light, and in laboratories, for their ultra-violet emissions. In high-voltage circuits a spark gap functions as a switch: in the ‘off’ state an insulating gas or vacuum prevents current from flowing, while in the ‘on’ state the spark plasma functions as a short circuit. The advantage of spark gap switches is the fast ignition of the plasma, which quickly develops a high current density of  $10^8 \text{ A m}^{-2}$  [24], even at blocking voltages of  $10^2 \text{ kV}$ . A significant body of research exists on spark discharges, mainly driven by needs from the field of electric power engineering [25, 26].

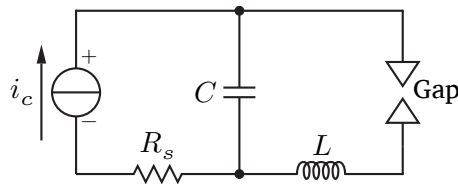


FIGURE 1.1 Classic spark circuit.

From a circuit point of view, the spark is a conductive channel between two otherwise insulated electrodes. The formation of this conductive channel can be explained through streamer theory [27]. Consecutive electron avalanches traveling from cathode to anode result in an increase in positive space charge around the anode (Figure 1.2). This space charge then attracts photoelectrons generated in its vicinity, and the space charge forms a self-propagating streamer traveling towards the cathode. Unlike the individual avalanches, this streamer is sufficiently conductive to form the conductive channel required for spark discharge. Space charge reduces the overall electric field, but enhances the field strength at the leader tip, allowing sparks to traverse long distances [25].

The current flowing through the gap heats up the gas through Joule heating. If the temperature in the gap reaches 7000 to 10 000 K thermal ionization becomes significant, and the resistivity of the channel rapidly drops down to  $<1 \Omega$  for small gaps [28]. The core temperature rises until it reaches a plateau temperature of  $2 \times 10^4$  to  $6 \times 10^4 \text{ K}$ , at which the point the plasma starts to expand in order to accommodate the increasing space charge [29]. This expansion causes the characteristic audible shockwave to which sparks owe their name.

Once the spark has formed, the energy in the storage capacitor is transferred into the spark gap through ionization processes and Joule heating. Part of the energy in the spark is dissipated in the form of light, both spectral lines

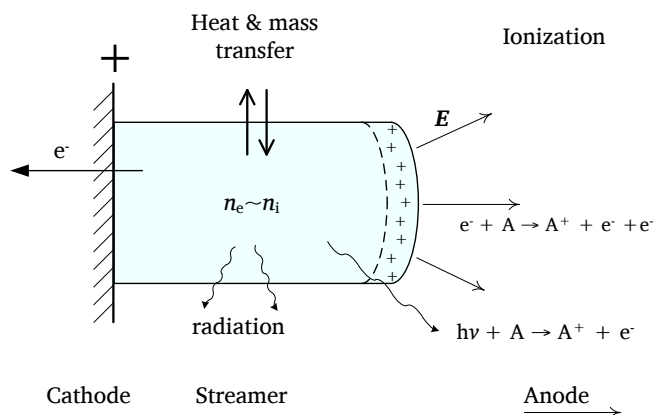


FIGURE 1.2 Schematic overview of processes in a developing spark, after [25].

of the used gas, and broad spectrum thermal radiation. Heat is transported away from the spark by conduction and convection. As the discharge starts cooling down due to these effects, it can die out before current drops to zero. This makes it possible to quench a spark or arc with a gas stream directed at the gap.

## 1.5 Nanoparticle production by spark discharge

Compared to other plasma based physical methods of producing nanoparticles, the distinguishing feature of the spark discharge is a repetition of short high energy, high frequency pulses called sparks. We can consider each individual spark event as a microscopic batch reactor, which can be tuned to achieve desired particle properties. Rapid local heating followed by rapid quenching results in small ( $<10$  nm) primary particles of high purity, free of solvents and surfactants. The spark repetition rate of spark generators is typically limited to  $\sim 300$  Hz, above which the spark becomes unstable. Chapter 2 of this thesis provides a solution that allows the repetition rate to be increased by two orders of magnitude. The duration of a spark event,  $t_{\text{spark}}$ , is typically  $<10$   $\mu\text{s}$ , and can be described as an underdamped RLC discharge with a resonant frequency on the order of a MHz [30]. Plasma temperatures in the spark reach up to  $2 \times 10^4$  to  $8 \times 10^4$  K [29, 31], and we can estimate the heating rate to be  $>10^7$   $\text{K s}^{-1}$ . Establishing the cooling rate is less trivial, and estimates ranging from  $-10^3$  to  $-10^7$   $\text{K s}^{-1}$  have been published [32, 33].

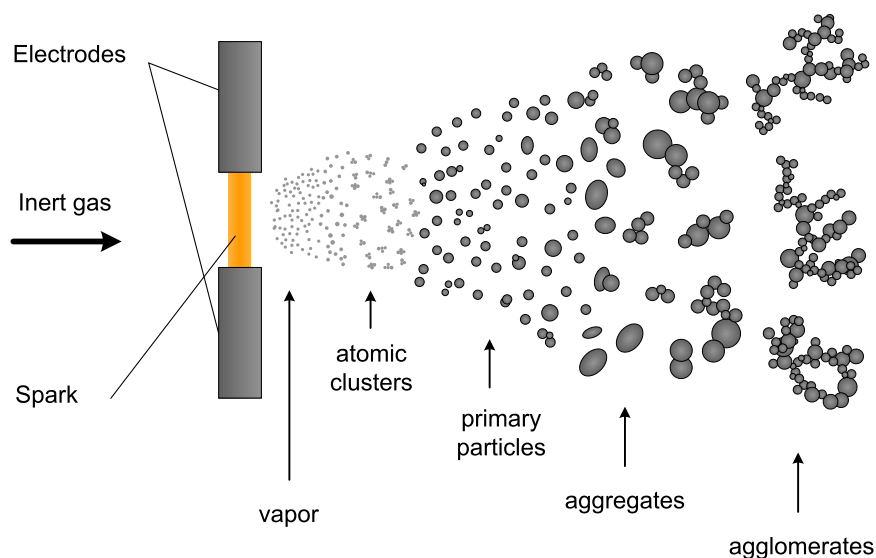


FIGURE 1.3 Particle formation mechanisms in spark discharge (Figure reproduced from [34]).

Particle formation in spark discharge can be described as a nucleation and condensation process that forms primary particles, followed by coagulation and coalescence to form aggregates and agglomerates (Figure 1.3). The minimum particle size achievable with spark discharge is a single atom [35]. Atomic clusters synthesized by spark discharge show preferential sizes consistent with observations on ‘magic’ clusters known from vacuum experiments [36]. The preferential sizes appear to be material dependent (Figure 1.4). These clusters, which are stipulated to behave as a kind of superatom [37], are available at atmospheric conditions and can be further processed, potentially making a new class of materials available.

The aerosol produced by the spark discharge has a high particle concentration, and the particles tend to agglomerate unless sufficiently diluted. Under clean conditions, metallic agglomerates sinter if their size is sufficiently small. In the case of gold, a critical particle size of 5 nm can be identified below which all particles are spherical [38]. This effect is used in chapter 7 of this thesis, where particles are coated with liquid-like atomic clusters of a second material. While the maximum primary particle size for different materials typically lies around 20 nm, spherical particles several hundred nano-

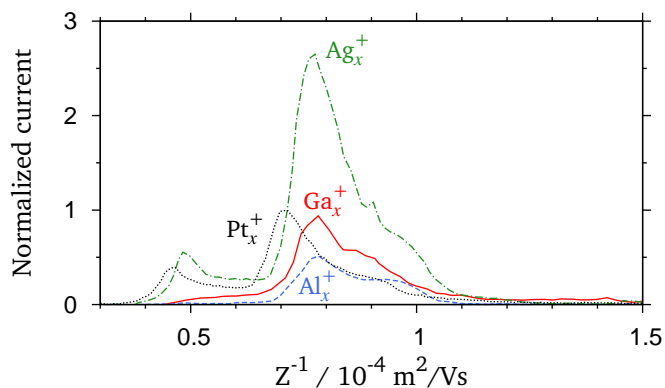


FIGURE 1.4 Metal clusters from a spark generator, unpublished work.

meter in size can be synthesized by allowing the particles to agglomerate, and subsequently reshaping them by sintering [39]. Using two parallel spark generator/sintering oven combinations, Kala et al. produced gold nanoparticles paired with germanium particles [40]. Sintering of spark discharge agglomerates is used in chapter 4 of this thesis in order to deposit silver nanospheres in solar cells.

The high temperatures, far exceeding the boiling point of any solid, make it possible to evaporate any conducting material. So far, over 20 elements have been used in spark discharge, including carbon [22], silicon [41], gallium [36], tungsten [42] and various other metals [42–45]. One powerful application of the spark is in the synthesis of mixed metallic particles (Figure 1.5), using either alloys [43, 45, 46] or sintered mixed powders [47, 48] as electrodes, or simply by placing two electrodes of different composition opposite each other [43, 49]. With the latter two methods it is possible to fabricate internally mixed nanoparticles from otherwise immiscible metals, with domain sizes on the order of 1 nm [48].

Non-metallic compounds such as oxides and hydrides can be formed by mixing small quantities of a non-inert gas in with the quench gas. Oxides are formed by adding a few percent of  $O_2$  to the carrier gas [44], or using the impurities present in commercial inert gases [10]. To produce essentially unoxidized Mg nanoparticles, special attention to system and gas purity must be taken [30]. By sparking Mg in 5%  $H_2$  in Ar, Vons [30] demonstrated that it is possible to produce  $MgH_2$  nanoparticles in the spark. A more detailed study on the formation of  $MgH_2$  is presented in chapter 5 of this thesis.

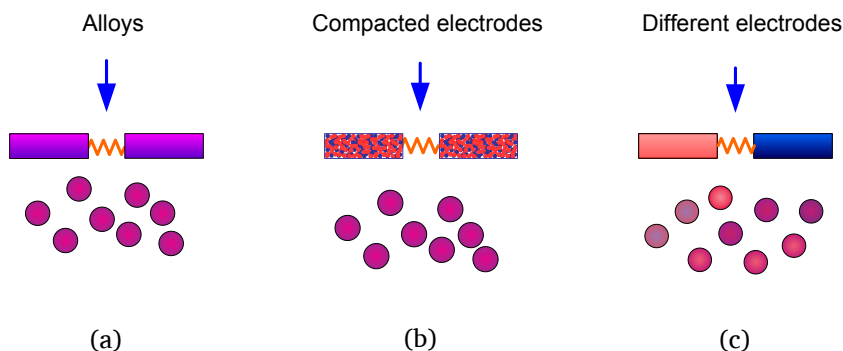


FIGURE 1.5 Three approaches to atomic mixing in spark discharge (Figure reproduced from [34]).

## 1.6 Scope of this thesis

The objective of this thesis is to develop the spark discharge method towards the fabrication of well-defined nanostructured materials, with special attention to use in energy storage and conversion applications.

The first part of this thesis, chapters 2 and 3, describes a novel method of increasing the production rate of a single electrode pair by two orders of magnitude; at low cost, and without changing the product properties. At the same time, the spark-to-spark variation in discharge energy is reduced, and linear scaling of production rate *vs.* input power is achieved.

The second part of this thesis concerns the use of spark discharge materials in energy storage and conversion applications. In chapter 4, size-selected silver nanospheres of 100 nm diameter are incorporated into a thin-film photovoltaic cell. The high-purity particles produced by the spark improve their performance as surface plasmon scattering enhancers within the solar cell. In chapter 5, the synthesis of magnesium-based metal hydrides in the spark is studied. The hydrides are evaluated for their potential use in hydrogen storage. In the last two chapters, the possibility of functionalizing particles using spark discharge is explored. Both agglomerates and spherical particles are coated with nanoclusters, providing various nanostructured morphologies. The addition of a Nb catalyst to help the hydrogenation reaction of magnesium is investigated in chapter 6. Finally, in chapter 7, the formation of smooth coatings of gold and silver on nanoparticles is described.

## Chapter 2

# Design of a 25 kHz Spark Generator

**T**HE PRODUCTION RATE OF A SINGLE SPARK GAP WAS INCREASED through better control of the discharge voltage, and by increasing the spark repetition rate. An improved spark generator concept based on high voltage switches (IGBTs) is presented. The switches allow the spark capacitor to be charged independently of the gas breakdown voltage, resulting in improved control over the spark repetition rate and the spark energy.

The prototype has an upper frequency limit of 25 kHz, and runs reliably at a power output of 300 W with an electric efficiency of 84 %. Spark formation is assisted by means of a continuous, low intensity DC current that provides additional space charge by two mechanisms. In the case of small gap spacings in helium the space charge is injected by a glow discharge. At larger gap spacings, and in argon, low energy microdischarges occur.

---

This chapter is based on: T. V. Pfeiffer, J. Feng and A. Schmidt-Ott, *Advanced Powder Technology* 25 2014, 56-70.

## 2.1 Introduction

The energy cost of nanoparticle production processes tends to be significant. Plasma based ablation processes operated at atmospheric pressure typically require  $10^3$  to  $10^6$  eV per atom, or  $10^6$  to  $10^9$  J mol<sup>-1</sup> [50]. Pai argues that the electron temperature  $T_e$  strongly influences the energy cost. At high  $T_e$ , electron energy is mainly dissipated in the plasma through excitation and ionization processes – both beneficial for electrode ablation – rather than momentum transfer. In order to obtain energy costs of  $\leq 10^7$  J mol<sup>-1</sup> a  $T_e > 2.5 \times 10^4$  K is required.

A metal hydride based fuel tank for a hydrogen car will require approximately 40 kg of active material. A hypothetical pilot plant with a production rate of 2 to 5 kg h<sup>-1</sup> is then required to produce enough hydrogen storage material for 500 hydrogen storage systems per annum.<sup>1</sup> Energy efficiency becomes a concern: current spark generators require  $10^7$  to  $10^8$  J per gram Mg [30, 42], or 10 MW to power our pilot plant. Regardless of the energy efficiency, pushing more power into the system means more product. While scaling up is possible by simply running multiple devices in parallel, the economy of scale is poor due to the low output of the spark gap.

### 2.1.1 Spark discharge generators

An increase in the production rate of a single electrode pair can be achieved in two ways: increasing the ablation efficiency  $\Delta m/\Delta E$ , and increasing the total power input. Especially in the latter there is ample room for improvement, as the energy cost for producing nanoparticles by spark discharge is already on the order of  $10^7$  J mol<sup>-1</sup> [42]. Spark generators in use today have a limited repetition rate of  $\approx 300$  Hz.<sup>2</sup> Mäkelä, Aalto, Gorbunov, et al. [52] use a slightly different geometry with sharp electrodes, running at 200 Hz. Byeon, Park, and Hwang [49] claim to operate a spark at a calculated frequency of 667 Hz using a 10 nF capacitance, but their system is overspecified. Based on their data, a frequency of 66.7 Hz or a capacitance of 1.0 nF seems more likely. Berkowitz and Walter [53] operate a spark submerged in a dielectric liquid with a frequency of 10 to 40 kHz. While this is a fundamentally different system, producing mostly particles in the  $\mu\text{m}$  range, it

---

<sup>1</sup>The current annual production of consumer vehicles is  $5 \times 10^7$

<sup>2</sup>Liu, Kim, Wang, et al. [51] mention using the PALAS GFG 1000 at a frequency of 1000 Hz, but this seems to be an error; the GFG 1000 has a maximum operating frequency of 300 Hz, obtained by setting the control knob to setting 999 ‰

is noteworthy to mention an energy cost of  $\sim 4 \times 10^6 \text{ J mol}^{-1}$  for  $< 20 \mu\text{m}$  particles, comparable to the efficiency of ambient pressure gas phase methods producing much smaller particles.

The duration of a typical spark event is approximately  $10 \mu\text{s}$  from onset of current flow until current collapse. This sets the theoretical upper limit of the repetition rate at  $\sim 100 \text{ kHz}$  at a 100% duty cycle. Considering that the spark needs to be quenched, and the energy supply needs to be recharged, lower duty cycles will be required in practice. A repetition rate of  $\sim 50 \text{ kHz}$  is an ambitious step forward.

### 2.1.2 Design concept

The distinguishing feature of a spark discharge is the high energy, oscillating current pulse that is responsible for electrode ablation. The high current pulse is directly responsible for the high temperatures of  $10^4 \text{ K}$  in the spark [29], making it possible to effectively ablate material from high melting point materials. Because the anode evaporates more rapidly than the cathode, the oscillating nature results in material from both electrodes being evaporated, allowing the synthesis of nanoparticles of non-alloying materials [32, 48]. When reactive gases are used in spark discharge, each spark can be considered a small reactor. This makes scaling up in the time domain without modifying plasma conditions very attractive.

This chapter describes an approach for scaling up of the classic spark discharge circuit, where maintaining the pulsed, oscillatory nature of the spark discharge is the primary design constraint. The increased scale is achieved by increasing the repetition rate. As a reference, we consider the spark generators and operating conditions as used by Tabrizi and Vons (Table 2.1). A better control of the spark energy is required, especially when going to higher repetition rates. The above goals can be achieved by decoupling the charge and discharge cycles using a number of switches. By increasing the repetition rate by two orders of magnitude, the power input increases from tens of W to the kW range. The gas flow rate through the reactor is increased to ensure adequate cooling and quenching at the higher power input, keeping a constant dilution over output power range. A continuous, low intensity ‘glow’ current increases the space charge density between subsequent sparks, providing sufficient initial free electrons to ensure a reliable spark ignition.

TABLE 2.1 Reference conditions for spark discharge as used in this chapter, from [10, 30, 41–43, 48, 54, 55].

Parameter	Typical values	Reference value
Discharge voltage, $U_d$	0.5 to 7 kV	3 kV
Charging current, $I$	0 to 30 mA	15.0 mA
Input power, $P$	0 to 30 W	
Repetition rate, $f_{\text{rep}}$	0 to 300 Hz	
Electrode spacing, $d_{\text{gap}}$	0.5 to 2.5 mm	2.0 mm
Flow rate	0.5 to 10 L min <sup>-1</sup>	1 L min <sup>-1</sup>
Electrode diameter	3 to 6.35 mm	6 mm
Capacitance, $C$	2.2 to 126 nF	20 nF
Inductance, <sup>a</sup> $L$	1 to 2 $\mu$ H	1.2 $\mu$ H
Gap resistance, <sup>a</sup> $R_{\text{gap}}$	1.3 to 20 $\Omega$	1.5 $\Omega$
Resonant frequency, $f_{\text{spark}}$	1 to 2.7 MHz	1.5 MHz

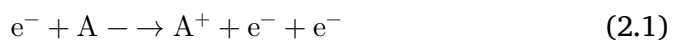
<sup>a</sup> Fitted using an *RLC* model.

## 2.2 Theory

### 2.2.1 Gas discharges and breakdown

The fundamentals of gas discharges have been thoroughly studied for over a century, and many textbooks on atmospheric discharges are available [25, 56]. In our context, a gas discharge is the transition from gas phase to plasma under the influence of an electric field. Three things are required to form a discharge: an initial ion or free electron has to be available to start an electron avalanche; the electric field has to be strong enough to gain a sufficient yield from electron avalanches; and there must be sufficient time for the avalanche, streamer, or leader to travel to the opposing electrode.

Consider a free electron in a gas that is subjected to an electric field. If the electric field is sufficiently large the electron gains enough energy to ionize a gas atom or molecule, freeing up an additional electron (Equation 2.1).



Both electrons gain energy in the electric field, which allows them to ionize more molecules and free up more electrons, causing a so-called electron

avalanche. Each discharge also produces photons, some energetic enough to ionize gas molecules. Next to the ionization events, there are processes leading to loss of charged species. Electrons and ions can recombine, drift out of the electric field, or reach the anode or cathode with a finite chance of releasing a new electron or ion. Electrons can attach to molecules, most notably  $O_2$ ,  $N_2$  and  $H_2O$ , to form negative ions, rather than participating in the electron avalanche.

Several mechanisms can provide the initial electron. The primary source of electrons are the metal electrodes, which have work functions of several eV. Hot surfaces emit electrons by thermionic emission, and if the hot surface is a cathode the electrons are drawn away from the surface. In field emission, electric fields on the order of  $1 \times 10^8 \text{ V m}^{-1}$  can directly extract electrons from metal surfaces. In room temperature spark generators, as discussed here, the above effects are negligible. Ultra-violet light can free electrons from gas species or metal surfaces through photo-ionization [23]. Radiation with higher energies, aptly termed ionizing radiation, can also provide the initial electron. For practical purposes, only UV and ionizing radiation in the form of cosmic rays are relevant for our ambient electric discharges.

In the case of a strongly non-uniform field, for example a needle perpendicular to a plane, a steady state can occur where a plasma forms at the high intensity field, the needle tip, but the ionization rate further away is insufficient to sustain the plasma. This results in a localized glow around the needle tip, called a corona discharge. If the ionization rate exceeds the loss rate throughout the gap, a conductive channel will grow between anode and cathode. Gas breakdown occurs when the conductive channel of the gas discharge spans the gap between cathode and anode, *and* the resistance of said channel drops below that of the external circuit, forming a short circuit [25]. Breakdown is characterized by a descending current-voltage characteristic: as the current through the channel increases, the voltage needed to sustain the channel drops. This can occur when Joule heating becomes significant enough to allow thermal emission of electrons. The temperature in the spark rises with increasing current, in the case of hydrogen reaching a plateau of  $\sim 6 \times 10^4 \text{ K}$ , after which increased spark energy results in isothermal growth of the plasma volume [29].

The breakdown strength of a dielectric gas is material and pressure dependent, and for non-rarefied gases can be expressed in units  $\text{V m}$  [57]. It represents the electric field required to cause breakdown in a quantity of gas. For non-ideal geometries with non-homogeneous fields, it is more convenient to work in terms of breakdown voltage  $U_b$ , the voltage required to

TABLE 2.2 Properties of selected dielectric gases. DC uniform field breakdown strengths  $((\mathbf{E}/N)_{\text{lim}})$  for selected gases, adapted from [57], compared to a fit of data from [42] for a spark generator with 0.25 to 2.0 mm gaps at 1 bar and 2 bar. Dielectric strength calculated from  $\mathbf{E}/N$  for 298 K and 1.013 bar.

gas	$(\mathbf{E}/N)_{\text{lim}}$ $10^{-21} \text{ V m}^2$	$(\mathbf{E}/N)_{\text{spark}}$ $10^{-21} \text{ V m}^2$	$(\mathbf{E}_b^0)_{\text{lim}}$ $10^6 \text{ V m}^{-1}$	$\mathbf{E}_{b, \text{spark}}^0$ $10^6 \text{ V m}^{-1}$	$\nu_{en}/p$ $10^7 \text{ Pa}^{-1} \text{ s}^{-1}$
N <sub>2</sub>	130	142	3.20	3.95	3.0
Ar	25.3	46.7	0.62	1.04	3.8
H <sub>2</sub>	65.0	—	1.60	—	3.8
He	—	9.56	—	0.36	0.8
Ne	2.17	—	0.053	—	1.5

cause breakdown in a given system, or for a system with variable electrodes, dielectric strength  $\mathbf{E}_b$ . Table 2.2 lists breakdown and dielectric strengths for a number of gases relevant for spark discharge.

The electrical conductivity  $\sigma$  of a plasma is determined by the electron concentration  $n_e$  and the mobility of the electrons. Fridman [24] gives the following expression for the (electron) conductivity in absence of strong magnetic fields.

$$\sigma = \frac{n_e e^2}{m_e \nu_{en}}. \quad (2.2)$$

The electron mobility is expressed in terms of the frequency of electron-neutral collisions  $\nu_{en}$ . In the case of argon  $\nu_{en}/p = 3.8 \times 10^7 \text{ Pa}^{-1} \text{ s}^{-1}$ , and at atmospheric pressure the equation reduces to

$$\sigma_{\text{Ar}} = n_e \cdot 7.3 \times 10^{-21} \Omega^{-1} \text{ m} \quad (2.3)$$

At high electron concentrations, the resistance of the small gaps used in spark discharge nanoparticle generators can drop well below  $1 \Omega$ .

The time required to form a spark after the occurrence of an initial ionization event, the formative time lag  $\tau_f$ , can depend critically on the gas composition and the overvoltage over the spark gap, with higher gap voltages giving faster spark formation [58, 59]. For  $> 99.99\%$  argon at 0.96 bar and a 3 mm gap, Kachickas and Fisher report a  $\tau_f$  of 70  $\mu\text{s}$  for 10% overvoltage, 5  $\mu\text{s}$  for 30% overvoltage, and  $< 1 \mu\text{s}$  for overvoltages exceeding 50%. In contrast,  $\tau_f$  in nitrogen and air drops down to 1  $\mu\text{s}$  for an overvoltage around 2%.

## 2.2.2 Spark generators

The circuit used in current spark generators is given in Figure 2.1a, where  $L$  is the intrinsic inductance of the leads connecting to the electrodes. The capacitance  $C$  is charged by a constant current power supply. Once the voltage over the capacitor  $U_C$  reaches the breakdown voltage  $U_b$  of the gas, a spark can form. The spark is a conductive channel, and the now shorted capacitance discharges its stored energy

$$E_C = \frac{1}{2}CV^2 \quad (2.4)$$

into the spark gap. Taking the combined resistance of electrodes, wires and plasma as  $R$ , one can model the spark discharge as an RLC discharge with a resonance frequency on the order of MHz (Figure 2.1b) [41]. To achieve high currents,  $R$  and  $L$  are preferably kept as small as possible. Once the energy stored in the capacitance is dissipated, the process is repeated (Figure 2.2a), RLC discharge not shown).

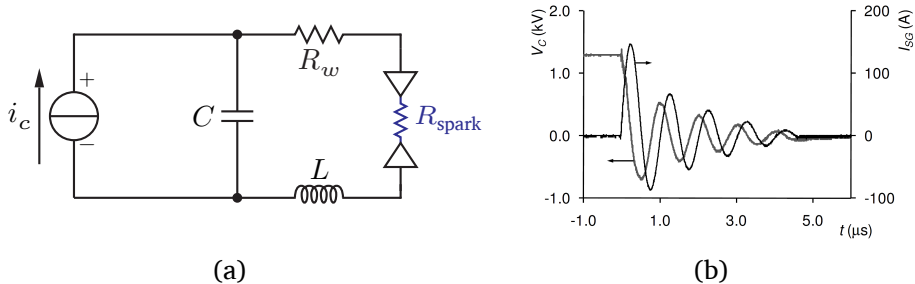


FIGURE 2.1 The spark as an RLC circuit. (a) Spark generator circuit. (b) Current and voltage traces of a spark discharge [30]

Due to the stochastic nature of spark formation and the method of capacitor charging, the discharge voltage  $U_d$ , defined as the voltage on the capacitance when the spark starts, can vary significantly between sparks. Because the energy stored in the capacitance scales with  $U_C^2$ , this has a strong impact on particle production.  $U_b$  effectively determines the capacitor energy, and the use of low breakdown gases such as He, Ne, and Ar (Table 2.2) is therefore limited to low energy discharges. This effect becomes more drastic when subsequent sparks start influencing each other. When  $U_C$  starts to rise faster than the gas can recover after a spark, premature breakdown at low energy can occur (Figure 2.2b). The gas composition can also influence the recovery time of the gas. Removing  $O_2$  and  $H_2O$  impurities lowers the discharge

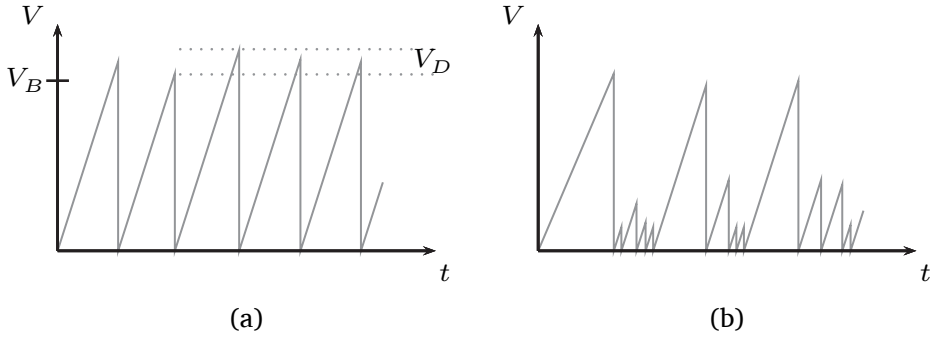


FIGURE 2.2 Schematic representation of  $U_c$  vs. time. (a) without and (b) with cross-talk between sparks.

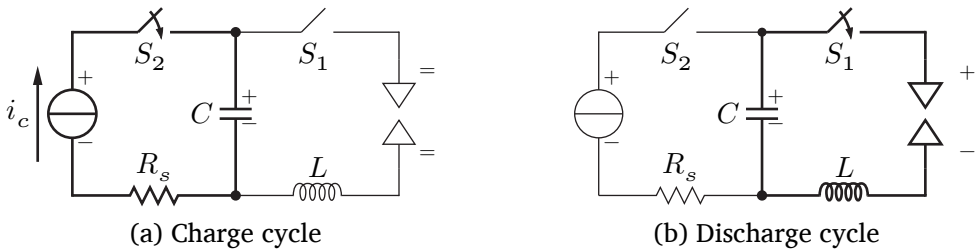


FIGURE 2.3 Spark circuit with decoupled charging cycles.

voltage of argon significantly when magnesium electrodes are used, which can be attributed to enhanced photoemission [30: p. 67].

In an ideal spark generator each spark is equipotent. A straightforward method of ensuring constant spark energy is shown in Figure 2.3. Two switches are used to decouple charging and discharging of capacitor  $C$ . The cycle starts by closing switch  $S_2$  until the desired  $U_c$  is reached (Figure 2.3a). Because  $S_1$  is open there is no potential difference over the spark gap, and  $U_c$  is independent of the breakdown voltage of the gap. Once  $S_1$  closes the potential difference over the spark gap is  $U_c$ , and if  $U_c > U_b$  a spark can form (Figure 2.3b). When the discharge is completed  $S_1$  opens and the cycle can be started again.

## 2.3 Experimental

### 2.3.1 New power supply

#### Fast high voltage switches

Several options that allow rapid switching of high power and high voltage exist, all built around the concept of a thyristor. A thyristor consists of a four layer n-p-n-p or p-n-p-n structure that allows much higher voltages than transistors can tolerate. The equivalent circuit of a thyristor is a self-latching combination of a p-n-p and a n-p-n transistor. The thyristor is turned ‘on’ by applying a sufficient voltage at the gate of either of the built-in transistors. Once on, an internal positive feedback loop keeps the thyristor in a forward conducting state. Conduction stops once the forward current drops sufficiently, and the freed charge carriers recombine.

Because the thyristor cannot be switched ‘off’ and recovery is slow, it has been mostly superseded by power MOSFETs and IGBTs. Power MOSFETs and IGBTs both use a similar planar topography to allow high currents and high voltages, and feature an isolated gate that switches the device on and off (Figure 2.4). Both devices have wide safe operating areas and are protected against latch-up.

The IGBT is a minority carrier device and has a p<sup>-</sup> injector layer that lowers the forward conducting voltage, while the MOSFET is a majority carrier device. An IGBT does not conduct in the reverse direction, but most packages can be supplied with an internal anti-parallel fast recovery diode to allow current to flow in the reverse direction. Typically, IGBTs withstand higher voltages and currents with low conduction losses, at the expense of slower switching and higher switching losses. Because high voltage and high current are required in the spark, the IGBT is preferred.

At the low cost of €14, IXGR 16N170AH1 is a 1.7 kV, 16 A fast switching IGBT comprising an internal anti-parallel ‘freewheeling’ diode, [60]. With turn-on times on the order of 40 to 60 ns, turn-off times on the order of 100 to 400 ns, this is sufficient for the intended spark duration of <10 μs and target repetition rate of 25 to 50 kHz. To allow for the high peak currents of ~200 A, we use four IGBT in parallel in the current path of the spark discharge.

#### Spark generator topology

The circuit described in Figure 2.3 requires the use of a high side switch, with logic at high voltage level. Because of the poor availability of suitable

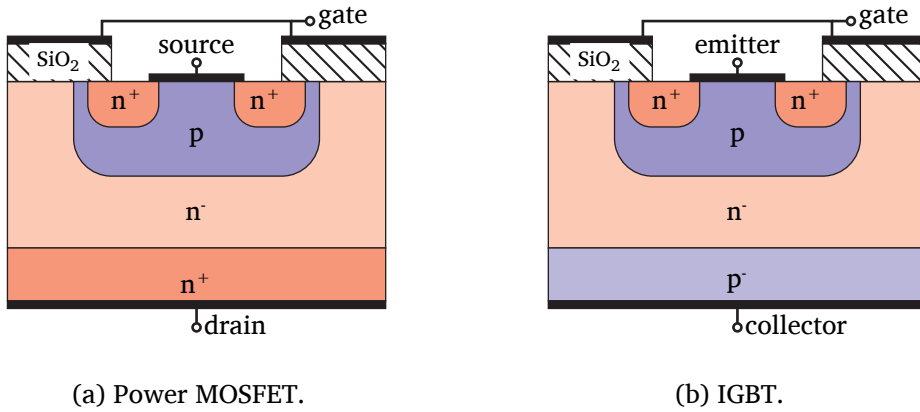


FIGURE 2.4 Internal structure of generic Power MOSFET and IGBT.

switches, we use three regular high voltage switches in the topology shown in Figure 2.5a. In this configuration, the capacitor  $C$  is charged by closing switches  $S_2$  and  $S_3$  (Figure 2.5b). Once  $C$  is fully charged  $S_2$  and  $S_3$  open, and the capacitor is left floating (Figure 2.5c). When we now close  $S_1$ , the left-hand side of the capacitor is forced to 0 V, and the right-hand side of the capacitor is pushed down to negative polarity. The top electrode follows, and the potential difference of the capacitor is placed over the spark gap. When this potential difference exceeds the breakdown voltage of the gap, a spark forms. Once the conductive channel is formed, the typical RLC discharge of  $C$  will take place (Figure 2.5d). Note that there is still only one switch in the high current spark loop.

To facilitate the formation of the discharge, the right electrode can be pulled up to high voltage. This has two effects: a stronger field is formed in the gap, and a small sustained current can prevent the discharge from dying out completely. For convenience we call this current a glow current, even if the discharge is too weak to give a visible glow. By sustaining a discharge a lower supply voltage is needed to form a spark, and less energy is lost in forming the spark channel. Of course the glow current should be small enough that it does not play a role in electrode ablation.

The final topology is shown in Figure 2.6, and functions analogously to the three-switch circuit. The main capacitor  $C_1$  is charged by closing switches  $S_2$  and  $S_3$  in a boost converter configuration.  $C_1$  consists of an array of  $96 \times 0.47$  nF NP0 capacitors in parallel. When charged to 1500 V, this 45 nF

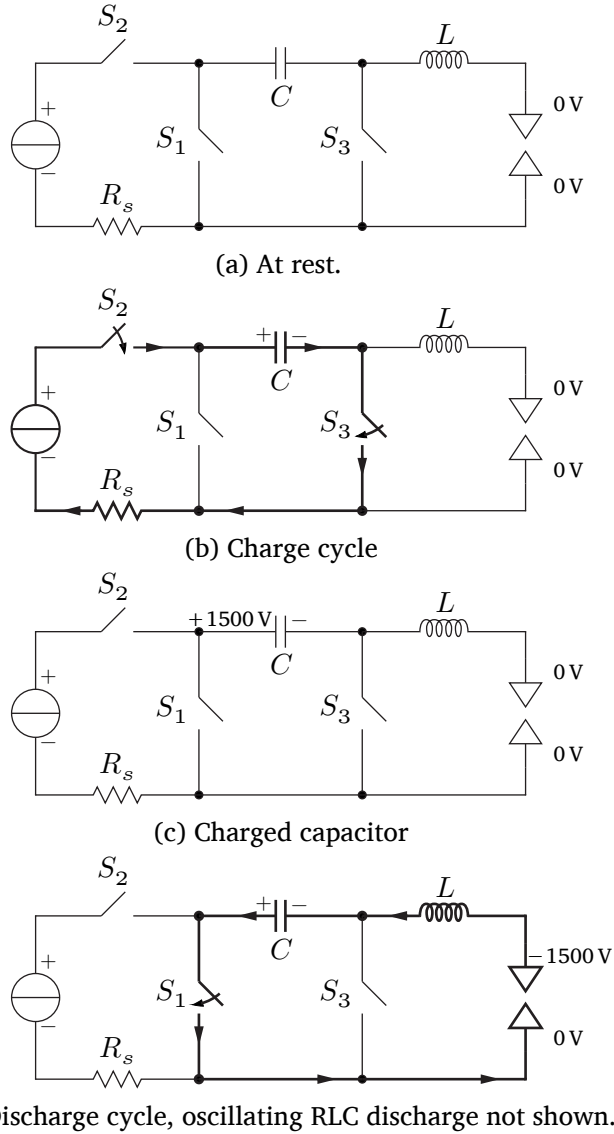


FIGURE 2.5 Spark topology using three high voltage switches.

capacitance stores 51 mJ, similar to the spark energy typically used in the classic circuit [42]. Diode  $D_{15}$  compensates for the unknown initial charge state of  $C_1$  by limiting the capacitor voltage to the supply voltage. The discharge is initiated by closing  $S_3$  with all other switches open, allowing current to flow along the path  $C_1 - S_1 - D_8 - \text{gap} - C_1$ . To allow current inversion, switch  $S_4$  is closed 500 ns later, i.e. before the first half cycle has completed. The electrodes are referred to according to the role they play during the first half cycle: the left electrode in Figure 2.6 is the anode, the right electrode is the cathode. The positive current direction is left-to-right through the spark gap.

The right hand electrode is pulled up by three mechanisms.  $R_2$  is a 200 k $\Omega$  resistor continuously supplying up to 2.5 mA towards the gap.  $S_6$  closes just before  $S_1$  does, providing an additional 50 mA during 1  $\mu$ s. Operation of  $S_6$  can be turned on or off by means of a toggle switch. Finally, the 9.4 mH  $L_3$  supplies a boost of 500 mA.  $S_5$  is used to limit losses when  $C_1$  is left with reversed polarity after a partial discharge. Residual energy in  $C_1$  is transferred to  $L_4$ , and returned to the power supply through  $D_{13}$ .

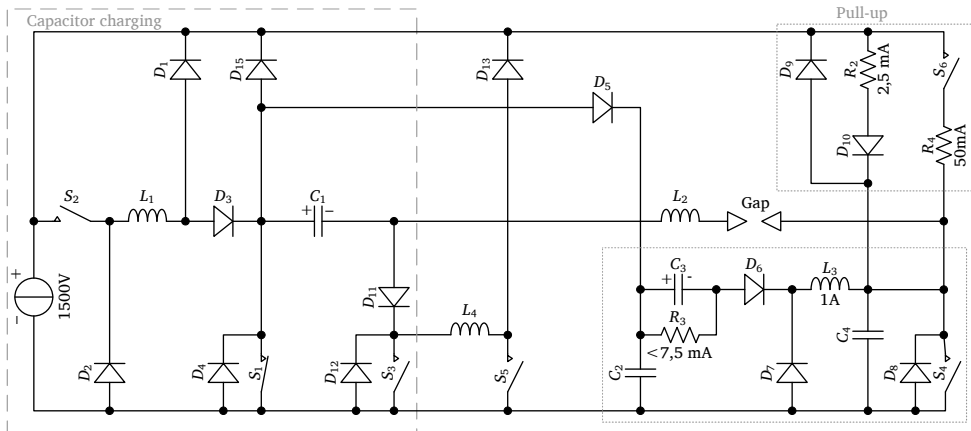


FIGURE 2.6 Expanded circuit with a pulled up cathode.

The spark generator is driven by an analog clock that allows the spark repetition rate to be set, e.g. by a potentiometer. The timing sequence of the switches is shown in Figure 2.7, where  $t_0$  is defined as the start of the trigger pulse T. The capacitor charging cycle is set to take 12.3  $\mu$ s.  $S_1$  opens for 10  $\mu$ s to allow forward conduction, while free oscillation is possible from  $t = 1.1$  to 7.8  $\mu$ s. The cycle ends after a 6  $\mu$ s energy recovery stage, with a total duration of 29.2  $\mu$ s. The timing sequence used here allows repetition

rates up to 34 kHz, but the prototype is limited by the internal clock to 25 kHz.

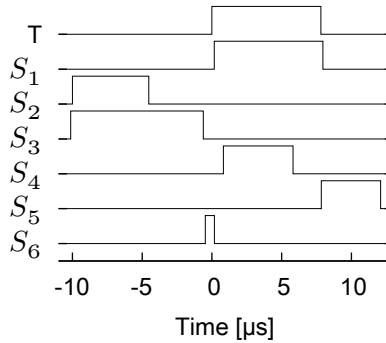


FIGURE 2.7 Timing sequence of switches from Figure 2.6

It is worth noting that both electrodes are referenced against the power supply ground. This makes it possible to influence the mean electric field inside the reactor by biasing the electrode pair versus the reactor housing. By changing the electric field one could minimize electrostatic losses inside the reactor, or even increase the yield of charged particles with a given polarity [61].

#### Physical description

The spark generator circuit is built into a box of  $\approx 3 \text{ dm}^3$  with a high voltage input, a ground cable and two high voltage leads. Timing and logic of the spark generator are powered by an external 12 V DC power supply. IGBT's and critical diodes are mounted on an air-cooled heat sink. The repetition rate of the spark generator is controlled from 1.06 to 25 kHz using a potentiometer. Two BNC connectors allow voltage on both electrodes to be monitored.

#### 2.3.2 Reactor

The reactor is described in chapter 3, page 43.

#### 2.3.3 Measurements

A LeCroy 9354 mass storage oscilloscope was used to analyze the performance of the circuit with up to 2 ns resolution. The internal clock of the

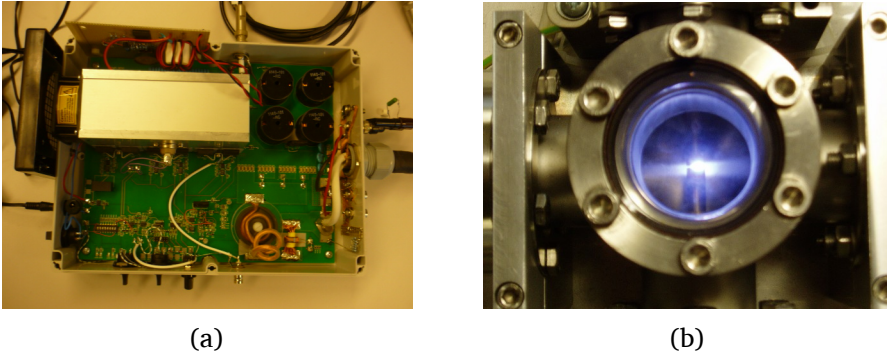


FIGURE 2.8 Spark generator prototype. (a) Generator with top removed, (b) View of sparks between two electrodes.

spark generator was used as the oscilloscope trigger. The current flowing through the spark gap was measured using a Pearson 110 current probe on one of the leads leading to the spark gap. Voltages were measured at the spark generator circuit, referenced to ground, using either a Tektronix P6015A high voltage probe (1:1000) with a 75 MHz bandwidth, or Testec TT-HV250 probes (1:100). The oscilloscope signals are corrected for different propagation delays in the leads of the probes to an accuracy of  $\pm 0.5$  ns. During development, it was found useful to monitor thermal dissipation within the circuit using a Fluke Ti-55 thermal imaging camera.

## 2.4 Results and Discussion

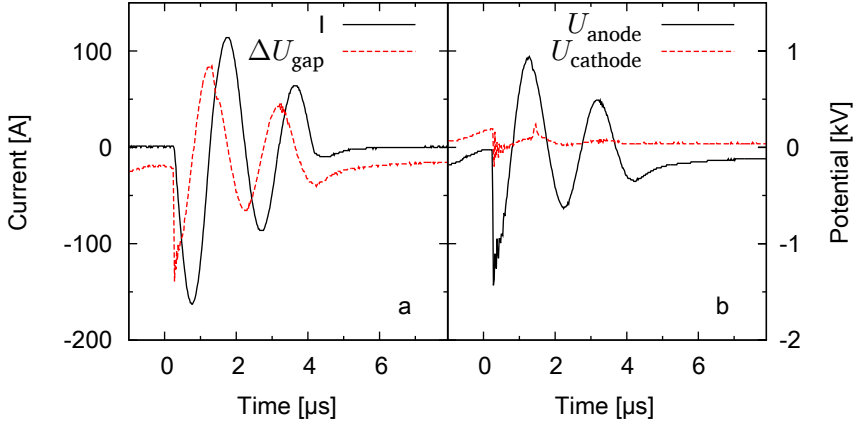


FIGURE 2.9 Oscilloscope traces for a typical spark event. (a)  $I$  and  $\Delta U_{\text{gap}}$ , (b)  $U_{\text{anode}}$  and  $U_{\text{cathode}}$ .

Figure 2.9 shows a typical oscilloscope trace of a spark event, where  $t_0$  corresponds to the start of the trigger pulse. At  $t_0$  the voltage on the cathode is 200 V as a result of the pull up mechanisms. When  $S_1$  has opened at  $t = 0.2 \mu\text{s}$  the anode voltage drops at a rate of  $4 \times 10^{10} \text{ V s}^{-1}$ . 20 ns later the anode follows as the resistance of the gap decreases with increasing space charge due to enhanced ionization. The spark ignites, current through the shorted gap increases to a peak of 165 A, and the typical oscillation of the RLC discharge follows. Fitting the RLC discharge according to Vons [30] yields  $L = (2.5 \pm 0.7) \mu\text{H}$ , and  $R_{\text{gap}} = (0.7 \pm 0.2) \Omega$ , comparable to the values of Vons [30]. While the simple RLC approximation is not strictly valid due to the presence of diodes and switches, it does demonstrate that the discharges are essentially identical to the desired waveform of the classic spark system.

Figure 2.10 shows the current-voltage characteristic of the spark generator circuit, constructed by plotting current and voltage waveforms such as in Figure 2.9a against each other. With the spark generator circuit connected to a fixed resistance (Figure 2.10a), the decay of the oscillation is clearly visualized by the tangential angle. We can see that with a higher resistances the gap voltage increases and the curve spirals to the origin faster. The circuit deviates from a perfect spiral in the bottom right corner. This is associated with the anti-parallel diodes starting to conduct.

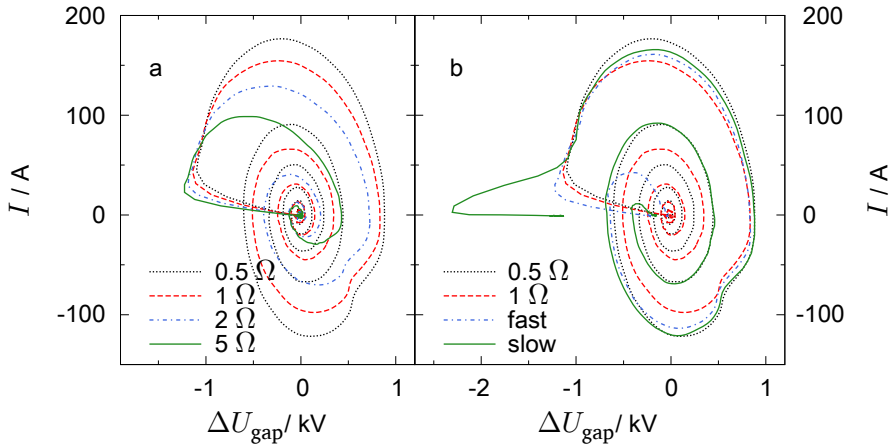


FIGURE 2.10 Current-voltage characteristic of the circuit, a) with a purely resistive load, and b) with a spark gap compared to a resistive load.  $U_s = 1.5 \text{ kV}$ ,  $f_{\text{rep}} = 1.0 \text{ kHz}$ ,  $d_{\text{gap}} = 2 \text{ mm}$ .

In Figure 2.10b the current-voltage characteristic of the spark generator for two sparks are compared with a purely resistive load. They represent two distinct modes observed with the circuit, that will be discussed in the following sections. The curve labeled ‘slow’ starts with a sharp cathode drop to  $-2.3 \text{ kV}$ , followed by a gradual increase in current through the gap. In the curve labeled ‘fast’ the sharp cathode drop is absent. In both cases, a discharge of finite resistance is still active in the gap when the spark is initiated. The discharge has the required descending current-voltage characteristic (see page 15), and the gas starts to break down. After breakdown the discharge behaves similarly to a  $0.5$  to  $1.0 \Omega$  resistor, consistent with the fitted result of  $0.7 \Omega$ , until the current becomes insufficient to sustain a spark. As ionization rates decrease the resistance in the gap increases, and the oscillation is dampened.

#### 2.4.1 Plasma ignition

When discussing spark formation with the new circuit, we can distinguish two cases. The first case is the initial *ignition* of the plasma in the absence of a glow current, when the system is switched on after a period of rest. The second is the *formation* of a spark, either by itself or in the wake of its predecessor, which will be discussed in subsection 2.4.2.

Because there is no explicit source for seed electrons during ignition, it typically takes between 1 s and 20 s for the first spark to form. Small gaps ignite easily and fast, and once the plasma is ignited the electrode spacing can be increased as desired. For large gaps the generator is not able to ignite the plasma, even if the spark generator is capable of maintaining the plasma at such a spacing. Ignition could be made more robust by incorporating a source of ionizing radiation, preferably UV, aimed at the spark gap.

When the first spark occurs sufficient space charge is kept in the gap to ensure that essentially each subsequent energy pulse results in the formation of a spark, and the plasma is ignited (Figure 2.11). Occasionally at larger gap spacings, roughly  $>1$  mm in Ar, a solitary first spark forms without igniting the plasma. From this we can infer that the ionization rates as a result of the pull up mechanisms are comparable in magnitude to the loss rates in the gap, and the use of even larger gaps would require additional current passed on to the pull-up mechanisms for stable operation.

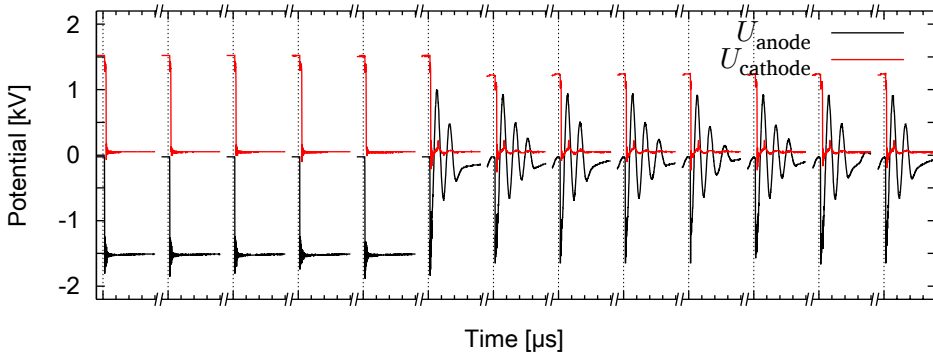


FIGURE 2.11 Ignition of a spark at  $f_{\text{rep}} = 1$  kHz. The dashed lines represent  $t_0$  of each spark attempt. Minor ticks represent  $0.2 \mu\text{s}$ .

#### 2.4.2 Formative time lag

Figure 2.12 shows the time from opening  $S_1$  until onset of current flow, arbitrarily defined here as the moment when the forward current through the gap exceeds 1 A. If sufficient free electrons are available in the gap to start avalanche formation, this time is the formative time lag  $\tau_f$ . For 0.5 mm and 1.0 mm gap spacings in Ar this happens at  $(24 \pm 4)$  ns, where the spread can be attributed to experimental limitations.  $\Delta U_{\text{gap}}$  reaches its maximum at

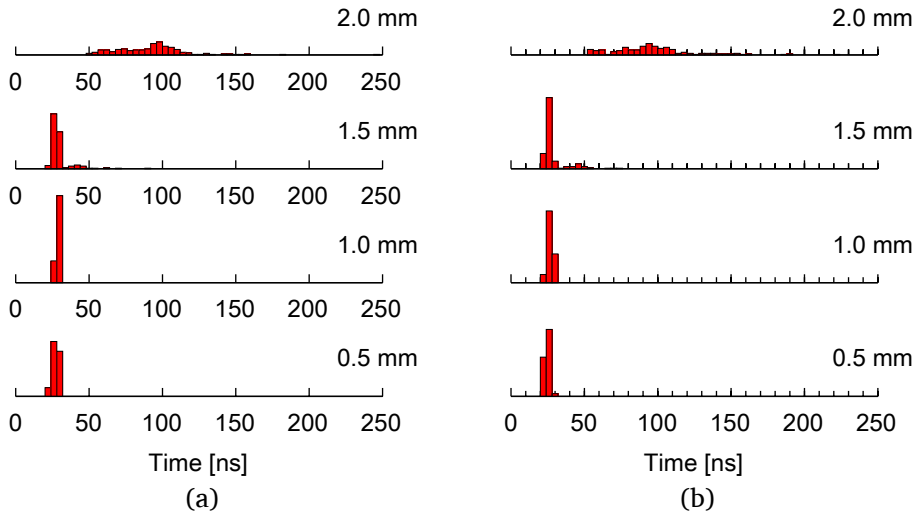


FIGURE 2.12 Current onset delay or formative time lag for different gap spacings at 1.5 kV in Ar. Each series consists of 200 spark events. (a) no current boost, and (b) with the current boost via  $S_6$  turned on.

$t = 48$  ns, limited by the large current flowing through the gap. The  $I$ - $V$  curves corresponding to this set are of the ‘fast’ type (Figure 2.10b).

The near instantaneous ignition is too fast to be explained through streamer theory. The electron transit time in the gap can be estimated from the electron mobility and gap voltage, and is approximately 10 ns. The ion transit time is roughly 500 times greater. A significant space charge has to be present in the gap in order to have sufficient seed electrons to cause breakdown at times much shorter than the ion transit time. This space charge either remains from the prior spark, with the help of the pull-up mechanisms, or is formed through resonance photons [58]. The presence of a residual space charge is confirmed by the observed finite resistance of the gap, which requires a significant electron density. As the voltage is increased further ionization rates in the channel increase, resistance drops, the channel heats up and expands, and breakdown of the gas can occur once again.

At larger gap spacings, a second population of formative time lags appears. The  $I$ - $V$  curves corresponding to this set are of the ‘slow’ type (Figure 2.10b). These formative time lags follow an exponential distribution, which is the expected result for streamers initiated by a series of electron avalanches. The observed ignition times are however an order of magnitude shorter than the ion transit time at the gap spacings and voltages used here. Kachickas and

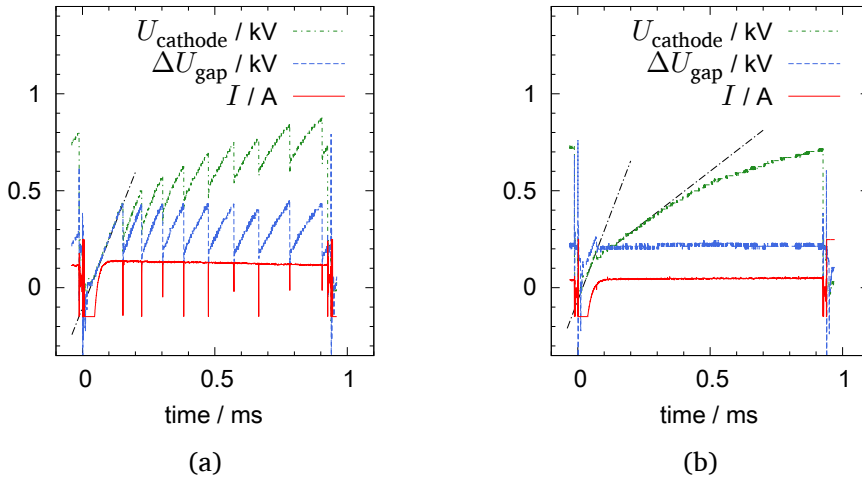


FIGURE 2.13 Current and voltage traces of the glow regime for a 0.5 mm gap,  $U_s = 1.2$  kV and  $f_{\text{rep}} = 1$  kHz. (a) capacitive discharges in Ar, (b) glow in He.

Fisher [59] explained similar findings in nitrogen by cathode photo-emission, possibly with minor contributions from photo-ionization of the gas close to the cathode. In our case, where depending on the quench gas conditions the electrode surfaces can reach temperatures above 1200 K (see chapter 3), thermionic emission from the cathode could also play a role.

### 2.4.3 Glow discharge

The discharge maintained between the sparks typically is not a stable DC glow, as can be seen from the oscilloscope traces in Figure 2.13. The current converges to a DC current of  $\sim 60$  mA, and shows repetitive weak capacitive discharges, which we'll refer to as microdischarges. The 60 mA value is an artifact of the coil used in the measurement, and attempts to measure the current using a shunt resistor show that the average DC current through the gap leads is  $< 1$  mA. Such currents might sustain a weak glow discharge, but are at least three orders of magnitude too low to sustain an arc, and will not result in the ablation of a significant amount of mass from the electrodes [24].

The microdischarges form as  $U_{\text{cathode}}$  rises sufficiently to cause breakdown, and some of the energy stored in the  $0.3$  nF of  $C_4$  in Figure 2.6 is dissipated in the gap. The microdischarges transfer charge from the cathode to the anode, and as a result the anode voltage (not shown in Figure 2.13a) and the

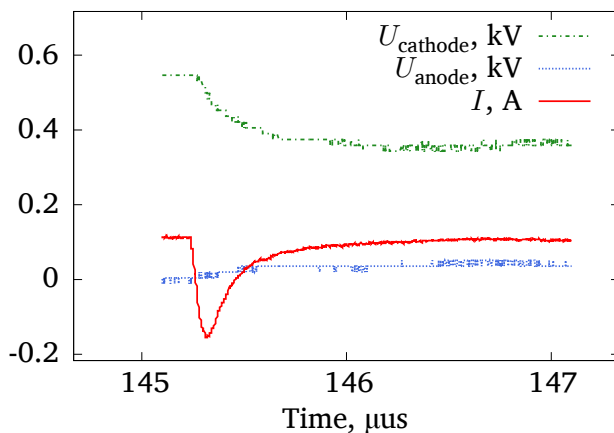


FIGURE 2.14 A single microdischarge, 0.5 mm gap in Ar.

cathode voltage increase stepwise. The gap voltage  $\Delta U_{\text{gap}}$  remains constant, with dielectric strengths of  $8.7 \times 10^5 \text{ V m}^{-1}$  for Ar and  $1.6 \times 10^5 \text{ V m}^{-1}$  for He. The occurrence of microdischarges can be qualitatively linked to the occurrence of ‘fast’ discharges of Figure 2.10b). This indicates that the microdischarges inject electrons into the gap, increasing  $n_e$  sufficiently to ensure an instantaneous discharge.

A single microdischarge is highlighted in Figure 2.14. The microdischarges have peak currents in the range of 10 to 700 mA and appear similar in waveform to the filamentary discharges observed in dielectric barrier discharges [62]. These microdischarges can result in electrode ablation, and several researchers have worked on particle generators based on DBD [63, 64]. While particles have been observed that originate from electrode ablation, the production rates lie many orders of magnitude lower than those of the spark. The only quantitative data available indicates a production rate of  $10^{-14} \text{ mol s}^{-1}$  for a 9.5 W power input, or  $>10^{14} \text{ J mol}^{-1}$ , versus  $10^6$  to  $10^9 \text{ J mol}^{-1}$  for spark discharge [63]. Thus, particle production through microdischarges can be neglected.

During the glow phase,  $U_{\text{cathode}}$  rises at a rate of  $(3.5 \pm 0.1) \times 10^6 \text{ V s}^{-1}$  for He with gap spacings of 0.5 to 2.5 mm and Ar with gap spacings of 0.5 mm and 1.0 mm. This corresponds to a charging current of 1.0 mA for  $C_4$ , which corresponds well with the target pull up current. For a 0.5 mm gap in a flow of  $1 \text{ L min}^{-1}$  He the microdischarges ignite a glow discharge with a voltage drop of 0.21 kV (Figure 2.13b). During the glow  $U_{\text{cathode}}$  rises at a

rate of  $1 \times 10^6 \text{ V s}^{-1}$ , corresponding to a 0.3 mA charging current for  $C_4$ . Thus, 0.7 mA of the pull up current is diverted into the glow, and we can deduce that the glow channel has a resistance of  $3 \times 10^5 \Omega$  and dissipates 0.15 W. Assuming the glow forms over the full  $2.8 \times 10^{-5} \text{ m}^2$  electrode surface, Equation 2.3 gives a electron concentration of  $10^{16} \text{ m}^{-3}$ , which is very reasonable for glow discharges [56].

#### 2.4.4 Spark energy

We can define a total energy stored in the spark generator during the spark  $E_{\text{SG}}$  as the sum of the electric energy,  $E_C$ , and the magnetic energy,  $E_L$ .

$$E_{\text{SG}} = E_L + E_C = \frac{1}{2}LI^2 + \frac{1}{2}CU^2 \quad (2.5)$$

The energy available to form a spark and ablate material is the energy stored in the capacitor (Equation 2.4). Because of the large voltage transients of  $C_1$  during charging,  $U_C$  could not be measured directly, and we take  $U_s$  as the initial voltage. Under normal operating conditions this is a valid assumption, as the boost converter configuration ensures that the capacitor is fully charged, while  $D_{15}$  ensures that  $U_C \leq U_s$ . The energy remaining in the capacitor after an incomplete discharge can be obtained directly through  $U_{\text{cathode}}$ . For odd halfwaves, the voltage ends positive, and energy recovery through  $L_4$  is required.

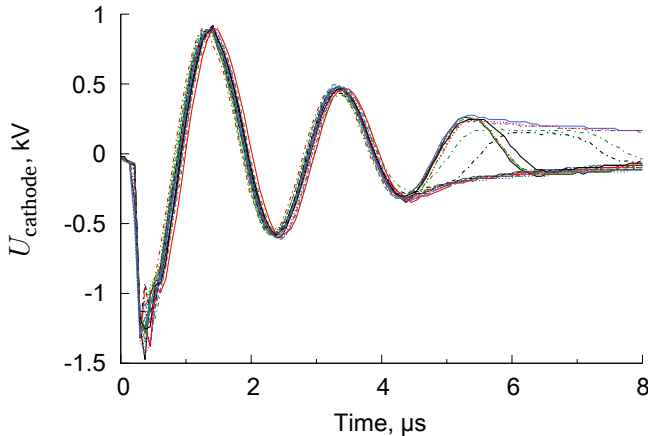


FIGURE 2.15 Decay of  $U_{\text{cathode}}$  for 20 sequential discharges.  $d_{\text{gap}} = 2.0 \text{ mm}$ ,  $U_s = 1500 \text{ V}$ ,  $1.0 \text{ L min}^{-1} \text{ Ar}$ ,  $f_{\text{rep}} = 1.0 \text{ kHz}$

Figure 2.16 shows the progression of a spark, expressed in available or stored energy  $E_{\text{sg}}$  as obtained with Equation 2.5 versus time, for different gap spacings. For  $L$  we use our fit result of  $2.5 \mu\text{H}$  (page 25). The uncertainty of the fitted  $L$  is sizable, and Figure 2.16 serves mainly as a general indication of the progression of a spark. The bumpy nature of the curve is due to the phase shift of the dampened oscillation, and can be qualitatively described by plugging  $U(t)$  and  $I(t)$  of the RLC-model into Equation 2.5. For all gap spacings,  $E_{\text{SG}}$  drops exponentially; from 50 mJ to  $<5$  mJ in  $4 \mu\text{s}$ . From this we conclude that spark behaviour is essentially independent of the gap spacing.

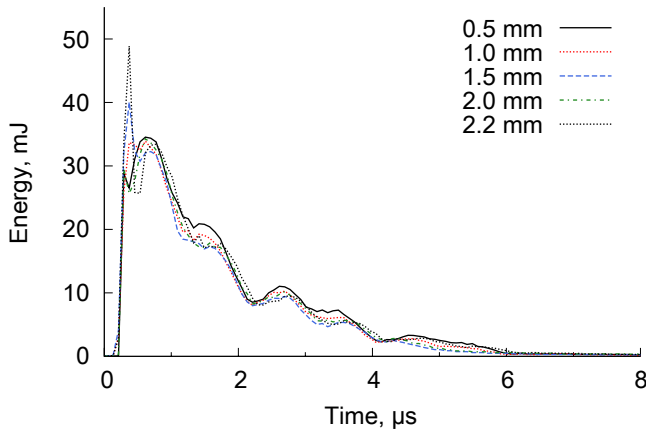


FIGURE 2.16  $E_{\text{SG}}$  during discharge for several gap spacings.  $U_s = 1500 \text{ V}$ , Ar,  $f_{\text{rep}} = 1.0 \text{ kHz}$

For the 1500 V sparks, spark to spark variation starts to occur after two full-cycles (Figure 2.15). With each half-cycle, less than half of  $E_C$  remains. The residual energy is small, and  $(49.8^{+0.8}_{-2.4})$  mJ is dissipated in the plasma. When low voltages are used, and thus  $I$  is low, the plasma quenches faster. At 1.00 kV, the spark waveform consists of either two or three half-cycles (Figure 2.17). In the first half-cycle,  $(18.2 \pm 1.0)$  mJ are dissipated. The second and third half-cycle dissipate  $(3.4 \pm 0.4)$  mJ and  $(1.1 \pm 0.2)$  mJ, respectively. While the third half-cycle is responsible for only 5% of the total spark energy, it can impact particle production significantly. From one half-cycle to the next, current flows in the opposite direction, and the different ablation rates of anode and cathode result in inconsistent ablation. This is particularly problematic when electrodes of two different materials, or even smaller discharge voltages, are used. For the production of atomic clusters, low spark

energies and voltages are important [35]. To obtain more consistent sparks at low voltage, the spark could be prematurely cut off, for example by closing  $S_1$  after the first half cycle.

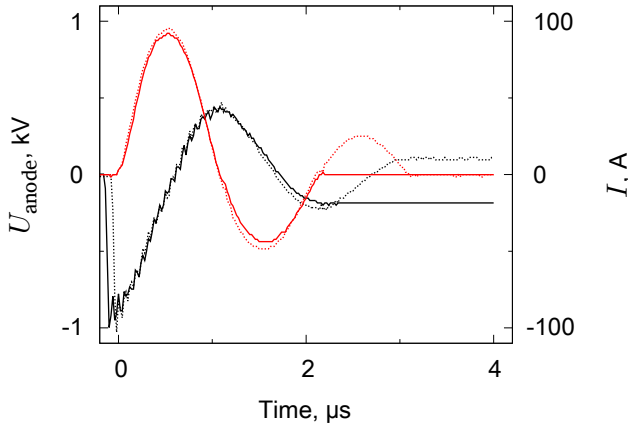


FIGURE 2.17 Oscilloscope traces at  $U_s = 1.00$  kV,  $d_{\text{gap}} = 0.5$  mm in Ar,  $f_{\text{rep}} = 17$  kHz. .

#### 2.4.5 Power dissipation

At a repetition rate of 8 kHz with  $U_c = 1$  kV, the spark circuit draws a current of 205 mA. Using Ohm's law, we find a power output of 205 W for the power source. Assuming complete discharge of the capacitor, we can calculate a power input into the plasma of 180 W from the spark energy (Equation 2.4) and the repetition rate. The dissipation in the circuit is then 25 W, or 12% of the input power. In practice, the capacitor does not discharge completely (Figure 2.9). Taking into account the residual capacitor energy due to incomplete discharge, 173 W is dissipated in the spark for an overall electric efficiency of 84%.

**Components** The maximum power output of the spark generator circuit is limited by the components used, and the way they are placed and cooled. Initially an array of 20 2.2 nF X7R capacitors in parallel was used. This array had a thermal resistance of  $0.6 \text{ KW}^{-1}$ , limiting its use to  $<200$  W before the thermal limit of the capacitors was reached. By distributing the current over a larger number of capacitor packages and switching to a NPO dielectric, the

thermal resistance of the capacitor array was reduced significantly. The new  $96 \times 0.47 \text{ nF}$  capacitor array has a thermal resistance of  $<0.08 \text{ KW}^{-1}$ , and is thus rated for  $>1250 \text{ W}$ .

The remaining limiting factors in the prototype circuit are the IGBTs in the discharge path, that have to conduct the short  $>100 \text{ A}$  pulses. In the current configuration the spark runs reliably at  $1.2 \text{ kV}$ , while for higher discharge voltages  $S_1$  and  $S_4$  have to be actively monitored for overheating. The largest currents are handled by  $S_1$ , which consists of an array of 4 IGBTs in parallel. Because the conductivity of IGBTs increases with temperature, they are prone to thermal runaway. Current is distributed unequally over parallel IGBT packages, and one of the packages will reach its thermal limits, while the others are barely used.

The power output range of the circuit could be extended by increasing the number of IGBTs in the array, or preferably by better distributing the current over the IGBT packages. This is not trivial, but could perhaps be achieved using balanced low value series resistors with a positive temperature coefficient. A better solution would be incorporating smart IGBT control combined with temperature and/or current probes on the individual IGBTs. In the prototype  $S_4$  is a single IGBT that conducts the return stroke of the discharge. Replacing the single package with an IGBT-array will improve performance at high discharge voltages.

## 2.5 Conclusion

Nanoparticle production with conventional spark generators is limited by strongly varying spark energies at spark repetition rates above  $300 \text{ Hz}$ . By decoupling the charge and discharge cycles of the spark generator, consistent sparks can be obtained at repetition rates on the order of  $10^2 \text{ kHz}$ . The prototype reliably operates at a power output of  $300 \text{ W}$ , one order of magnitude higher than conventional spark generators. The limiting factors in the prototype are the IGBTs. IGBT technology is fairly new, and it is reasonable to expect better components to become available in the near future. With the current state of the art, replacing the single IGBT  $S_4$  by a number of parallel IGBTs, and improving the current distribution over the parallel IGBTs will expand the operating range of the spark generator into the  $\text{kW}$  range.

Using a pull-up resistor, space charge can be kept in the gap to facilitate spark formation. If sufficient current is provided, a glow current can be maintained in small gaps. Otherwise, microdischarges with energies of

50 to 100  $\mu\text{J}$  occur between the electrodes in the dead time between sparks. Both the glow discharge and the microdischarges are too weak to ablate the electrodes, and can be neglected in terms of nanoparticle production. The microdischarges maintain an electron concentration that is sufficiently high to result in near instantaneous (non-stochastic) spark formation when  $S_1$  is closed. The lack of a spread in formative time lag in principle allows the discharges of multiple spark generators to be accurately timed at high repetition rates. This could prove particularly useful in limiting electrostatic losses when using multiple electrode pairs in series, e.g. when coating nanoparticles by spark discharge (chapter 7).

The sparks of the new spark generator are essentially identical to the oscillating discharges of the conventional circuit. The relatively low operating voltage of 1.5 kV requires the use of a larger capacitance to obtain the same spark energy, resulting in a resonant frequency of the circuit lower than that of the reference spark. Increasing the operating voltage to 3 to 5 kV, possibly by stacking IGBTs in series, would be an important improvement on the current prototype allowing a wider range of spark conditions to be used.



## Chapter 3

# Nanoparticle Production with a 25 kHz Spark Generator

**T**HE SPARK GENERATOR CIRCUIT of chapter 2 was used to produce nanoparticles in a newly developed setup. A nanoparticulate mixture of  $\text{Nb}_2\text{O}_5$  and  $\text{NbO}_2$  was formed from metallic Nb rods. The energy efficiency ( $1.4 \times 10^{-9} \text{ mol J}^{-1}$ ), particle size (5.7 nm) and morphology (open fractal-like) are similar to those obtained with the classic circuit, despite the increased power input.

Minimum flow conditions for high repetition rate sparks are formulated, which allow each spark to be considered as an individual event, and allow for sufficient heat dissipation. Future improvements that will allow the production of air-sensitive materials are presented.

### 3.1 Introduction

The spark generator described in chapter 2 allows more energy to be pushed into a spark gap, increasing the evaporation rate of a single electrode pair. To maintain product properties, other parameters need to scale correctly with the increased energy input. This chapter discusses these scaling aspects, and describes the setup built to test particle production with the new electric circuit.

With the 1.5 kW circuit of chapter 2, we can compare the spark to atmospheric arc discharges, which have typical power inputs of 0.01 to 25 kW [65]. Arc discharges are continuous plasmas, and as such have much slower cooling rates than the short sparks. As a result, particles produced by high power arc discharges are larger, with broad size distributions. For this reason it is desirable to keep each spark as an independent spark event.

Primary particles form by nucleation and condensation of the vapour formed by the spark, followed by coagulation and coalescence into aggregates and agglomerates. The particle concentration in the vapour/aerosol cloud is the principal parameter controlling condensation and coagulation [66]. Coalescence in turn depends on the time-temperature history of the aggregate [54]. This means that increased dilution is required in order to maintain the desired small particle size.

The aim of this chapter is to provide a set of guidelines for the scaled production of nanoparticulate materials by spark discharge. The first results of  $\text{NbO}_x$  particles produced with the new spark circuit are presented, and evaluated in terms of equivalency with the classic circuit.

### 3.2 Theory

We consider three constraints when scaling up particle production with spark discharge:

1. Sparks are independent,
2. Specific energy stays constant,
3. Specific power stays constant.

By independent sparks we mean that the vapour cloud by each spark is transported out of the gap before the next spark triggers. By treating each spark as an independent particle production event process development is greatly

simplified, as products can developed at the scale of a single spark. In an independent spark, the specific energy, i.e. the energy put into the spark volume, determines the formation of the metal vapour cloud. Because particles in spark discharge form by coagulation, keeping the initial vapour cloud conditions constant will result in an unchanged growth of the primary particles. Finally, scaling the power input with the quench flow rate, i.e. keeping a constant overall dilution, will result in a comparable agglomerate growth.

The vapour cloud formed by a spark must be removed from the gap before the subsequent spark can start. This condition is met if the distance traveled in the time between sparks is greater than the electrode diameter

$$d_{\text{el}} < v_{\text{gap}} f_{\text{rep}}^{-1}, \quad (3.1)$$

where  $v_{\text{gap}}$  is the gas velocity in the gap. Using 6 mm diameter electrodes operation at the maximum  $f_{\text{rep}}$  of 25 kHz a  $v_{\text{gap}} > 86 \text{ m s}^{-1}$  is required. This velocity is at the practical limit for gas flow of 30% of the speed of sound [67], and higher spark repetition rates will require special attention to the quenching of the gap.

As a rough approximation, the reactor used here can be treated as a cylindrical flow path intersected by two electrode rods. If the gap is centered on the axis of the cylinder, and the gap distance is much smaller than the reactor chamber, the velocity in the gap is equal to the maximum velocity of the parabolic flow profile, i.e.  $v_{\text{gap}} = 2\bar{v}$ . The mean velocity of the quench gas is

$$\bar{v} = \frac{4Q_{\text{q}}}{\pi d_{\text{r}}^2}, \quad (3.2)$$

where  $Q_{\text{q}}$  is the quench flow rate, and  $d_{\text{r}}$  is the inner diameter of the cylinder. Combining Equation 3.1 and Equation 3.2 provides the criterion for independent sparks:

$$\frac{Q_{\text{q}}}{f_{\text{rep}}} > \frac{\pi}{8} d_{\text{el}} d_{\text{r}}^2 \quad (3.3)$$

For the 38 mm piping and 6 mm electrodes used here, Equation 3.3 reduces to

$$\frac{Q_{\text{q}}}{f_{\text{rep}}} > 3.40 \times 10^{-6} \text{ m}^3. \quad (3.4)$$

At the 25 kHz upper limit of the circuit (chapter 2), a minimum flow rate of  $8.5 \times 10^{-2} \text{ m}^3 \text{ s}^{-1}$ , or  $5.1 \text{ m}^3 \text{ min}^{-1}$ , is required.

The flow rate is often limited by practical or economic constraints, as bigger pumps are needed to overcome the increasing pressure drop over the

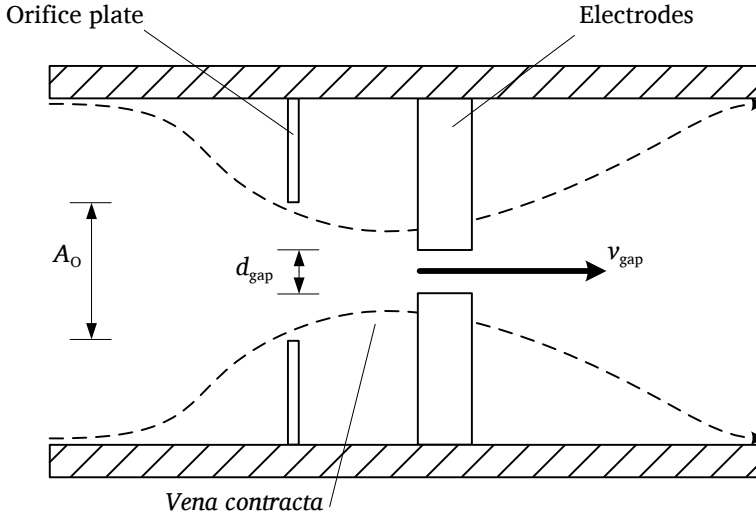


FIGURE 3.1 Schematic representation of flow focusing using an orifice.

system. For turbulent flow, the flow rate through an orifice is given by Hinds [66]:

$$Q = kA_O \sqrt{\frac{2 \Delta p}{\rho_g (1 - (A_O/A_{\text{tube}}))}}, \quad (3.5)$$

where  $k$  is a discharge coefficient ( $\sim 0.62$ ),  $A_O$  and  $A_{\text{tube}}$  are the cross-sectional areas of the orifice and the tube, respectively,  $\rho_g$  is the gas density, and  $\Delta p$  is the pressure drop over the orifice.

Lower flow rates can provide the required velocity if the gas flow is focused into the gap with an orifice or a nozzle (Figure 3.1), increasing  $v_{\text{gap}}$  for a given flow rate. The flow passing through the opening  $A_O$  of the orifice contracts, causing an acceleration of the gas. If the flow is unobstructed, the flow profile is narrowest at the *vena contracta*, and the maximum velocity is obtained. Calculating the actual flow profile for an electrode pair placed downstream of the orifice is however problematic. The width of the electrodes is smaller than the orifice, allowing the gas to flow *around* as well as between the electrodes, which combined with a lack of rotational symmetry precludes the use of a 2-D simplification. Instead, assuming that the electrodes are sufficiently close to the orifice, we can get a rough lower estimate of the velocity by assuming the flow has not yet expanded to the dimension of the

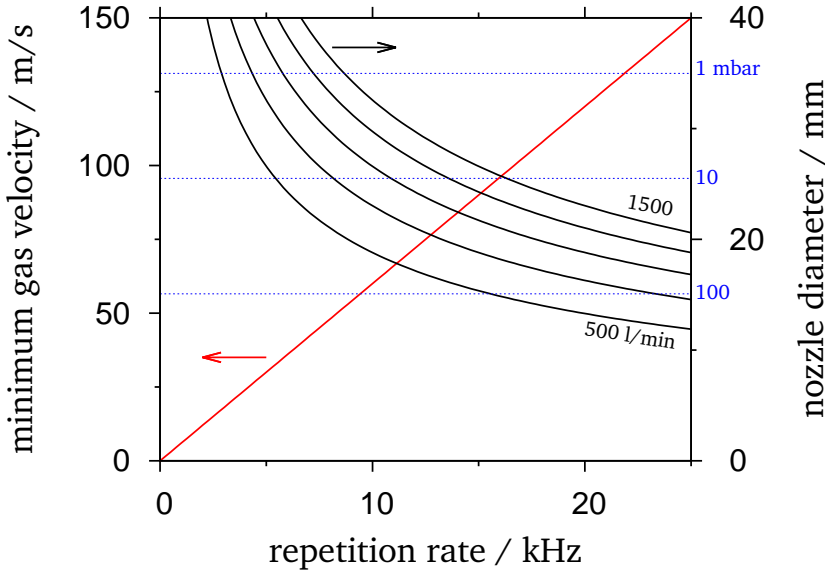


FIGURE 3.2 Flow requirements for independent sparks for 6 mm electrodes. Minimum required gas velocity (red) and minimum required orifice diameter for 250, 500, 750, 1000, 1250 and 1500 L min<sup>-1</sup> (black) vs repetition rate. The dotted horizontal lines indicate the pressure drop over the orifice at 750 L min<sup>-1</sup>.

orifice (see Figure 3.1).

$$v_{\text{gap}} \geq Q/A_{\text{O}} \quad (3.6)$$

Thus, sparks can be considered independent if

$$\frac{Q_{\text{q}}}{f_{\text{rep}}} > A_{\text{O}} d_{\text{el}} = \frac{\pi}{4} d_{\text{el}} d_{\text{O}}^2. \quad (3.7)$$

Figure 3.2 shows the orifice diameters required to achieve independent sparks for flow rates of 500 to 1500 L min<sup>-1</sup>. Running the spark at an  $f_{\text{rep}}$  of 25 kHz is feasible at these flow rates, but will require a pressure drop on the order of 100 mbar.

We can define the energy stored in the capacitor divided by the volume of the spark gap as a specific energy

$$E^* = \frac{E_{\text{spark}}}{V_{\text{spark}}} = \frac{\frac{1}{2}CU^2}{d_{\text{gap}}A_{\text{spark}}}, \quad (3.8)$$

where  $C$  is the capacitance,  $U$  is the voltage on the capacitor, and  $d_{\text{gap}}$  is the gap spacing.  $A_{\text{spark}}$  is the cross-section of the spark channel, and is not

directly accessible. If the peak current is known, as is the case with the spark generator of chapter 2, it can be derived from the current density of sparks, which is  $10^8 \text{ A m}^{-2}$  [24].

$$E^* = 10^8 \frac{\frac{1}{2}CU^2}{d_{\text{gap}}I_{\text{peak}}} \quad (3.9)$$

The specific energy determines the initial conditions of the plasma cloud, e.g. temperature and metal vapour concentration, and thus the formation of primary particles. Because the spark energy of the new circuit is independent of  $d_{\text{gap}}$ , the specific energy can be freely set – without modifying the electrical properties of the RLC discharge. This can be especially important for the synthesis of non-equilibrium phases or mixed materials [30].

After the spark has been quenched by dilution further growth of particles and agglomerates occurs by coagulation, which is governed by the particle number concentration. At high frequency in turbulent flow we can assume that the vapour clouds emitted by each spark are mixed to form a homogeneous aerosol shortly downstream of the spark. Analogous to  $E^*$  we can define a specific power  $P^*$  for the aerosol as

$$P^* = \frac{P_{\text{spark}}}{Q_{\text{quench}}} \left( = \frac{E_{\text{spark}}f_{\text{rep}}}{Q_{\text{quench}}} \right). \quad (3.10)$$

A high specific power results in a high aerosol loading, yielding faster agglomeration. Together with the characteristic sintering time of particles, this affects the structure of the agglomerates [68]. For noble metals of very small particle sizes, where sintering can occur at room temperature (see chapter 7),  $P^*$  controls the size of the primary particles [38].

### 3.3 Experimental

The reactor chamber is a five-way DN40CF cross, with two linearly adjustable, isolated high voltage electrodes and a view port. The spark generator circuit chapter 2 is powered by a 1.5 kV, 1.5 kW DC power supply (Technix SR1.5-P-1500). A 38 mm I.D. closed loop flow system sealed with DN40KF flanges is used to provide a sufficient quench gas flow for the increased power input (Figure 3.3). Pressure and temperature of the gas are monitored before the spark and after the collection filter. Flow rates of 100 to 850 Lmin<sup>-1</sup> are achieved using a recirculating blower (Domel 791.3.232-210). The flow rate entering the reaction chamber is measured using a Venturi tube compensated for pressure and temperature. A water cooled aluminium heat exchanger is used to remove heat generated by the blower and the spark.

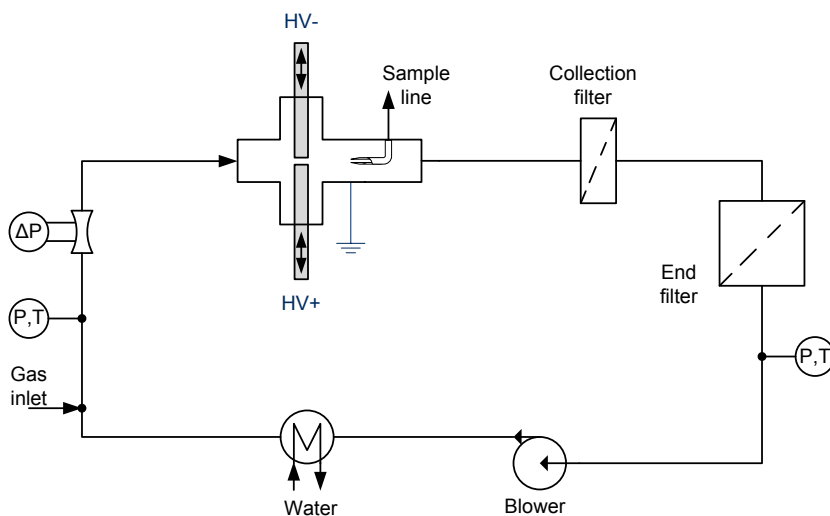


FIGURE 3.3 Process schematic of the closed loop spark generator.

A sharp pitot type sample tube with an inner diameter of 3 mm placed 91 mm downstream of the electrode axis allows the produced aerosol to be sampled for online analysis, e.g. by a differential mobility analyzer. The pitot tube is aligned coaxially with the 38 mm pipe. The flow rate out of the sample tube is set by flowing in fresh gas after the blower. For the current chapter, non-purified gases of 5.0 purity were used. Particles are collected on a 90 mm collection filter (Millipore HVHP09050) for gravimetric analysis and off-line

TABLE 3.1 Operating conditions and production rate data for production runs with niobium.  $d_{\text{gap}} = 0.5$  mm.

I.D. #	$f_{\text{rep}}$ kHz	$U_s$ kV	$P_s$ W	$Q_{\text{quench}}$ $\text{m}^3 \text{min}^{-1}$	$\dot{m}_{\text{filter}}$ $10^{-6} \text{g s}^{-1}$	$\dot{m}_{\text{electrode}}$ $10^{-6} \text{g s}^{-1}$	$Q/f_{\text{rep}}$ $10^{-6} \text{m}^3$
1	1.00	1.50	67.5	0.20	0.8	-	3.3
2	2.00	1.50	126	0.13	0.8	-	1.1
3	8.00	1.00	205	0.10	6.4	-24.6	0.2

characterization. A HEPA filter (Camfil Megalam MD14 305 mm  $\times$  305 mm) is used as a particle dump to protect the blower.

Powder X-ray diffraction analysis was performed in 0.5 mm capillaries on a PANalytical Xpert-PRO using Cu-K $\alpha$  radiation. TEM samples were prepared by gently scraping the TEM grid over the powder on the collection filter, before imaging on a FEI Tecnai TF20 electron microscope operated at 200 kV.

### 3.4 Results

At high power inputs and low quench gas flow rates, the electrode surfaces start melting and deform. At flow rates below roughly  $10 \text{ L min}^{-1}$  a protrusion starts growing from the liquefied anode surface towards the cathode, as also observed for glow and arc discharges [69]. The spark localizes around this protrusion, enhancing its growth until it eventually forms a short-circuiting bridge between both electrodes.

At higher flow rates no bridging occurs between the electrodes, but evidence of melting was found when inspecting the electrodes after use (Figure 3.4). The white glassy structure observed on an insufficiently cooled electrode tip (Figure 3.4b and 3.4c) is brittle, and can be scraped from the metal rod with little effort. If less power, or sufficient quenching is applied, a smoother surface is obtained (Figure 3.4a).

Light-grey Nb powders were collected during three production runs, listed in Table 3.1, with respective run times of 113 min, 236 min and 113 min. The quench flow rate was limited to  $\approx 200 \text{ L min}^{-1}$  by the large pressure drop over the collection filter, providing insufficient cooling for collection runs at repetition rates  $> 8 \text{ kHz}$ . The particle collection efficiency for run #3 was 25%. The powder X-Ray diffraction pattern of the sample of run #1 shows nearly fully oxidized Nb, with an approximate composition of 90% Nb<sub>2</sub>O<sub>5</sub>

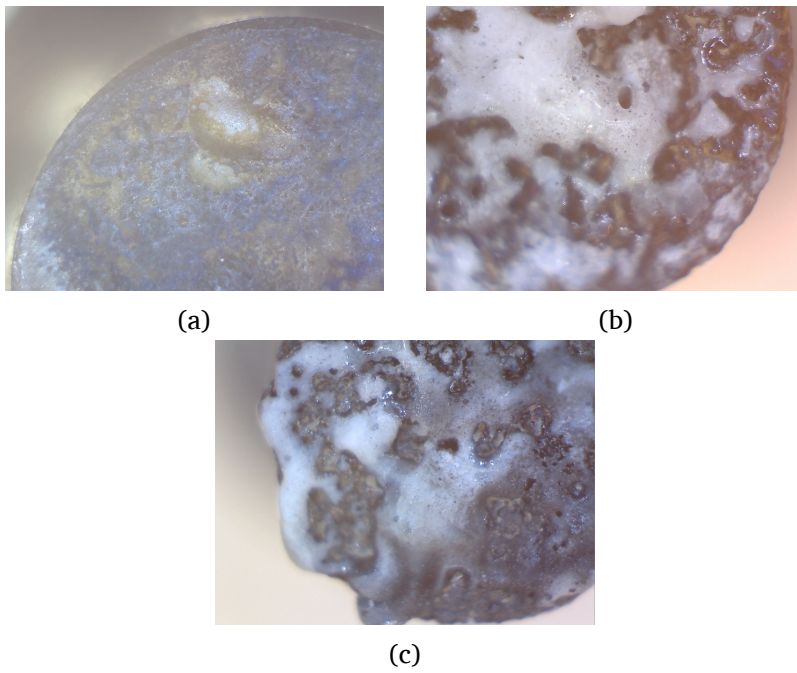


FIGURE 3.4 Optical micrographs of a  $\varnothing 6$  mm Nb cathode after use in a quench flow of Ar. (a)  $130 \text{ L min}^{-1}$ , 1.5 kV, 2 kHz. (b)  $100 \text{ L min}^{-1}$ , 1.0 kV, 8 kHz. (c) anode under conditions of (b).

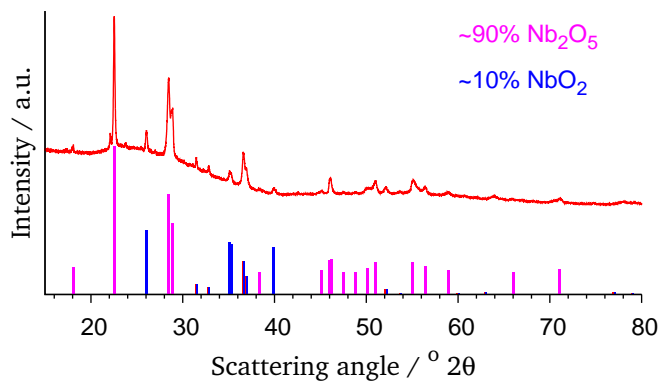


FIGURE 3.5 XRD of nanoparticles produced from Nb rods.

[ICCD, 04-007-0752] and 10 % NbO<sub>2</sub> [04-007-1440]. Metallic Nb was not found. Using Scherrer's equation with  $k = 0.9$ , crystallite sizes ranging from 12 to 66 nm (NbO<sub>2</sub>) and 13 to 104 nm (Nb<sub>2</sub>O<sub>5</sub>) were estimated from the X-ray diffraction patterns.

TEM micrographs show fractal-like, open agglomerates (Figure 3.6a). The size distribution of the primary particles, obtained from several micrographs, can be described with a lognormal distribution with a  $\bar{d}_p$  of 5.7 nm and a  $\sigma_g$  of 1.59 (Figure 3.6b). The sample could not be imaged at high resolution due to the poor conductivity of the oxidized sample.

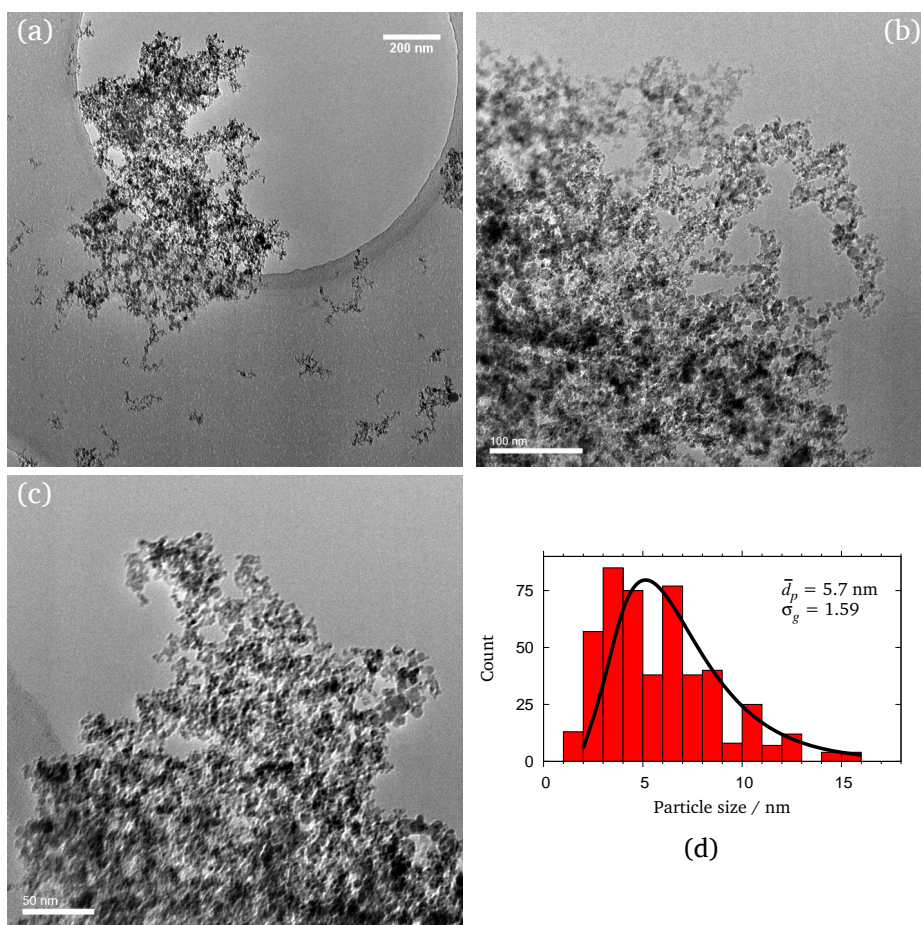


FIGURE 3.6 TEM micrographs of NbO<sub>x</sub>. (a-c) Micrographs with 200 nm, 100 nm and 50 nm scale bars, (d) Size distribution of primary particles ( $N = 483$ ).

### 3.5 Discussion

The small primary particle size and the morphology of the agglomerates obtained with the new spark circuit are comparable to those of the classic circuit. Tabrizi, Ullmann, Vons, et al. measured ablation efficiencies of  $1.1 \times 10^{-9} \text{ mol J}^{-1}$  at a specific energy of  $\sim 1.4 \times 10^7 \text{ J m}^{-3}$  and a specific power of  $1.8 \times 10^5 \text{ W s m}^{-3}$  [42]. The ablation efficiency for the new circuit, calculated using  $P = f_{\text{rep}} E_{\text{spark}}$ , was slightly larger at  $1.4 \times 10^{-9} \text{ mol J}^{-1}$ , at a specific energy and power of  $2.7 \times 10^7 \text{ J m}^{-3}$  and  $1.1 \times 10^5 \text{ W s m}^{-3}$ , respectively.

The increased ablation efficiency follows from the increased specific energy. Tabrizi, Ullmann, Vons, et al. show that the ablation efficiency has an inverse relation with the gap length [42]. By reducing the gap length, the volume in which the spark dissipates its heat changes. The temperature in the spark will reach a plateau value, after which the plasma channel expands [29]. Because less energy is needed to heat the plasma to its plateau, more energy is available to expand and sustain the plasma channel. As a larger area of the electrode is heated, more mass can be ablated at the same energy cost.

#### 3.5.1 Electrode melting

The glassy deposit on the Nb electrodes (Figure 3.4b) is likely a niobium oxide, presumably  $\text{Nb}_2\text{O}_5$ , based on the powder XRD of the produced nanoparticles (Figure 3.5). Based on the melting points of Nb and  $\text{Nb}_2\text{O}_5$ ,  $2477^\circ\text{C}$  and  $1512^\circ\text{C}$  respectively, as well as the mild red glow along the length of the electrodes during operation, we can estimate the mean temperature near the tip of the rod to have been roughly 1500 to  $2000^\circ\text{C}$ . The partial melting of the electrodes is undesirable in view of process stability, and should be avoided. Thus, a much lower mean temperature than that of Figure 3.4b has to be achieved if one wants to spark less refractory metals at high power inputs.

Figure 3.2 shows that the flow rate of  $100 \text{ L min}^{-1}$  is too low to meet the flow criterion of Equation 3.4 for repetition rates in the kHz range. None of the three production runs meet the criterion of Table 3.1, but the melted oxide was observed only in run #3. From the measured peak current the diameter of the spark channel is estimated at 1.5 mm. While the flow rate in run #2 was insufficient to displace the vapour cloud across the electrode cross-section, the displacement did exceed the diameter of the spark channel.

Thus, if a subsequent discharge formed in the decaying space charge of its predecessor, its hot zone did not overlap that of the prior hot zone. In run #3, the displacement of the vapour cloud was less than the spark diameter, and the second spark would strike in essentially the same location. This leads to a local rise of temperature if the heat conductivity is insufficient to remove all of the spark energy.

In closed loop mode, the Domel blower achieved a flow rate of  $\sim 700 \text{ L min}^{-1}$  against a pressure drop of 100 mbar. From the measured pressure drop over the system, Equation 3.3, and Equation 3.5, it follows that the maximum achievable flow rate with this blower is  $\sim 15 \text{ kHz}$ . To improve cooling at the electrode tip, the gas flow must however be focused using a nozzle [22] or an orifice as described above. Another useful solution is to increase the thermal conductance of the electrodes by increasing the electrode diameter [69]. A third option is to use a magnetic field to displace the vapour cloud between sparks, in order to avoid local heating by successive sparks.

### 3.5.2 Oxidation

Despite being handled in a glove box with  $< 0.1 \text{ ppm O}_2$  and  $\text{H}_2\text{O}$  impurities, the particles were near fully oxidized. The measured  $\sigma_{g,p}$  of 1.59 is higher than the 1.34 to 1.45 typically found for metals [42], and can be understood in terms of slower sintering, e.g. via grain boundary diffusion or lattice diffusion [70]. This suggests that the oxides were formed during the initial stages of primary particle formation.

According to supplier specifications the Ar contained  $< 2 \times 10^{-4} \text{ mol m}^{-3}$  in oxygen impurities, resulting in a steady influx of  $3 \times 10^{-9} \text{ mol O}_2/\text{s}$ . The ablation rate of run #1 is estimated at  $3 \times 10^{-8}$  to  $7 \times 10^{-8} \text{ mol s}^{-1}$ , giving Nb:O ratios of 5:1 to 10:1. The oxygen impurities in the carrier gas are an order of magnitude short of the observed Nb:O ratio of 1:2.4. Instead, the oxygen impurities can be traced back to the recirculating blower, which has two potential weak seals: the axle bearings and the rotator housing. The rotator housing, not gas-tight from the factory, was sealed with a rubber sleeve. During operation, the heat from the blower resulted in noticeable degradation of the rubber. From the porous appearance of the rubber, combined with the increased temperature, the  $\text{O}_2$  permeation rate is estimated at  $> 5 \times 10^{-8} \text{ mol O}_2/\text{s}$  [71]. The rotator housing has been replaced with a gas tight aluminium housing, which is expected to significantly reduce the oxygen contamination in the system.

### 3.6 Conclusion

A setup for the scaled-up production of nanoparticles was developed. Using niobium as a test material we show that the reactor provides linear scaling of production rate, while maintaining the characteristic particle morphology of the spark. Extrapolating from the measured ablation rate of  $1.4 \times 10^{-9} \text{ mol J}^{-1}$  an ablation rate of  $6 \times 10^{-3} \text{ mol h}^{-1}$  is achievable if the circuit of chapter 2 is operated at 25 kHz.

Heat management is crucial when operating a high frequency spark generator. Two flow criteria must be considered: the overall gas flow must be sufficient to allow the heat generated in the spark to be dissipated, and sufficient gas flow must be pushed into the spark to minimize overheating of the electrode. Flow focusing is needed to ensure that the vapor cloud is removed from the spark gap before the next spark strikes. With the current blower, operation should be feasible up to repetition rates of  $\sim 15 \text{ kHz}$ .

Oxides of niobium were formed. The gas impurities of the gas are insufficient to explain the amount of oxide formed, and it is clear that the setup is not suitable for the production of air-sensitive nanoparticles. To achieve this goal, better sealing has been applied to the recirculating blower. Furthermore, the setup is being integrated into a glove box to allow the production and harvesting of air-sensitive materials.



## Chapter 4

# High-Purity Spark Discharge Silver Nanospheres as Plasmonic Scatterers in Thin-film Solar Cells

**S**PARK DISCHARGE and tube furnaces were studied as sources for plasmon resonant silver nanoparticles for use as scattering enhancers in PV solar cells. These scatterers can trap light within the plane of the solar cell, allowing thinner layers of photo-absorbing material to be used, with obvious economic benefits.

Size-selected Ag nanospheres formed by sintering of spark- or furnace-generated aerosols were deposited by electrostatic deposition. Optical tests were performed on transparent conductive substrates as well as complete single-junction cells.

With the spark, particles of higher purity were obtained in higher concentrations. The measured scattering efficiency was lower than predicted by Mie theory, and a red shift in resonance was observed. Both effects can be explained through chemical contamination, by NaCl for furnace-generated particles, and by Ag<sub>2</sub>S tarnish for particles stored in air. Particles embedded in a single junction micro-crystalline PV cell increase the short circuit current density by ~10 %, but provide no improvement in overall solar cell efficiency. Points for improvement in the solar cell manufacturing process are identified.

---

Parts of this chapter appear in T. V. Pfeiffer, J. Ortiz-Gonzalez, R. Santbergen, H. Tan, A. Schmidt Ott, M. Zeman, A. H. M. Smets. *Plasmonic nanoparticle films for solar cell applications fabricated by size-selective aerosol deposition*, Energy Procedia, accepted.

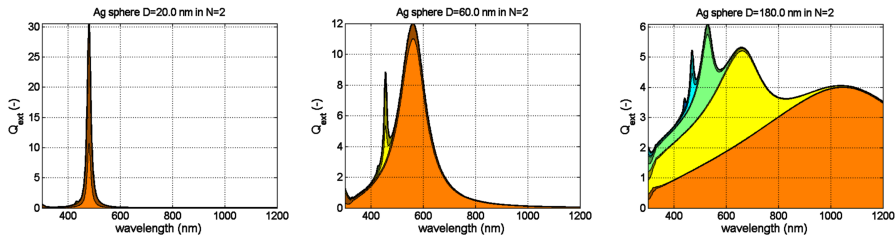


FIGURE 4.1 Calculated extinction efficiencies ( $Q_{\text{ext}} = Q_{\text{abs}} + Q_{\text{scat}}$ ) for (a) 20 nm, (b) 60 nm, and (c) 180 nm Ag nanoparticles embedded in a TCO of refractive index 2. Light and dark zones represent scattering and absorption, respectively. Colours represent different resonance modes. Reproduced from [73].

## 4.1 Introduction

Localised surface plasmon resonances (SPR) of metallic nanoparticles can trap incident light into a photo-absorbing layer [72], allowing the use of thinner, and therefore cheaper, solar cells. Silver spheres have large scattering cross-sections of up to ten times their geometric diameter, i.e. a 10% surface coverage is sufficient to couple all incident light into the solar cell. Moreover, Ag spheres scatter significantly more light than they absorb in the range of 60 to 180 nm (Figure 4.1). The calculations, based on Mie-theory, show that the primary resonance mode shifts from 480 nm to 1050 nm (i.e. a *redshift*) with increasing particle size, allowing the SPR to be tuned to the solar spectrum.

Production methods for plasmonic nanostructures should be able to process large surface areas at low cost, with good control of morphology, and at high purity. High-vacuum systems are often used to avoid contamination, and because many semiconductor layers are deposited in vacuum. They can be ordered structures, e.g. by nanoimprint lithography [74], or disordered structures, e.g. self-assembled metal-island-films [17]. Colloidal methods allow excellent control of particle size, and can self-assemble into ordered layers [75, 76]. The colloidal suspensions are however rich in contaminants, most notably the necessary surfactants, that can interfere with solar cell performance.

Spherical particles of controlled size can be generated and subsequently deposited on a flat substrate using aerosol methods [73, 77]. Silver is evaporated in a tube furnace at  $>1200$  °C, the vapour is left to nucleate and grow, and the resulting agglomerates are sintered to spheres in a second furnace.

Recently, using a temperature gradient to control the supersaturation of a seeded silver vapour, monodisperse ( $\sigma_g \leq 1.1$ ) spheres of silver were generated at high concentrations of  $5 \times 10^5 \text{ cm}^{-3}$  [78]. The nanospheres are then size-selected in a DMA, and deposited with an electrostatic precipitator. Surface coverages up to about 10 % can be achieved with electrostatic deposition, before agglomeration presents a problem [73, 77]. Because the particles are deposited in an inert atmosphere under ambient conditions, sensitive substrates can be used. This makes it possible to develop cell configurations where the plasmon scatterers are deposited *after* deposition of the solar cell.

High temperature (tube) furnaces have an intrinsic problem with contaminants due to the large surface area of the furnace walls. Both vapour pressure and diffusion coefficients follow an  $\exp(-T^{-1})$  relationship, resulting in a steady flux of contaminants from the tube material, and from its surrounding atmosphere. Impurities present in the tube walls can deplete over extended outgassing. However, permeation of external impurities present a constant source of contaminants. In particular oxygen, with a partial pressure of 200 mbar in ambient air and a diffusion coefficient of  $10^{-10} \text{ m}^2 \text{ s}^{-1}$  in  $\text{Al}_2\text{O}_3$  above  $1200^\circ\text{C}$  [79], will pass through the furnace walls. Hence the final product will often have a lower purity than the feedstock used, especially for refractory materials.

Localized heating using, e.g. arcs, electron beams, or induction heating, reduces this problem by lowering the heated area of the external surface. The crucible or mount that holds the feedstock does reach high temperatures due to conduction, and becomes a source of contaminants. In the typical design of spark discharge particle generators only the electrode tip is heated directly, making it possible to keep the temperature of all non-feedstock materials low.

## 4.2 Experimental

### 4.2.1 Deposition of Ag nanoparticles

Ag nanospheres were generated by sintering of agglomerates formed by evaporation/condensation (Figure 4.2). The vapour source was either a tube furnace (Vecstar VTF, 42 cm hot zone) at  $1380^\circ\text{C}$ , or the spark generator of chapter 2 running at 1.2 kV and 100 mA (3 kHz). A ceramic boat was filled with silver wire of 99.9 % purity (MaTeck, GmbH), and was placed in the middle of the hot zone of the 50 cm alumina furnace tube. The spark comprised two 99.995 % Ag rods of 7 mm diameter (MaTeck, GmbH). The quench

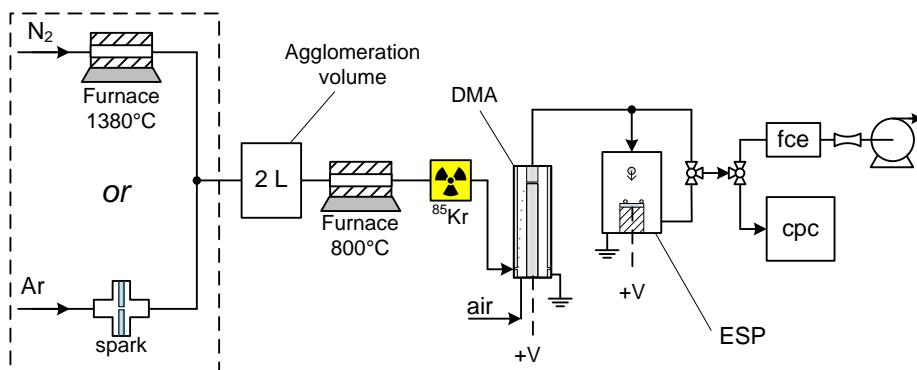


FIGURE 4.2 Schematic of the experimental setup.

gases were of 99.999% purity, with flows of  $1.8 \text{ L min}^{-1}$   $\text{N}_2$  for the oven and  $3.0 \text{ L min}^{-1}$  Ar for the spark. The aerosol was allowed to grow in a 2 L aluminium vessel, before sintering in a second tube furnace (Vecstar VCTF, 100 cm hot zone) fitted with a 140 cm alumina tube.

A bipolar charge distribution was applied to the sintered particles using a  $85 \text{ Kr } \beta^-$ -source (80 MBq). A Duisburg-type differential mobility analyzer (DMA) ( $L = 364 \text{ mm}$ ) was used for size measurement and selection. Particle concentrations were obtained with a home built faraday cup electrometer (fce), or a condensation/nucleation particle counter (cpc, Grimm 5.403). Size-selected nanospheres were deposited on various flat substrates in a home-built electrostatic precipitator (ESP), consisting of a 100 mm inner diameter steel vessel and a grounded, axial 4 mm inner diameter inlet nozzle placed 70 mm above the 40 mm diameter deposition area at 7 kV. The collection efficiency in the ESP was  $>92\%$  for particles up to 118 nm, measured by comparing the outlet concentration with or without the electric field applied.

#### 4.2.2 Thin-film solar cells

Single-junction photovoltaic (PV) cells were assembled on glass substrates in multiple deposition steps (Figure 4.3). A cell array consisting of 4-8 square,  $16 \text{ mm}^2$  solar cells was deposited on each substrate. First, aluminium-doped zinc oxide (AZO), a transparent conductive oxide, was deposited using RF-magnetron sputtering with a ZnO target comprising 2% m/m  $\text{Al}_2\text{O}_3$ . The AZO-coated glass substrates were removed from vacuum, and either coated with nanospheres as described in subsection 4.2.1, or left untreated for use

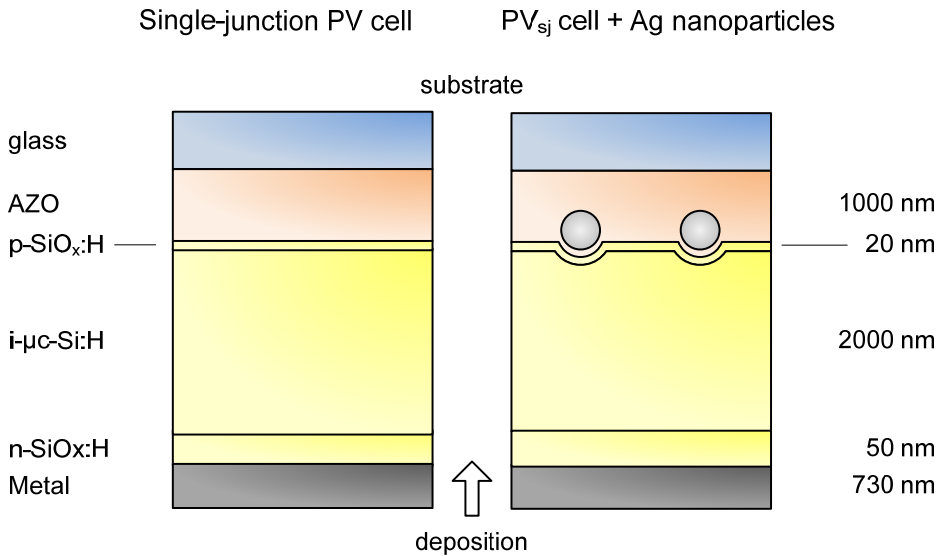


FIGURE 4.3 Solar cell configuration, *left*: reference cell, *right*: cell with embedded Ag nanospheres.

as reference cells. Two particle sizes, 104 nm and 120 nm, were embedded in the solar cells, with surface coverage  $>10\%$ .

On top of this a p-i-n micro-crystalline Si:H solar cell was deposited [80]. The doped SiO<sub>x</sub>:H layers were deposited using RF plasma-enhanced chemical vapour deposition (RF-PECVD) at 13.56 MHz. The i-μc-Si:H layer was deposited using very high frequency (VHF) PECVD at 40.68 MHz. The back reflector was deposited by physical vapour deposition (PVD) of Ag.

#### 4.2.3 Characterization

Optical characterization was performed on Ag nanospheres deposited on glass or glass coated with 20 to 80 nm conductive indium tin oxide (ITO). Absorption and scattering measurements were performed with an Elmer Lambda 950 spectrophotometer with a 150 mm integrating sphere. EQE and JV-curves were recorded under AM1.5,  $100 \text{ mW cm}^{-2}$ .

The scattering and absorption cross-sections of the deposited particles were modeled using Mie theory. The cross sections averaged over particle size distributions obtained from SEM measurements were calculated using the Mieplot (v4.3) implementation of the BHMIE algorithm [81, 82]. The

simulations for Ag-Ag<sub>2</sub>S core-shell particles were performed using the Matlab package MatScat [83]. Literature values were used for the optical constants of Ag [84] and Ag<sub>2</sub>S [85].

Particle size distributions and surface coverage were determined on glass/ITO or on Si wafer using a Hitachi S-4800 Scanning electron microscope (SEM). Image analysis was performed using the ImageJ software package [86]. Over  $>100 \mu\text{m}^2$  was analysed per sample, and size distributions were determined from 250 to 1500 particles, depending on surface coverage. The measured surface areas were converted to surface equivalent particle size by assuming circularity. Particles with circularities  $\leq 0.7$  are considered agglomerates, and are excluded when primary particles are discussed. Energy dispersive spectroscopy (EDS) was performed on a JEOL JSM-6010LA. To obtain a sufficient signal, spot analyses were performed on agglomerates.

## 4.3 Results

### 4.3.1 Aerosol production

Figure 4.4 compares the mobility size distributions (PSD) of the two particle generators under conditions used for deposition. The PSD for the spark is cut off at 105 nm due to the lower dielectric strength of Ar. In both cases, similar size distributions with a modal size of 60 nm were obtained. The broader size distribution of the spark is a result of the shorter residence time. Both the furnace and spark have a comparable production rate, yielding concentrations on the order of  $10^5 \text{ cm}^{-3}$  of size-selected particles in the range of 80 to 120 nm.

The variation in particle concentration from the spark generator is in part caused by the continued erosion of the electrodes. During a typical 2.5 h deposition run the measured concentration drops to about 70 % of the initial value, as represented by the error bars in Figure 4.4. To compensate for this drop the electrode spacing was adjusted between production runs; in principle this could be done in real-time, as is done in commercial spark generators [87]. The furnace had a drift of only a few percent, but showed a significant drift from day to day. To compensate for this drift the furnace tube needed to be periodically cooled and dismantled in order to replenish the silver stock.

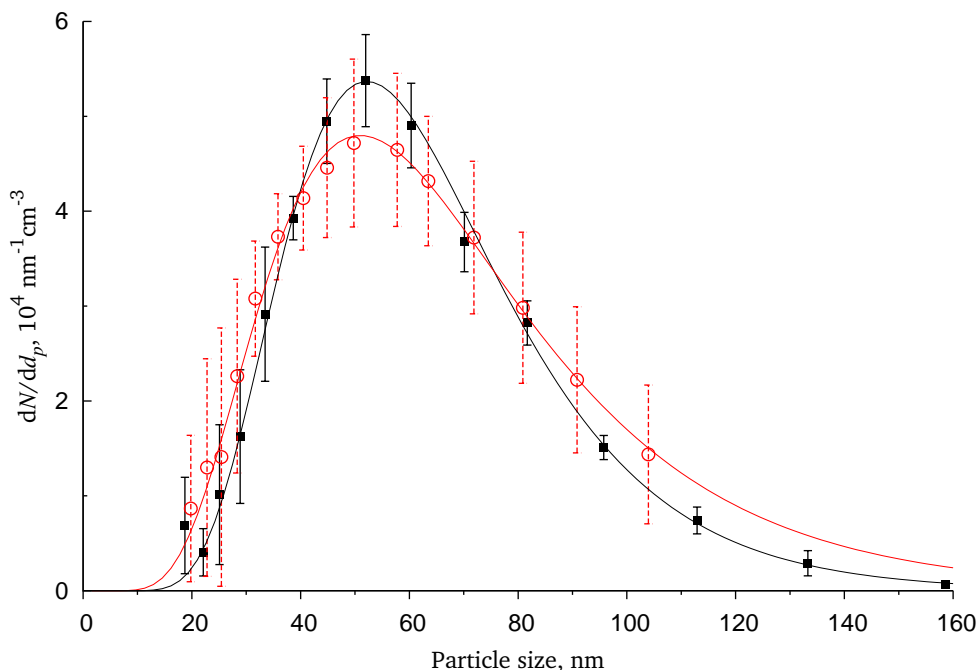


FIGURE 4.4 Averaged mobility size distribution of sintered agglomerates produced by tube furnace,  $1.8 \text{ L min}^{-1} \text{ N}_2$ ,  $T_{\text{sint.}} = 750 \text{ }^\circ\text{C}$  (black squares), and spark discharge,  $4 \text{ L min}^{-1} \text{ Ar}$ ,  $T_{\text{sint.}} = 800 \text{ }^\circ\text{C}$  (red circles). Lognormal curves are optical fits.

#### 4.3.2 Films of deposited Ag nanospheres

Aggregation should be avoided during deposition, because the strongest SPR enhancement is expected when monodisperse particles are homogeneously distributed on the substrate [17]. Following the method of Krinke, Deppert, Magnusson, et al. [88] for a particle approaching a deposited particle we find that the attractive forces, in particular the van der Waals force, exceed the repulsive Coulombic force for 100 nm particles carrying 1 to 3 charges. Considering that the goal is to deposit onto (semi-)conductive substrates, which allows deposited particles to dissipate their charge, it will not be feasible to use electrostatic repulsion to avoid particle contacts.

The attractive forces start to play a role when the particles are a few diameters apart. Before that, Brownian motion dominates the particle trajectories, resulting in a random deposition at low surface coverage. Figure 4.5(a-c)

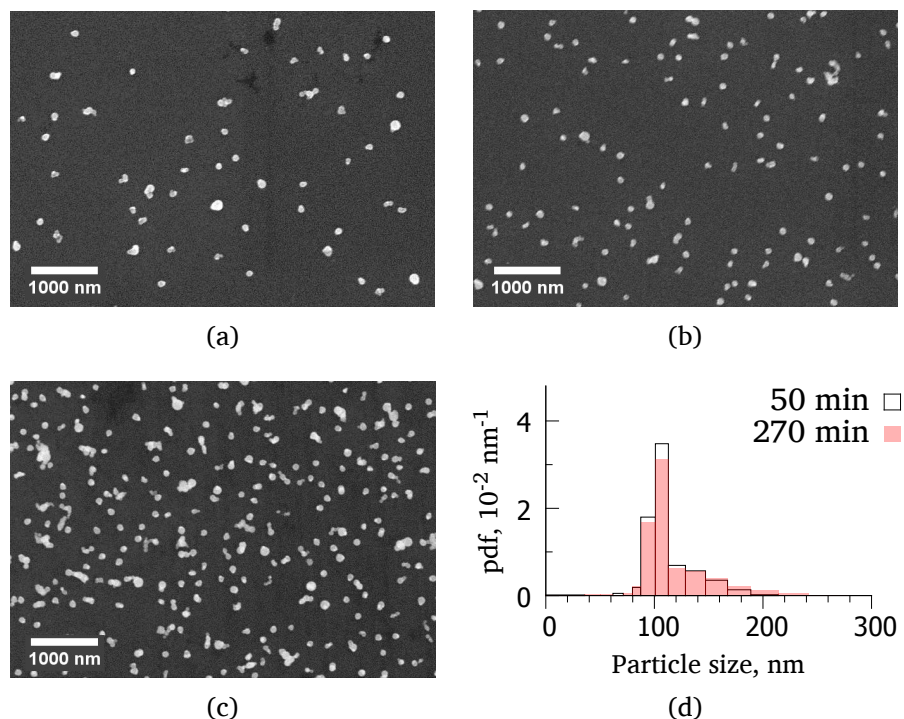


FIGURE 4.5 SEM micrographs of furnace-generated Ag nanoparticles for deposition times of (a) 50 min, (b) 90 min, and (c) 270 min. (d) particle size distribution for deposition times of 50 min (open bars) and 270 min (filled bars).

shows oven-generated Ag particles on a Si-wafer after deposition times of 50 min, 90 min and 270 min. The surface coverage grows consistently with the incoming particle flux at  $2.4\% \text{ h}^{-1}$ , from 2.3% after 50 min to 10.8% after 270 min deposition. The Ag particles are randomly distributed across the surface, and have a modal size of 107 to 110 nm (Figure 4.5d). They comprise single particles, doublets and small agglomerates. The second mode around 150 nm represents both doubly charged particles that passed through the DMA, and agglomerates that formed on the Si surface during deposition. Assuming that the 110 nm particles left the neutralizer with the equilibrium charge distribution [89], surface agglomerates represent  $\sim 5\%$  of the surface domains.

Figure 4.6 shows both single and agglomerated spark-generated spheres on Si with a modal size of 85 nm. The agglomerates are mainly composed of touching spheres, i.e. the formation of sintering necks was rarely observed.

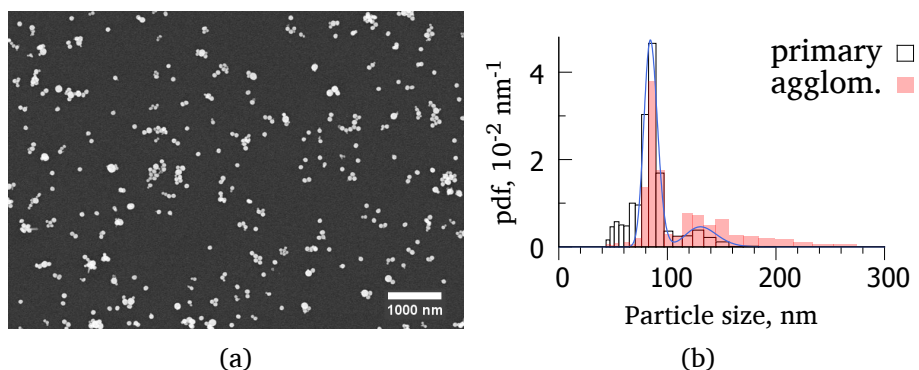


FIGURE 4.6 Deposited Ag nanoparticles produced by spark discharge. (a) SEM micrograph, (b) corresponding size distribution of primary particles (open bars) and agglomerates + singlets (filled bars). The blue curve is a lognormal fit of the primary particle data (see text).

This indicates that the agglomerates formed after the sintering oven, either in flight, or on the substrate surface. For the primary particle size data in Figure 4.6b, each agglomerate was cut into its constituent spheres<sup>1</sup>. A bimodal, lognormal distribution was then fit by ignoring particles smaller than the DMA size interval, where the second mode represents larger, doubly charged particles with the same mobility that pass through the DMA, taking slip correction [66] and the equilibrium charge distribution [89] into account.

5 to 8% of the particles are too small to have passed through the DMA by themselves, and passed through the DMA as part of an agglomerate. The observed lack of sintering indicates that these agglomerates formed by coagulation downstream of the sintering furnace, but before the DMA. This effect can be reduced by lowering the concentration entering the sintering furnace (here  $>10^7 \text{ cm}^{-3}$ ) by placing a first DMA between the agglomeration chamber and the sintering furnace, at the expense of a broader distribution towards larger sizes [77]. It is of course possible to use two DMA's, one before and one after the sintering furnace, to achieve an even narrower distribution than achievable with either method.

The maximum attainable surface coverage is limited by agglomeration, as the likelihood that the moving particle comes close enough to a deposited particle increases with the number of deposited particles [88]. For the 85 nm

<sup>1</sup>Using ImageJ's 'watershed' function. Resulting particles with circularity  $<0.7$ , i.e. incorrectly cut doublets, were discarded.

TABLE 4.1 Overall molar composition<sup>a</sup> of Ag nanoparticles as determined by EDX.

Element	Oven	Spark
Ag	51–73%	84–87%
Na	0–7%	0–1%
Cl	11–34%	1–2%
S	0–3%	10–12%
O <sup>b</sup>	13–23%	0–1%
Al	0–1%	0% <sup>d</sup>
metals <sup>c</sup>	0–1%	n.d.

<sup>a</sup> Excluding Si and C.

<sup>b</sup> Accompanied by additional C.

<sup>c</sup> Mg, K, Ca and Cu.

<sup>d</sup> Below quantification limit.

particles in Figure 4.6, agglomerates comprise about half of the observed particles. Once several deposited particles form a small agglomerate, the increased surface area represents a sink for an approaching particle analogous to bimodal coagulation (see chapter 7). This makes it more likely for an incoming particle to deposit *on*, rather than next to an existing agglomerate. After 270 min deposition the modal size has dropped a bit when compared to 50 min deposition, while the fraction of surface agglomerates, i.e. particles >150 nm, has increased. As the area of interest is the surface plasmon resonance of discrete nanospheres, we did not work with surface coverages above ~10%.

The elemental composition of spark- and furnace-generated particles is given in Table 4.1. Furnace-generated particles contain 51 to 73% Ag, as well as significant fractions of Na and Cl, as well as trace ≤1% impurities of Mg, Al, S, K, Ca and Cu. The detection of O consistently coincided with an enhanced carbon signal, suggesting the presence of some carbonate, e.g. Na<sub>2</sub>CO<sub>3</sub>. Table 4.1 and the following discussion do not include a noticeable fraction of micron sized particles with negligible Ag content, identified as ceramics of various composition. These ceramic particles were observed only for furnace-generated samples, and are considered to be debris from the porcelain boat that carried the silver aliquot, which cracked and shattered over the course of several heating cycles.

Spark-generated particles contain more Ag (84 to 87%), and S (11 to

13%), but significantly less Na and Cl than in furnace-generated samples. The trace metal impurities observed in furnace-generated particles could not be detected in the spark-generated samples.

Prior to EDX analysis, the samples had been stored in air for several months. Silver is known to form a tarnish of  $\text{Ag}_2\text{S}$  when exposed to ambient air containing traces of  $\text{H}_2\text{S}$  [90, 91], explaining the presence of sulfur in the samples. The furnace-generated particles likely contain  $\text{AgCl}$ , another known silver tarnish, that can form when Ag is exposed to ambient air containing traces of  $\text{Cl}_2$  or  $\text{HCl}$  [92]. All samples were stored in a single environment, making it unlikely that both  $\text{AgCl}$  and  $\text{Ag}_2\text{S}$  formed through air exposure. The low sulfur content in furnace-generated samples suggests that the particles were protected from sulfidation by a shell of  $\text{AgCl}$ .

The formation of  $\text{AgCl}$  is attributed to the presence of  $\text{NaCl}$  impurities in the evaporation furnace, which was operated close to the boiling point of  $\text{NaCl}$ . High temperature alumina and aluminosilicate tubes are known to result in contamination, specifically from organics [93], due to the exponential scaling of vapour pressure with temperature.  $\text{Na}_2\text{O}$  is a major impurity in alumina, originating from the Bayer process used in its production. Chlorine is not often cited as a known impurity, but  $\text{HCl}$  is used in the production of high-purity  $\text{Al}_2\text{O}_3$  in order to remove trace metal impurities [94]. One of the main uses of tube furnaces in aerosol sciences is to generate aerosols of  $\text{NaCl}$  [95]. Because the prior history of the used work tube<sup>2</sup> was unknown, it was thoroughly washed with demineralized water and ethanol to remove potential traces of  $\text{NaCl}$  prior to use.

The crucial difference between spark discharge and a furnace is the extremely localized heating [22]. According to the Hertz-Knudsen equation, the evaporation rate of a given material is proportional to the heated surface area, and –if a flow of gas transports evaporated material away from the heated surface– the temperature dependent vapour pressure [96]. The temperature in the spark is higher than the boiling point of any material, potentially allowing larger number of possible contaminating elements to be evaporated. The spark channel is several millimeters in diameter (chapter 2, resulting in heated surface area  $<1\text{ cm}^2$ ). The evaporation furnace was operated at a much lower temperature, near the boiling point of  $\text{NaCl}$ , and has a heated surface area in excess of  $300\text{ cm}^2$ , i.e.  $\sim 1000\times$  greater than that of the spark. When comparing expected contamination levels from the two

---

<sup>2</sup>An optically clean, supposedly unused spare tube, stored in an unsealed box in a lab occupied by aerosol scientists.

methods, one would expect spark-generated materials to contain more non-volatile compounds (WX, NbX, insofar as present), and furnace-generated materials to contain more volatile compounds (NaX, MgX). This is reflected by the presence of quantifiable trace metal impurities in furnace-generated, but not in spark-generated particles. The lower temperature in the sintering oven, near the melting point of NaCl, explains the low levels of Na and Cl in spark-generated samples.

High-purity tubes, combined with stringent cleaning protocols can be used to reduce contaminant levels. The impurities in the work tube will eventually deplete, allowing the production of clean silver. This can however take a long time, even with work tubes low on contaminants, when one considers the comparatively large size of the work tube in comparison with the silver aliquot.

#### 4.3.3 Economic evaluation

Both the furnace and the spark consume around 120 W, and yield a deposition rate of  $8 \times 10^{-9} \text{ m}^2 \text{ s}^{-1}$  on the  $1.25 \times 10^{-3} \text{ m}^2$  collection area of the ESP. This corresponds to a 75 % collection efficiency from aerosol to deposition surface in the ESP<sup>3</sup>. The energy cost for a silver particle film with 10 % surface coverage is  $1 \times 10^9 \text{ J m}^{-2}$ , or  $300 \text{ kW h m}^{-2}$ . This is significant when compared to the total (electrical equivalent) energy consumption during the complete life cycle of a PV solar cell (1 to  $16 \text{ kW/W}_{\text{peak}}$  [97], i.e. 150 to  $2400 \text{ kW h m}^{-2}$  at 15 % efficiency).

The ablation efficiency of silver by spark discharge is  $8 \times 10^{-10} \text{ mol J}^{-1}$  [42], meaning that only 0.8 % of the ablated mass ends up on the solar cell. The poor efficiency is the result of several loss mechanisms, some of which are easily reduced. Losses occur by diffusion of particles to the walls of the system, and can be estimated using the Gormley & Kennedy equation [66]. Diffusion losses are largest while the particles are small, or the temperature is high. Distinguishing between the coagulation chamber, the hot zone in the sintering furnace, and the rest of the system, transmission of particles is estimated at 97 % 95 % and >99 % respectively. The DMA was operated with a much lower aerosol flow rate than the furnace and spark. The excess gas was vented, yielding a transmission of 25 to 30 %. During size selection large and small fractions of the aerosol are discarded, yielding a mass transmission of 18 %.

---

<sup>3</sup>The solar cells used were typically  $3.1 \times 10^{-4}$  to  $3.6 \times 10^{-4} \text{ m}^2$ , yielding device efficiencies of 20 %

To accommodate for the observed deposition rate, particle losses in the spark generator chamber are placed on the order of 75 to 80 %. Particles can deposit on the reactor wall by either diffusion or electrostatic precipitation. Evaporated material can also deposit on the opposing electrode if the vapour jet formed by the spark bridges the electrode gap [42]. Without assigning specific values we assume that the three loss mechanisms are comparable in magnitude, i.e. all are significant. The specific energy (power input / flow rate) used here is one order of magnitude larger than typical spark systems. The comparatively low flow rate used here results in poor quenching of the vapour cloud, increasing the risk of material transfer between electrodes. The low flow rate also leads to increased diffusional and electrostatic losses.

Given that a complete PV cell can be assembled for less cost than the electrical cost of an SPR layer, adding an SPR layer with the current system would be viable the efficiency of the solar cell more than doubles. The losses in the spark chamber, in the excess vent, and in the DMA together result in 99 % reduction in aerosol mass. With an optimized design, particle losses in the spark can probably be reduced to <20 %.

The losses in the excess vent can be fully avoided if a high throughput DMA is used [98]. Some losses occur because not all the generated particles will be in the desired particle size range. If the aerosol is left to coagulate, it will approach the self-preserving size distribution with a geometric standard deviation,  $\sigma_g$ , of 1.32 to 1.36 [66]. For mass mean diameter close to 100 nm, this means that up to 30 % of the mass falls within  $(100 \pm 10)$  nm. If a monodisperse aerosol with an  $\sigma_g < 1.1$  is generated, e.g. by seeded nucleation [78], this value increases to 70 %. With the described improvements, the energy cost reduces to a more acceptable  $15 \text{ kW h m}^{-2}$  or  $6 \text{ kW h m}^{-2}$  for polydisperse and monodisperse generators, respectively.

#### 4.3.4 Optical properties

The measured cross-sections for scattering ( $Q_{\text{scat.}}$ ) and absorption ( $Q_{\text{abs.}}$ ) show red-shifts of the surface plasmon resonance compared to simulated spectra Figure 4.7. The red shifts were smaller for spark-generated particles:  $Q_{\text{scat.}}$  shifts by 60 nm and 90 nm, while  $Q_{\text{abs.}}$  shifts by 50 nm and 80 nm, for spark and furnace-generated particles, respectively. Additionally, the measured magnitude of  $Q_{\text{scat.}}$  and  $Q_{\text{abs.}}$  was lower than predicted from theory.

The red shift occurs in part because of a strong sensitivity to the refractive index of the medium in which the particle is embedded [77]; partly because of non-ideal sphericity of the particles [77]; and partly because of contaminants

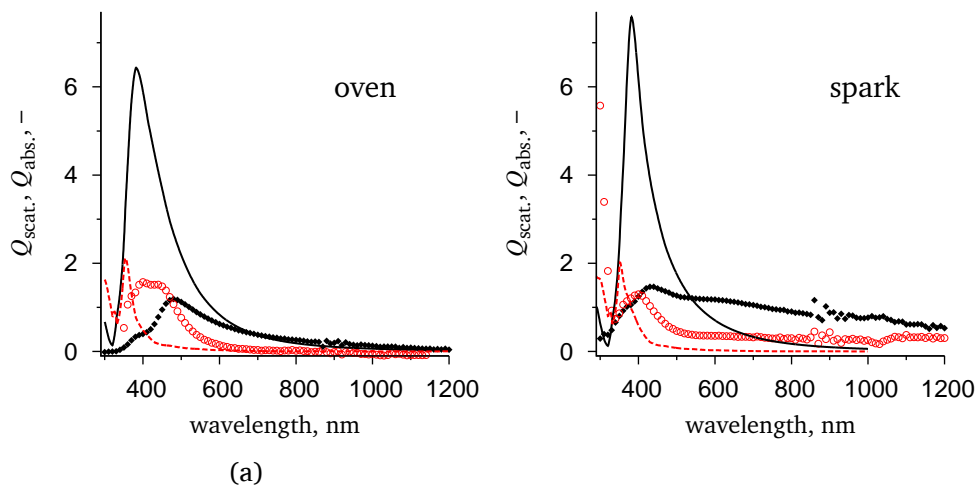


FIGURE 4.7 Measured (points) scattering (black) and absorption (red) cross-sections for silver nanoparticles, compared with simulated values (lines). (a) tube furnace,  $d_p = 107$  nm,  $\theta = 10\%$  (b) spark discharge,  $d_p = 84$  nm,  $\theta = 10\%$ .

in the Ag particles. McMahon, Lopez, Meyer III, et al. [99] observed a shift in the surface plasmon resonance of silver nanoparticle films deposited by ion-beam lithography, when the substrates were exposed to air. For 60 nm cylindrical silver particles they show a change in redshift of  $1.8 \text{ nm h}^{-1}$ , and link it to the observed formation of  $\text{Ag}_2\text{S}$ .

To simulate the effects on contaminants on the SPR of Ag nanospheres, we consider the formation of  $\text{Ag}_2\text{S}$  on the surface of silver exposed to air. Scattering cross-sections were calculated for Ag spheres with a constant diameter of 120 nm, of which the outer 0 to 15 nm was replaced by  $\text{Ag}_2\text{S}$ . A refractive index of 1 (air) was used for the medium. The simulations show a red shift of  $\sim 12$  nm for every nm shell thickness Figure 4.8 Additionally, the magnitude of  $Q_{\text{scat}}$  decreases, and that of  $Q_{\text{abs}}$  increases with increasing shell thickness. The drop in scattering intensity and the red-shift of spark generated particles, for which S is the dominant impurity, could be explained by a sulfide shell with a thickness of  $\sim 3$  nm.

Each optical measurement was performed one day after deposition. To confirm that tarnishing affects the scattering properties of the silver particles, the optical measurement of a furnace-generated sample was repeated 24 days after deposition (Figure 4.9). The observed red shifts in  $Q_{\text{scat}}$  and  $Q_{\text{abs}}$  are

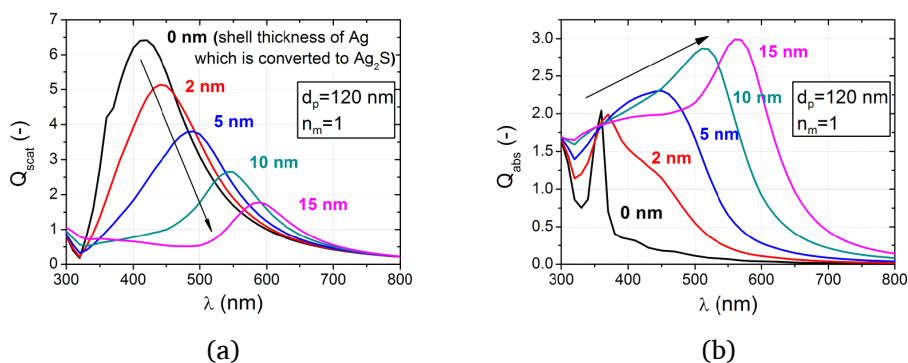


FIGURE 4.8 Simulated (a) scattering and (b) absorption by Ag nanoparticles surrounded by a shell of  $\text{Ag}_2\text{S}$ .

consistent in trend with a growing layer of  $\text{Ag}_2\text{S}$  (cf. Figure 4.8). However, the drop in intensity of  $Q_{\text{abs}}$  does not fit with the model. A decrease in absorption can be understood if the particles were not distributed homogeneously over the surface, and a different spot with lower surface coverage was lit in the repeat measurement. Additionally, the large fractions of Na and Cl in furnace-generated samples complicate the analysis, as it is possible that some conversion between Ag, NaCl and AgCl occurred.

$\text{Ag}_2\text{S}$  films formed in air by the reaction of Ag with  $\text{H}_2\text{S}$  can grow at a rate of 6 nm per month to  $10 \text{ nm h}^{-1}$  [90]. Such growth rates are in agreement with the  $\text{Ag}_2\text{S}$  thickness of  $\sim 3 \text{ nm}$  estimated from the optical measurement 24 hours after deposition. EDX measurements on 80 nm particles performed 260 d after deposition show a S content of 10 to 12 %, corresponding to a  $\text{Ag}_2\text{S}$  shell thickness of 9 to 12 nm. The S content of furnace-generated samples was too low to explain the SPR red shift by sulfidation. In stead, it is assumed that AgCl in the furnace-generated samples plays a similar role to  $\text{Ag}_2\text{S}$ .

#### 4.3.5 Solar cells

The spark-generated Ag nanoparticles result in a 4 to 15 % increase in short-circuit current density,  $J_{sc}$ , when placed in front of the solar cell (Figure 4.10). The Ag particles are embedded in AZO, with a refractive index of 2, resulting in a red shift and broadening of the surface plasmon resonance (Figure 4.10) compared to the samples measured in air (Figure 4.7b). The increased EQE at wavelengths above 600 nm is consistent with enhanced absorption due to light trapping. Integrated over the full spectrum, the individual cells

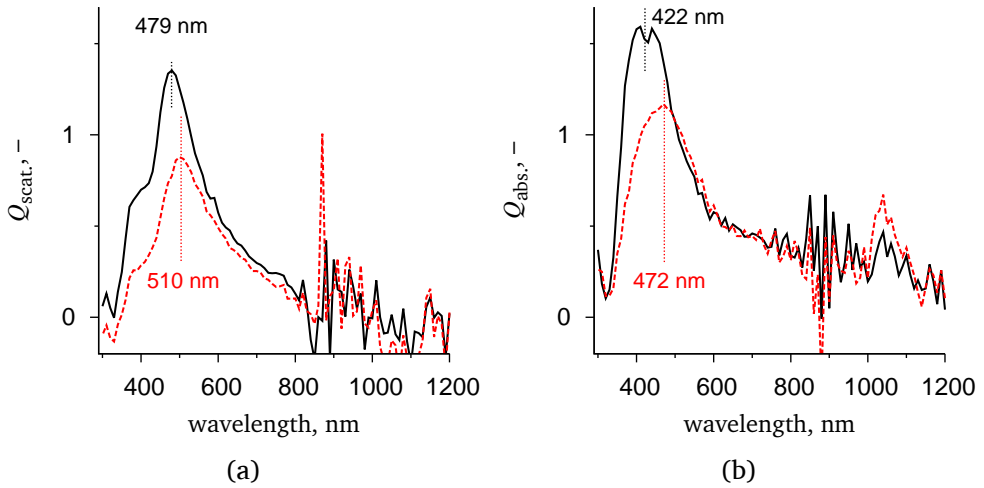


FIGURE 4.9 Age effect in scattering (a) and absorption (b) of 136 nm furnace-generated particles on glass/ITO, 1 d (black) and 24 d (red) after deposition.

showed a variation of  $\pm 1\%$  in  $J_{sc}$ . However, the cells comprising 120 nm particles showed a variation of several percent in EQE, specifically in the 400 to 600 nm spectral range. While this variation is probably linked to inhomogeneous deposition of Ag nanoparticles across the substrate, we have no suitable explanation for the small but definite increase in EQE observed for several cells in the range of 400 to 600 nm. In this part of the spectrum, the microcrystalline Si layer absorbs the light a single pass, and no EQE is to be expected from improved scattering.

The SPR-enhanced scattering results in an increased current density up to 0.4 V, above which the current density falls below that of the reference cell (Figure 4.11). The reduced  $V_{oc}$  is indicative of an increased number of electrical defects, causing an increased recombination of charge carriers. This limits the maximum power output of the cell, which is seen in the reduction of the fill factor from 69 to 61% (Table 4.2). Overall, the gain in current density is offset by the reduced fill factor, and the incorporated nanoparticles can be said to have a negligible effect on the efficiency of the solar cells.

The poor electrical performance of the solar cells is linked to the low shunt resistance,  $R_{SH}$ , and is explained through the surface texture of the samples. A high surface roughness leads to non-conformal growth of microcrystalline silicon, leading to the incorporation of voids and pinhole defects [100]. The samples were exposed to ambient air before depositing Si, and possibly col-

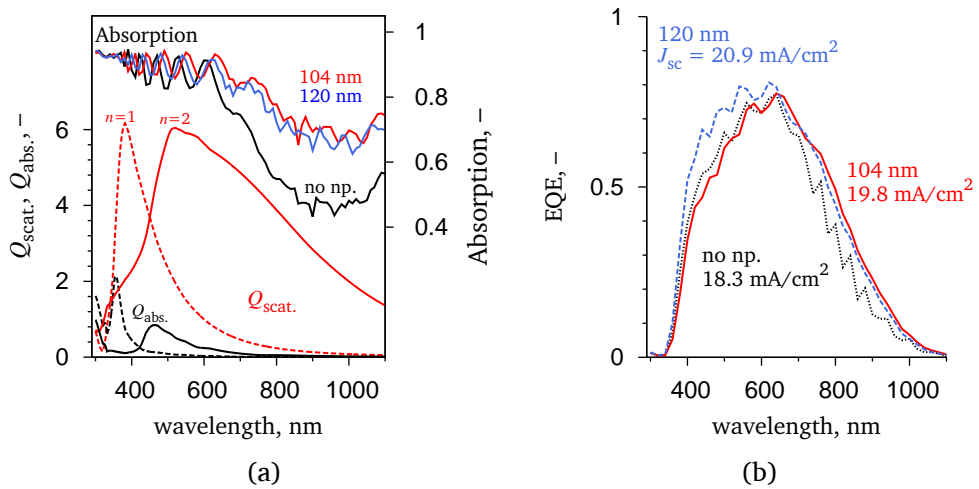


FIGURE 4.10 Wavelength dependent performance of single junction solar cells. (a) Measured total absorption and simulated  $Q_{\text{abs.}}$  and  $Q_{\text{scat.}}$  for 110 nm particles embedded in air ( $n_m = 1$ , dashed lines) and in AZO ( $n_m = 2$ , solid lines). Total absorption was measured in reflectance mode as  $1 - R$ . (b) Averaged external quantum efficiency at  $V_{\text{bias}} = 0 \text{ V}$  with corresponding  $J_{\text{sc}}$ .

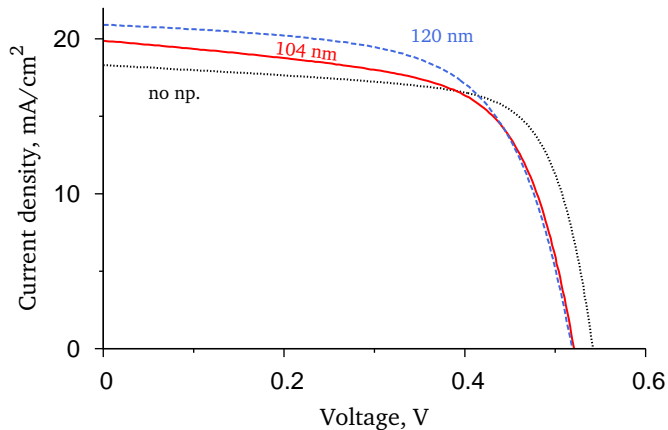


FIGURE 4.11  $JV$ -curves of assembled cells. The current densities are normalized to the EQE measurements.

TABLE 4.2 Summary of solar cell parameters. Surface coverage of nanospheres was  $\sim 10\%$

Parameter	unit	Reference	Cell 1	Cell 2
$d_p$	nm	-	104	120
$V_{oc}$	mV	541	518	511
$J_{sc}$	$\text{mA cm}^{-2}$	18.3	19.8	20.9
$FF$	%	69.0	61.3	60.7
$\eta$	%	6.9	6.5	6.8
$R_S$	$\Omega \text{ cm}^2$	3.1	2.6	3.9
$R_{SH}$	$\Omega \text{ cm}^2$	293	133	243

lected microscopic dust particles. SEM studies show that micrometer-sized Ag agglomerates were deposited alongside the  $\sim 100$  nm particles. These agglomerates are of the same order of thickness as the deposited Si film ( $2 \mu\text{m}$ ), and by themselves present additional shunt paths.

#### 4.4 Conclusions

Spark discharge presents a viable alternative to tube furnaces as a source of nanoparticulate aerosols, providing comparable production rates, and with the possibility for higher purity particles. Optimization of the process to reduce particle losses can reduce the energy cost of a silver nanoparticle layer with 10% surface coverage to  $\leq 15 \text{ kWh m}^{-2}$ . Combined with the absence of masks, precursors and solvents, and the fact that spheroid particles are deposited, the aerosol methods present a unique alternative to metal-island-films and ion beam lithography in the production of nanostructured, surface plasmon resonant films.

Impurities in the nanoparticles lead to a shift in the surface plasmon resonance, and reduce the amount of scattered light. Spark-generated nanoparticles are of higher purity than furnace-generated particles due to the localized heating. When the deposited particles are left exposed to air a shell of  $\text{Ag}_2\text{S}$  forms, resulting in a redshift of the SPR. In large scale assembly of PV cells it is common practice to avoid exposure to ambient air, and the  $\text{Ag}_2\text{S}$  tarnish will not form. In contrast, oven-generated particles were contaminated by a large fraction of the volatile NaCl, originating from trace compounds in the tube wall. While careful selection and production of tube materials

can reduce this type contamination, the fundamental flaw of a large heated surface area will remain.

The benefit of the surface plasmon resonant nanospheres, an increased photocurrent, is offset by the poor electrical properties of the deposited cells. To improve the electrical properties, the presence of micrometer size structures must be avoided. Primarily, the particle deposition step should be included in the overall process design so that the currently necessary vacuum break can be avoided. At the very least, exposure to ambient air must be prevented in order to avoid tarnishing of the silver nanospheres. If air exposure cannot be avoided, methods to reduce  $\text{Ag}_2\text{S}$  to Ag should be developed. Further work to find methods to reduce the size of formed agglomerates, e.g. by sintering, is recommended.



## Chapter 5

# Synthesis of Magnesium Hydride by Spark Discharge

**M**AGNESIUM HYDRIDE HAS THE POTENTIAL to be a cheap hydrogen storage material for automotive purposes. The high hydrogen content of 7.6 % H<sub>2</sub> is however offset by slow reaction kinetics, and nanostructuring of the material is generally considered to be necessary.

A novel approach is presented, where MgH<sub>2</sub> nanoparticles are synthesized from the elements using a spark discharge in a single-step, scalable, and green process. The formation of spark-generated MgH<sub>2</sub> was studied in mixtures of 0 to 100 % H<sub>2</sub>/Ar, using SMPS, XRD and TEM, as well as IR and TDS.

The particles are collected as hard agglomerates of 7 to 15 nm primary particles. H<sub>2</sub> affects the energy efficiency of the process, and a maximum production yield of  $1.3 \times 10^{-8} \text{ g J}^{-1}$  is obtained if 50 to 75 % H<sub>2</sub> is used. The particles consist of a mixture of nanocrystalline MgH<sub>2</sub>, Mg and MgO. Part of the 0.5 to 4.3 % m/m H<sub>2</sub> is present in an unidentified state; either as amorphous MgH<sub>x</sub>, or as a solid solution in Mg.

---

This chapter is closely related to chapter 3 in the dissertation of Anastasopol [101]. To appear as T.V. Pfeiffer, A. Anastasopol, J. Middelkoop, U. Lafont, E. Callini, A. Borgschulte, F. M. Mulder, S. W. H. Eijt, A Schmidt-Ott *Unusual Hydrogen Solubility in Nanoparticulate MgH<sub>2</sub> Synthesized by Reactive Spark Discharge*, manuscript in preparation.

## 5.1 Introduction

At this moment, no suitable production technique for *nanoparticulate*  $\text{MgH}_2$  exists. The popular alternative is mechanical alloying by means of e.g. a high energy ball mill, which produces nanocrystalline, but micrometer sized, particles. Catalysts and other additives can be conveniently added prior to mechanical alloying, but dispersion of these additives is poor. Nanocrystalline  $\text{MgH}_2$  can be made either by mechanical alloying of bulk  $\text{MgH}_2$  in an inert atmosphere, or through reactive mechanical alloying of Mg in  $\text{H}_2$  at elevated pressure [102]. Energy cost is typically not reported, and has to be estimated from experimental conditions. When ball milling Mg under  $\text{H}_2$  on a laboratory scale, energy costs are on the order of  $1 \times 10^8 \text{ J g}^{-1}$ . These methods can be transferred to (semi-)industrial scale ball mills [103], but the same limitations of lab scale milling apply. Other mechanical techniques that offer better scalability in terms of capital and energy costs, such as cold rolling, can be used to obtain a nanocrystalline structure if brittle  $\text{MgH}_2$  is used as a starting point [18]. The nanocrystalline hydride can also be synthesized directly from  $\text{MgCl}_2$  through reduction by LiH in a ball mill [104].

Liquid phase processes in general are characterized by good scalability and large waste streams. As the main interest in nanoparticles is due to their large surface area, surface contamination by surfactants, side products and solvent impurities are a concern. Liquid phase synthesis of  $\text{MgH}_2$  nanoparticles is typically achieved by reduction of an organometallic compound. The first work in this direction is by Bogdanovic [105], with the hydrogenation of a Mg–anthracene complex using transition metal homogeneous catalysts. Decomposition of Grignard reagents such as di-*n*-butylmagnesium under 50 bar hydrogen results in the formation of nanocrystalline  $\text{MgH}_2$ , although yields are significantly improved if the solvent is evaporated first [106]. With suitable capping ligands clusters of  $\text{Mg}_8\text{H}_{10}$  can be made, which release hydrogen upon heating to 473 K [107]. Nothing is known about possible reversible hydrogenation of the depleted clusters, and the extraordinarily large mass of the ligands limits their usefulness for hydrogen storage applications. The unavoidable presence of contaminants in the final product can also be used to advantage. Jeon, Moon, Ruminski, et al. synthesized Mg nanoparticles embedded in poly(methyl methacrylate) (PMMA), where the PMMA acts as a protective  $\text{O}_2$  barrier [108].

Nanoconfined  $\text{MgH}_2$  can be made by wet impregnation of a carbon scaffold with  $[\text{CH}_3(\text{CH}_2)_3]_2\text{Mg}$  or  $[\text{CH}_3(\text{CH}_2)_3]_2\text{Mg}$ , followed by thermal treatment under 5 MPa of  $\text{H}_2$  [109, 110]. Melt infiltration of nanoporous carbon

with liquid Mg avoids the use of organic solvents, but requires hydrogenation to form nanostructured  $\text{MgH}_2$  [111, 112]. In both cases, the product remains encased in the carbon scaffold, which might have implications on the final application.

Various methods can be grouped under the nomenclature physical vapour deposition/condensation. Oxide stabilized magnesium particles of 0.1 to 1  $\mu\text{m}$  can be produced by thermal evaporation of Mg and condensation on a cooled substrate in  $10^2$  Pa of inert gas [113]. When Mg is evaporated in an atmosphere of  $>20$  bar  $\text{H}_2$ ,  $\text{MgH}_2$  is formed in the form of wires with 0.1 to 1  $\mu\text{m}$  diameters [114]. Thin films of mostly  $\text{MgH}_2$  can be formed by RF-sputtering of Mg in 0.4 Pa of a 2:1 ratio of  $\text{H}_2$ :Ar [115]. Arc evaporation of Mg in a flow of 30%  $\text{H}_2$  in Ar at atmospheric pressure results in the formation of 300 nm particles of metallic Mg [116].

Spark discharge is a compromise between the cold and the hot discharges, and is characterized by rapidly quenched repetitive high energy pulses. Temperatures inside the spark reach  $6 \times 10^3$  to  $2 \times 10^4$  K, but each spark lasts only several  $\mu\text{s}$ . Each spark is accompanied by a rapid expansion of the plasma volume, which rapidly quenches the plasma in the working gas. The intermittent nature of the spark does however mean that only part of the gas turns to plasma, inherently leading to incomplete use of any gaseous feedstock.

This chapter describes a scalable method for producing nanoparticles of  $\text{MgH}_2$  with primary particle sizes  $<20$  nm, from the elements at ambient conditions.  $\text{H}_2/\text{Ar}$  mixtures in the range of 0 to 100%  $\text{H}_2$  were used as working gas in spark discharge. The  $\text{H}_2$  content influences production yield and product composition. The hydrogen storage properties of spark discharge  $\text{MgH}_2$  are evaluated, and compared to bulk and ball milled  $\text{MgH}_2$ .

## 5.2 Theory

While  $\text{MgH}_2$  is thermodynamically stable at ambient conditions, hydrogenation is prohibitively slow due to the poor  $\text{H}_2$  dissociation on the Mg surface. Increased temperatures lead to faster reaction rates, but shift the equilibrium away from the hydride according to the van 't Hoff equation

$$\ln \frac{p_{\text{eq}}}{p_0} = \frac{\Delta H}{RT} - \frac{\Delta S}{R} \quad (5.1)$$

If we want to hydrogenate Mg, with  $\Delta H = -74.4 \text{ J mol}^{-1} \text{ H}_2$  and  $\Delta S = -135 \text{ J K}^{-1} \text{ mol H}_2$  [117], at ambient pressure, a temperature below 550 K is

required.

Rather than splitting H<sub>2</sub> on the Mg surface, which suffers from slow kinetics, the H–H bond can also be broken in an electric discharge [56]. Monatomic species of H can have lifetimes up to 10<sup>-1</sup> s [118], sufficient long for hydrogenation. Atmospheric arcs have high degrees of dissociation, and a high specific power (~10<sup>10</sup> W m<sup>-3</sup>). Atmospheric pressure glow discharges operate under similar conditions [119]. These discharges are so called hot discharges:  $T_e \sim T_g \approx 1500$  K. An equilibrium shift due to insufficient cooling thus could explain why metallic Mg was formed instead of MgH<sub>2</sub> in the 30% H<sub>2</sub> arc of [116]. Dielectric barrier (DBD) and corona discharges are characterized by lower degrees of ionization and low gas temperatures. They are however not energetic enough to generate particles at industrially relevant scales [63]. Note that these cold discharges could however be useful to promote hydrogenation when refueling an existing H<sub>2</sub> storage system.

Consider the spark channel as a microreactor, where ablated metal atoms and plasma species are mixed and quenched. The volume of this microreactor depends on the energy of the spark. Capacitive spark discharges at atmospheric pressure of currents of 10<sup>2</sup> to 10<sup>4</sup> A are characterized by constant current densities on the order of 10<sup>3</sup> to 10<sup>4</sup> A cm<sup>-2</sup> [28, 120]. The spark channel in the spark generator needs to grow wide enough to accommodate the peak current in the spark generator, typically 200 to 300 A. This makes the volume of the spark discharge plasma ~10<sup>-8</sup> m<sup>3</sup> for a 1 mm spark gap.

The plasma volume consists of atoms, molecules, and ions, originating from both gas and electrodes, as well as free electrons. Prior to each discharge the gas is at ambient conditions, and the ideal gas law provides an upper limit to the concentration of species in the plasma that originate from the gas: 2.45 × 10<sup>25</sup> m<sup>-3</sup>. A typical spark ablates 10<sup>-11</sup> to 10<sup>-10</sup> mol [42], corresponding to concentrations of 10<sup>18</sup> to 10<sup>19</sup> m<sup>-3</sup>, or 1 ppm.<sup>1</sup> Fridman, Chirokov, and Gutsol [120] give an electron density of ≈10<sup>21</sup> m<sup>-3</sup> for ambient spark discharges. If we maintain charge neutrality by assuming 10<sup>21</sup> m<sup>-3</sup> positive ions to be present, ≥40 ppm of the gas is ionized. To obtain the desired 1 : 2 reaction stoichiometry of magnesium atoms and hydrogen ions, a minimum gas H<sub>2</sub> concentration of ≈5% is required. Since atomic and excited molecular hydrogen are also likely to give enhanced hydrogenation this value is an overestimation, and an excess of hydrogen is easily attained.

---

<sup>1</sup>This is equal to the total level of impurities in scientific grade (6N0, or 99.9999%) gases.

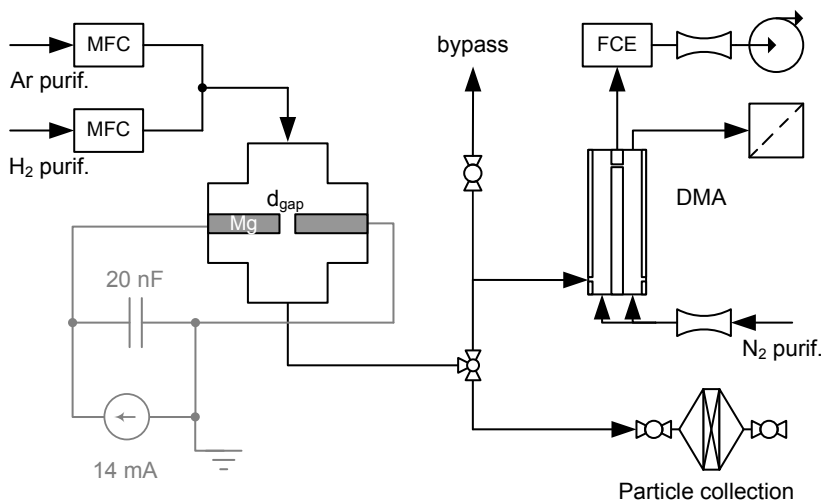


FIGURE 5.1 Experimental setup. DMA - *Differential mobility analyzer*, FCE - *Faraday cup electrometer*, MFC - *mass flow controller*.

## 5.3 Experimental

### 5.3.1 Synthesis

MgH<sub>2</sub> nanoparticles were synthesized by spark ablation of  $\square 6$  mm Mg rods in  $1.0 \text{ L min}^{-1}$  Ar and H<sub>2</sub> mixtures. The used setup (Figure 5.1) and the method of working contamination-free are based on those described in [10]. A second mass flow controller allows the full range of gas compositions to be used. All gases were of 5.0 purity, further purified using 0.5 L 5A molecular sieve and 0.5 L BTS catalyst to remove water and oxygen, respectively. In the case of hydrogen a second molecular sieve bed is needed to remove H<sub>2</sub>O formed by the reduction of BTS catalyst by H<sub>2</sub>. Before each collection run, the spark was run for 1 h to clean the electrode surface. Production rates were determined gravimetrically by collecting the particles on  $\square 47$  mm PVDF membranes (Millipore HVHP04700) in the form of a grey/black powder. All further sample handling was performed in a glovebox under Ar atmosphere with  $<0.1$  ppm O<sub>2</sub> and  $<0.1$  ppm H<sub>2</sub>O.

### 5.3.2 Characterization

The agglomerate size was determined on-line by means of mobility measurements. The Differential Mobility Analyzer of the Duisburg type was run in open loop to accommodate the changing gas composition of the polydisperse aerosol flow. The sheath flow of 10.0 L min<sup>-1</sup> nitrogen and the monodisperse aerosol flow of 1.0 L min<sup>-1</sup> were controlled via critical orifices. The flows in the DMA were controlled by fixing three flows leaving the hard to control excess flow free. With the used flows under laminar flow conditions, the error introduced by varying the composition of the inlet gas is estimated at <5% versus classical DMA theory.

X-ray diffraction (XRD) was performed on a PANanalytical X-Pert PRO diffractometer (Cu K<sub>α</sub>, 40 kV, 40 mA); its results were evaluated using the Powder Diffraction Files: Mg [35-0821], MgH<sub>2</sub> [74-0934], and MgO [45-0946]. Transmission electron microscopy (TEM) was performed on a FEI Tecnai TF20 electron microscope (200 kV), equipped with SAED and EELS capabilities. Infrared spectroscopy (FTIR) was performed using an Bruker ALPHA Platinum Attenuated Total Reflectance infrared spectrometer. A home built Thermal Desorption Spectroscopy setup, described in detail by Vons [30], was used to evaluate the hydrogen content of the as-produced particles. No activation steps were performed. To prevent evaporation of Mg a maximum temperature of 573 K was used.

## 5.4 Results

### 5.4.1 Production Rate and Yield

Production runs of 5 to 10 h yielded a grey-black powder at production rates of 0.1 to 1.1 mg h<sup>-1</sup>. Figure 5.2 shows the production yield in mass per energy, defined as production rate divided by the power input into the plasma, at constant charging current of 15 mA. By plotting the production yield rather than the production rate, we correct for the higher breakdown voltage of H<sub>2</sub>. With higher hydrogen concentrations the production rate and yield initially increase, but drop when the argon concentration approaches 0%. The increased *yield* is an important result, as energy efficiency is perhaps the most critical challenge in plasma ablation based nanoparticle generation methods.

We must emphasize that the presented production rates are of the collected product, not electrode mass loss as is sometimes reported. Because of the lengthy bake-outs required after opening the system, electrode mass loss

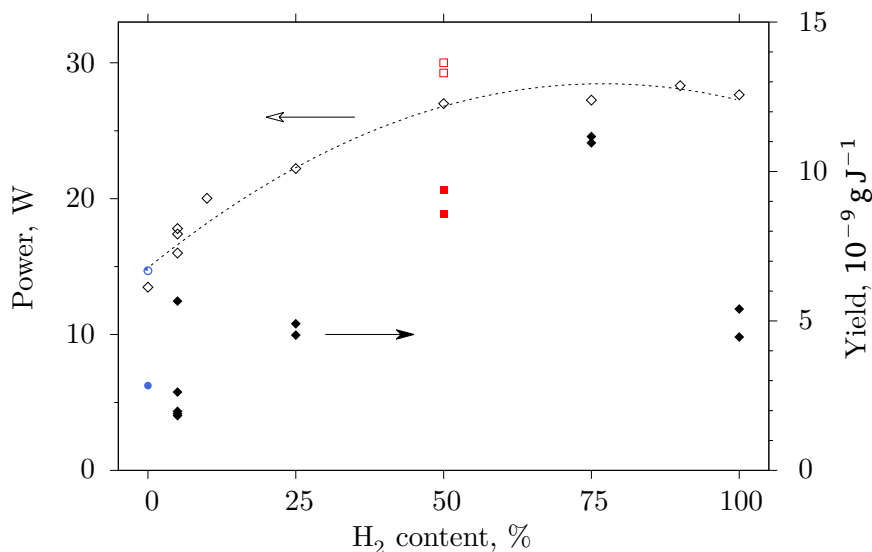


FIGURE 5.2 Power input (open symbols, left axis) and production yield (filled symbols, right axis) for increasing H<sub>2</sub> concentrations. *black diamonds*:  $d_{\text{gap}} = 1.5$  mm, *red squares*:  $d_{\text{gap}} = 1.75$  mm, *blue circles*:  $d_{\text{gap}} = 2.0$  mm, from [30]. The dashed line is a guide to the eye.

was determined at less frequent intervals, typically 3 to 5 production runs. Average electrode mass loss rates indicate particle losses around 60 to 80%, which can largely be attributed to diffusional losses of small particles.

The use of production rates results in an underestimation of ablation rates. More importantly, it removes measurement artifacts due to start up and shut down of the system, and directly represents the characterized product. Ablation rates can be especially skewed when large particles are formed but not collected. Because of the increasing contribution of surface energy, mass production rates in plasma based ablation methods drop with decreasing particle size. In spark discharge, part of the product consists of large spherical particles formed by liquid ejection [54]. These large particles constitute 5 to 10% of the mass of the product<sup>2</sup>. As such, while being system dependent, collection rates represent the *steady state* rate of nanoparticle production

<sup>2</sup>In unpublished experiments, we deposited the splash droplets in a medium/low pressure impactor. Because the aerodynamic diameter of a large spherical particle is much larger than an open agglomerate, the pressure can be set such that only the spherical particles are deposited. From image analysis on electron micrographs, we found a lower limit of 5% m/m of splash droplets in the collected product.

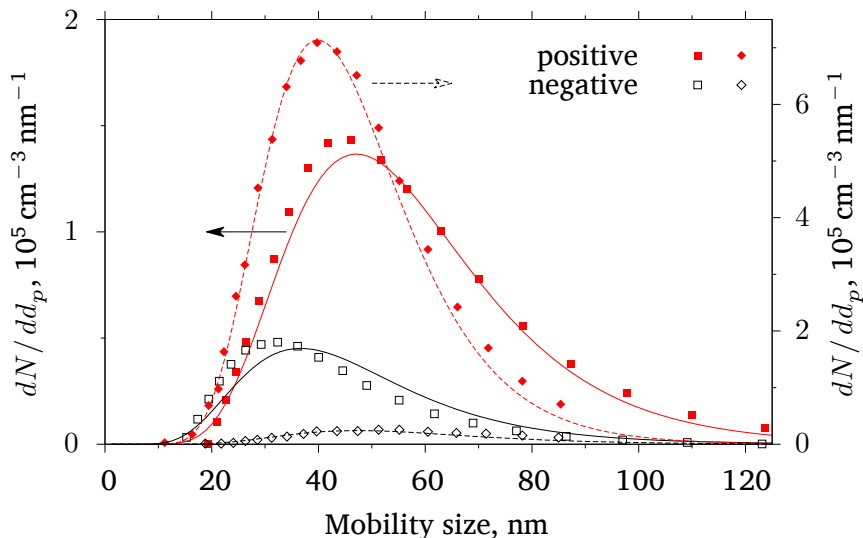


FIGURE 5.3 Self-charging in 100% Ar. Lines represent lognormal fits to the data. *squares/solid lines*: 1.5 mm gap, 15 mA, 10 W. *diamonds/dashed lines*: 2.0 mm gap, 9 mA, 5 W adapted from [30].

more accurately than electrode mass loss measurements.

#### 5.4.2 Mobility measurements

Figure 5.3 shows the mobility size distribution of Mg nanoparticles formed in 100% Ar in comparison to prior results by Vons [30]. The DMA measures the aerodynamic size of the agglomerates, and gives little information on the primary particle size; mobilities are calculated with the assumption of unit charge. Neglecting multiply charged particles is very reasonable for bipolar charging of  $<50$  nm particles [89], while 9% of 100 nm particles is doubly charged. An excess of positively charged particles is measured, but the new measurements show a decreased total number of charges, and a 6 times lower charge ratio  $n^+/n^-$ . Additionally, the mode of the distributions has shifted in opposite directions for the two polarities.

Size distributions for different  $\text{H}_2$  concentrations are shown in Figure 5.4. Adding  $\text{H}_2$  greatly reduces the excess of positive charges, and results in smaller modes. When  $\text{H}_2$  is present, the mode of the distributions shifts slightly to larger sizes with increasing  $\text{H}_2$  concentration. At  $\geq 50\%$   $\text{H}_2$ , the positive

and negative distributions are near equal.

### 5.4.3 Morphology and Structure

#### TEM

Figure 5.5 shows a micrograph of powder produced under 5 % H<sub>2</sub> atmosphere. The particles are nanostructured agglomerates, with morphologies typical of spark discharge. The particles are surrounded by an MgO shell, which leads to sample charging in the electron beam. Moreover, the electron beam induces desorption of hydrogen. Because of the drift caused by charging and hydrogen evolution we could not acquire high resolution images for these samples. The CMD of 127 primary particles is 14 nm with a geometric standard deviation of 1.5. A fine structure with protrusions of several nm in size can be observed on the surface of the agglomerates (Figure 5.5a, insert).

Electron diffraction patterns show diffuse rings, confirming the nanocrystalline nature of the sample (Figure 5.6). Figure 5.6b shows the averaged radial profile, referenced to the clear [002] reflection of MgO according to Vons [30]. This transformation results in a 6% larger reciprocal lattice spacings measured using the scale bar provided by the TEM software (Figure 5.6a); this correction is justified by the excellent fit with the principal reflections of both MgO and Mg. The three characteristic reflections of Mg comprise speckled rings, as compared to the smooth MgO lines, indicating that Mg is present in larger domains than MgO. No evidence for the presence of MgH<sub>2</sub> was found. The TEM results are consistent with earlier measurements [30].

#### XRD

X-ray diffraction patterns for 5 to 100 % H<sub>2</sub> are given in Figure 5.7. The presented results are normalized without background subtraction. Mg is the dominant species at all concentrations, and broad features indicate the presence of nanostructured MgO. In the diffractograms for 50 % and 75 %, broad reflections occur at 27.815° 2θ, 35.642° 2θ, 39.799° 2θ and 54.542° 2θ, which were assigned to MgH<sub>2</sub> [PDF 74-0934]. For 50 % H<sub>2</sub> small shoulders were observed at 25.530° 2θ and 37.9° 2θ, which correspond well with the 26.605° 2θ and 37.75° 2θ reflections of γ-MgH<sub>2</sub> [PDF 35-1184]. The main [111] reflection at 31.478° 2θ is however missing, and the gamma phase of MgH<sub>2</sub> cannot be assigned. The diffraction patterns for 5 %, 25 % and 100 % are of poor quality due to low sample quantities, and merely suggest the presence of Mg

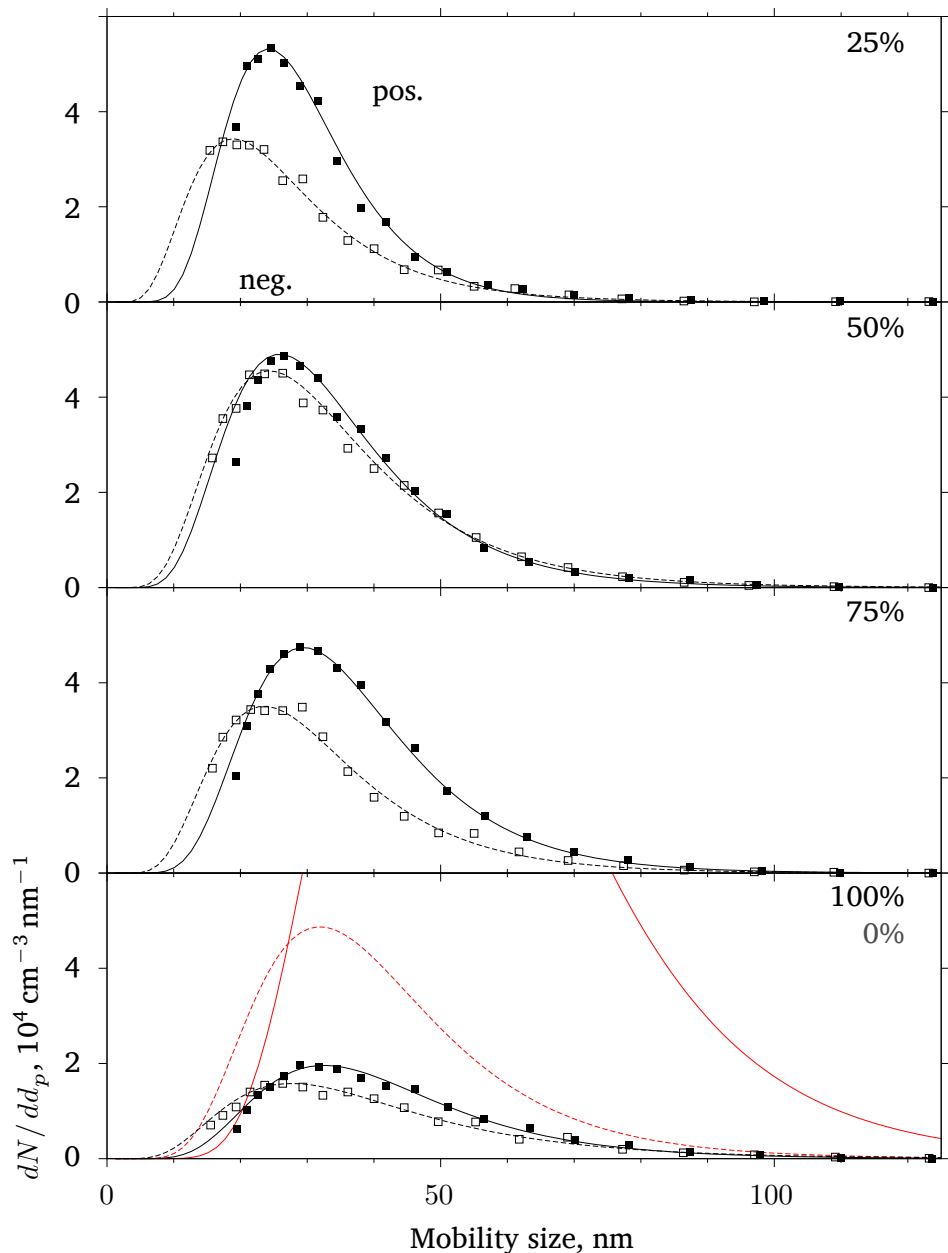


FIGURE 5.4 Mobility size distributions for H<sub>2</sub> concentrations of 25%, 50%, 75% and 100%, 15 mA, 22.5 W. The lognormal curves are guides to the eye. The lognormal fit for 0% H<sub>2</sub> from Figure 5.3 (squares) is provided for reference.

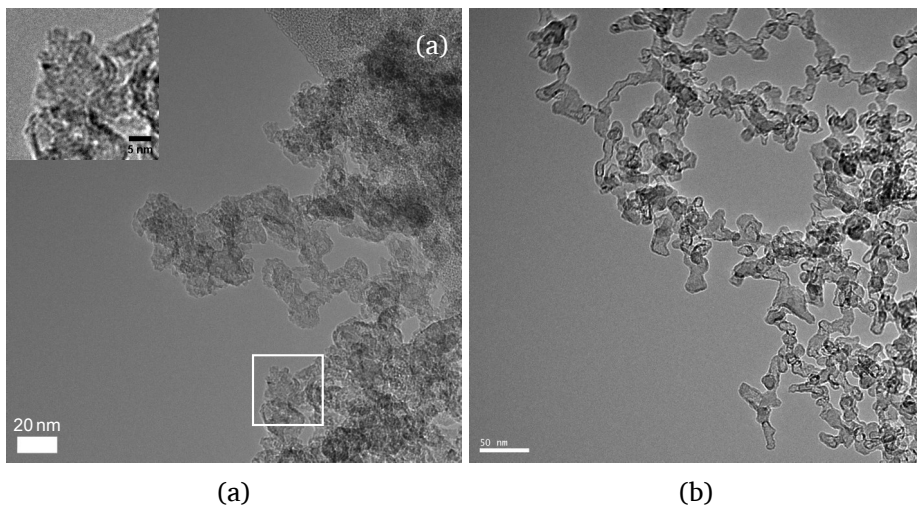


FIGURE 5.5 TEM micrographs. (a) 5%  $\text{H}_2/\text{Ar}$ , 20 nm scale bar; insert: detail of highlighted area, 5 nm scale bar. (b) Mg produced in pure Ar, 50 nm scale bar, reproduced from [30].

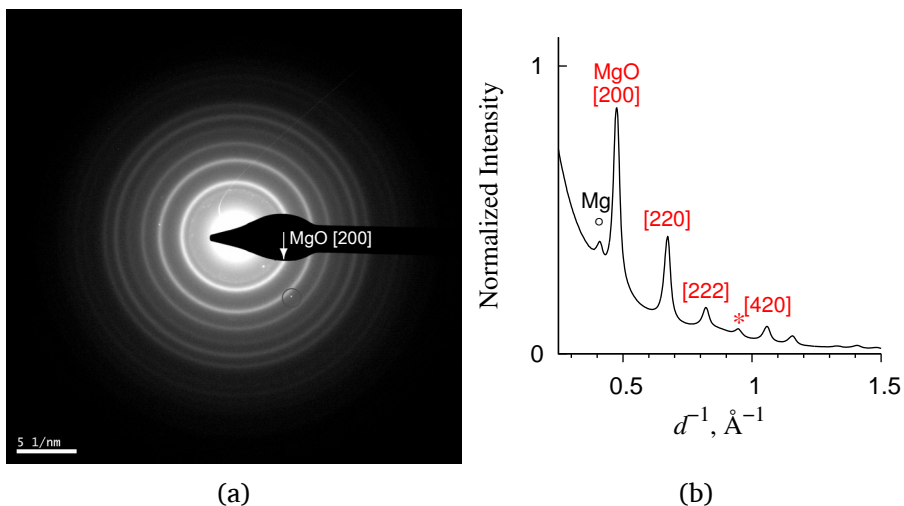


FIGURE 5.6 Electron diffraction pattern (a) and corresponding radial profile (b) for 5%  $\text{H}_2$  (see text). The reflection denoted by  $\circ$  corresponds to unresolved Mg [100], [002], and [101] planes. The reflection denoted by \* is attributed to the second harmonic of the MgO [200] plane. The (red) circled dot corresponds to the second harmonic of Mg [100].

and MgO. Crystallite sizes as determined using the Scherrer formula, corrected for instrument broadening and using a structure factor of 0.9, are reported in Table 5.1.

TABLE 5.1 Scherrer crystallite sizes

Angle °2θ	Species	50 % H <sub>2</sub>		75 % H <sub>2</sub>	
		FWHM °2θ	<i>d<sub>c</sub></i> nm	FWHM °2θ	<i>d<sub>c</sub></i> nm
27.82	MgH <sub>2</sub>	1.15	7.4	1.69	4.9
32.10	Mg	0.44	19	0.36	23
34.31	Mg	0.45	18	0.38	22
36.53	Mg	0.48	18	0.34	25
39.80	MgH <sub>2</sub>	0.77	11	—	—
54.54	MgH <sub>2</sub>	1.06	8.4	0.95	9.4

Rietveld analysis (Figure 5.8) is complicated by the overlapping of the sample holder reflections at 28.15° 2θ and 44.30° 2θ with the broad reflections of MgH<sub>2</sub> at 27.814° 2θ and MgO at 42.83° 2θ, respectively. γ-MgH<sub>2</sub> had to be excluded from the analysis to prevent the regression from diverging. Indicative mass fractions calculated from the refinement are given in Table 5.2.

TABLE 5.2 Mass fractions in % m/m as determined by Rietveld analysis.

	50 % H <sub>2</sub>	75 % H <sub>2</sub>
<i>f</i> <sub>Mg</sub>	(25.0 ± 0.1) %	(12.1 ± 0.1) %
<i>f</i> <sub>MgH<sub>2</sub></sub>	(38.2 ± 0.3) %	(20.7 ± 0.2) %
<i>f</i> <sub>MgO</sub>	(36.9 ± 0.8) %	(67.2 ± 0.1) %
<i>R</i> <sub>wp</sub>	3.4 %	3.4 %
χ <sup>2</sup>	12.4	3.9

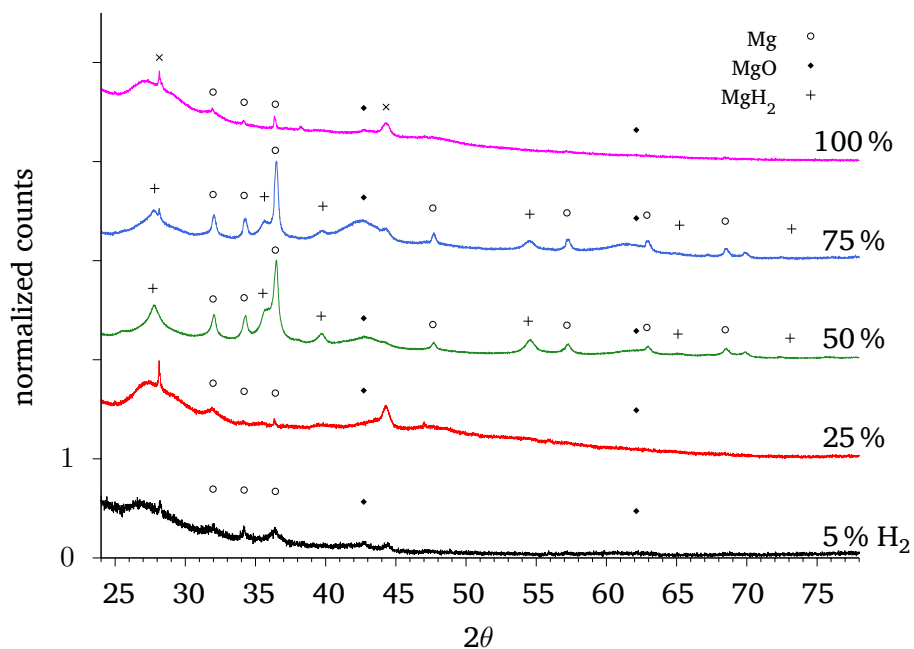


FIGURE 5.7 XRD for increasing H<sub>2</sub> concentrations. Spectra are normalized without background subtraction. × denotes reflections originating from the air-tight sample holder.

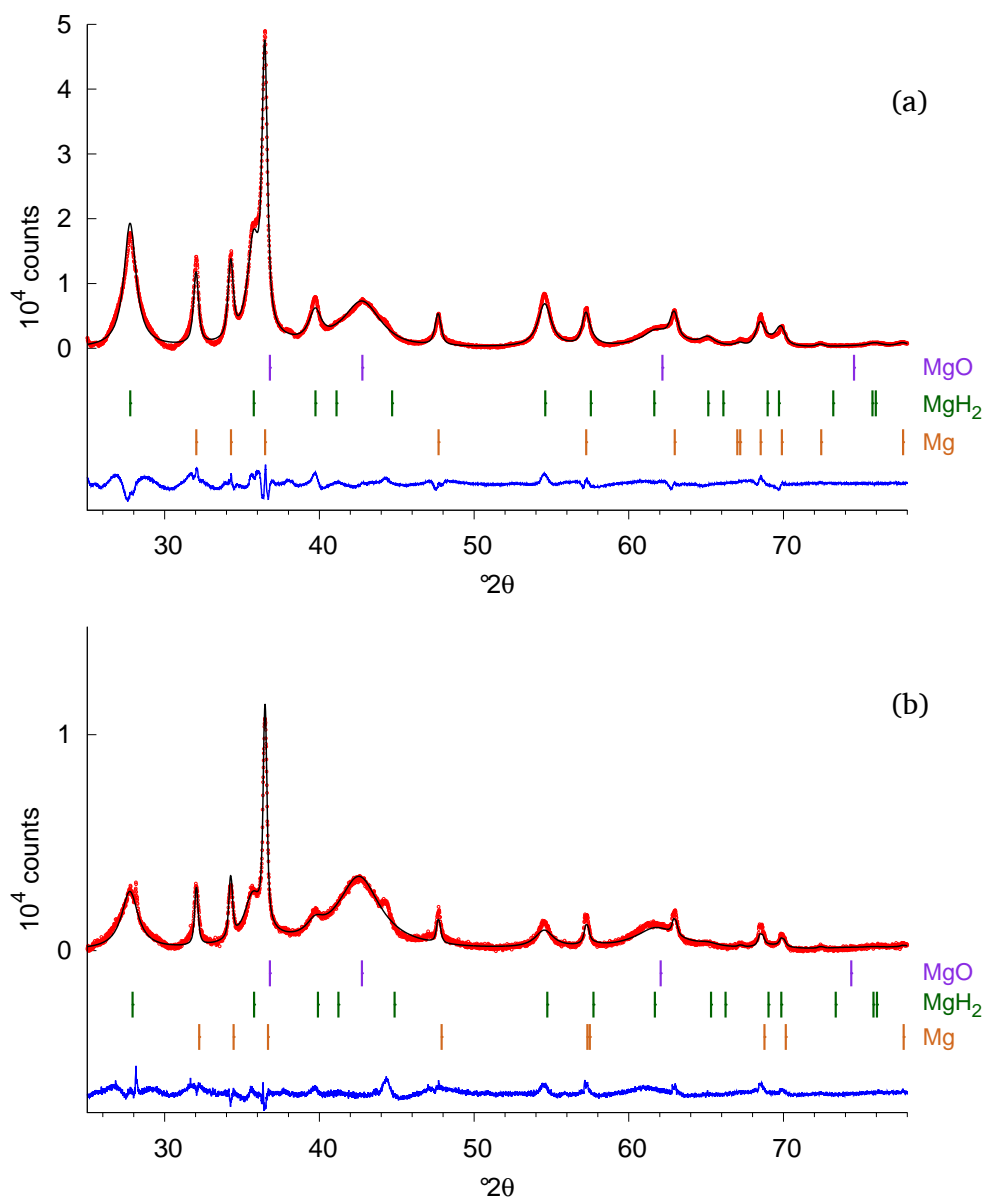


FIGURE 5.8 Rietveld refinement of  $\text{MgH}_2$  synthesized in (a) 50%  $\text{H}_2$ , and (b) 75%  $\text{H}_2$ .

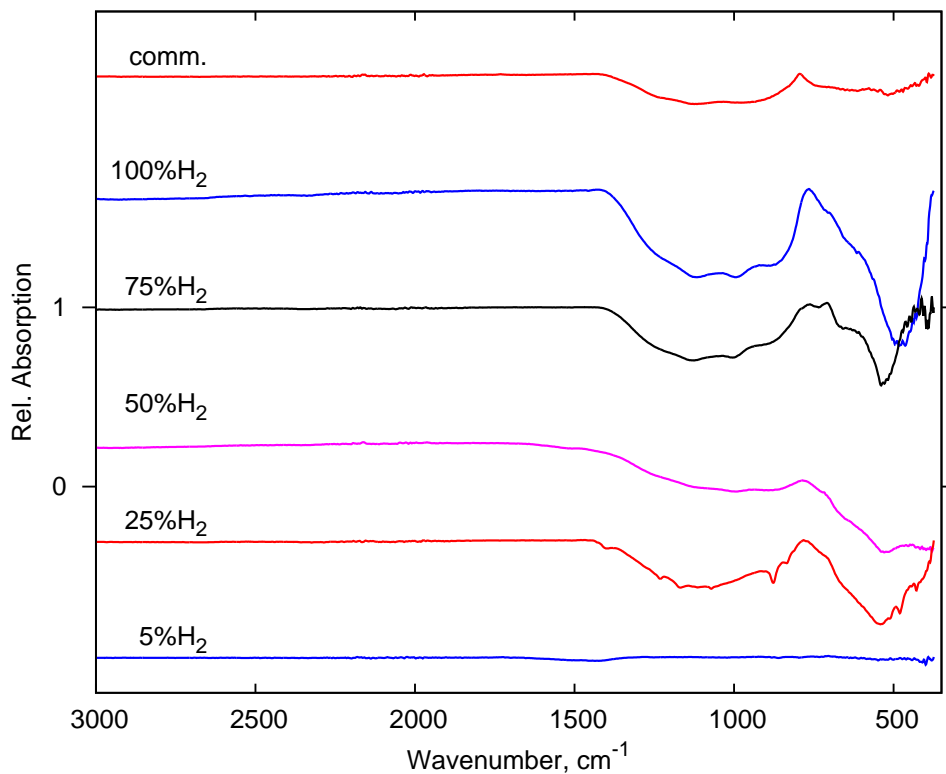


FIGURE 5.9 Infrared transmission spectrum of MgH<sub>2</sub> synthesized in 5 to 100% H<sub>2</sub>. MgH<sub>2</sub> prepared by ball mill is included for reference.

#### FTIR

The transmission spectra of MgH<sub>2</sub> produced at various H<sub>2</sub> concentrations are given in Figure 5.9. The spectra of spark generated samples are in good agreement with the ball-milled reference sample. The broad band from 1600 to 900 cm<sup>-1</sup> centered around 1160 cm<sup>-1</sup> is typical for MgH<sub>2</sub> [121].

## 5.4.4 Hydrogen content

The hydrogen content of the samples was determined by integrating the signal from the mass spectrometer from the Thermal Desorption Spectroscopy setup. This is done under the assumption that complete dehydrogenation occurs, hence the values reported in Table 5.3 represent a lower limit for the hydrogen content. Assuming that all hydrogen in the sample exists in the form of  $\text{MgH}_2$ , the as-produced samples comprise 6.8 to 56 % m/m of  $\text{MgH}_2$ . No correlation was found between hydrogen content in the gas and in the final product.

For a detailed investigation into the hydrogenation properties of spark-generated  $\text{MgH}_2$  the reader is referred to the dissertation of Anastasopol [101]. In short, the material comprises a large fraction of  $\alpha\text{-MgH}_2$ , i.e. a solid solution of H in hexagonal Mg, which shows enhanced hydrogenation kinetics without the need for a catalyst. The spark-generated materials are unique, in that the  $\alpha\text{-MgH}_2$  persists over multiple cycles, along with the enhanced hydrogenation rates.

TABLE 5.3 Initial hydrogen content determined by TDS. See text.

$\text{H}_2$ in gas	% m/m $\text{H}_2$	est. % m/m $\text{MgH}_2$
5 %	0.52 %	6.8 %
50 %	4.31 %	56 %
75 %	2.72 %	36 %

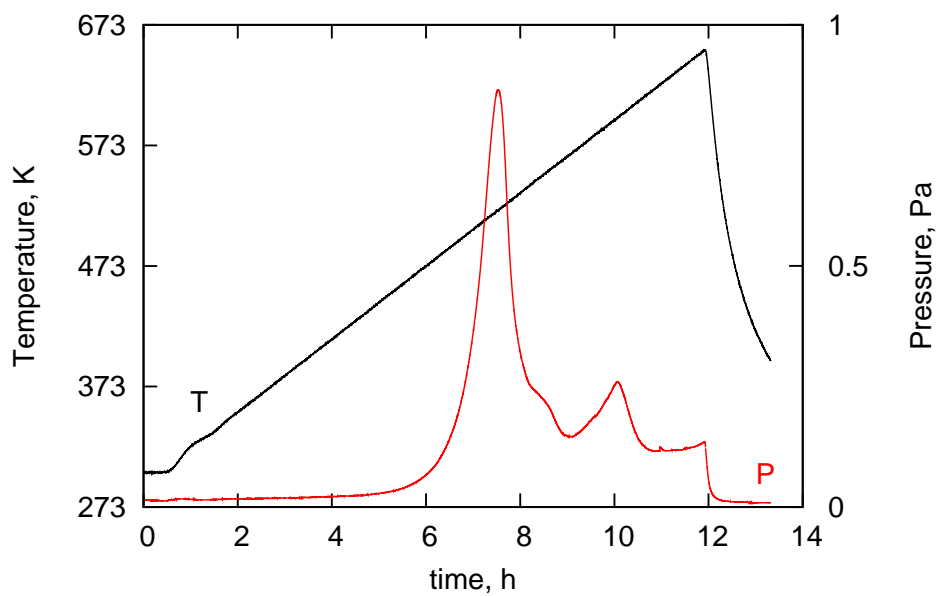


FIGURE 5.10 Thermal desorption spectrum recorded at  $0.5\text{Kmin}^{-1}$  of  $\text{MgH}_2$  synthesized in 50%  $\text{H}_2$ .

## 5.5 Discussion

### 5.5.1 Particle charging

From the mobility measurements in Figure 5.3 it is apparent that self-charging in a high purity Ar spark does not follow the bipolar equilibrium distribution typically observed in aerosol charging, which is characterized by approximately equal positive and negative charges. In equilibrium chargers, ions are continuously generated in the charging volume. In contrast, the charge carriers in spark discharge are formed coincidentally with particle formation, and can be depleted before equilibrium has been reached. Ion-forming electronegative species are essentially absent in high purity noble gases, and the dominant negative charge carriers are free electrons. The mobility of free electrons is much larger than that of the gas ions, resulting in excess negative charges in absence of electric fields [122]. When an electric field is applied the free electrons rapidly disappear, resulting in an excess positive space charge and a positively charged aerosol. In the simple spark discharge circuit this electric field is applied as the cathode potential rises during capacitor charging.

The two sets of mobility measurements recorded in pure Ar (Figure 5.3) were performed in essentially the same experimental setup, but show a drastic difference in charge ratio  $n^+/n^-$ . Vons [30] used a dedicated Ar bottle, and measured  $n^+/n^- = 20$ . In this work the gas composition was controlled by changing the mix ratio between two gas bottles, and  $n^+/n^- = 3.5$  was obtained. After each change in gas composition the system was flushed with the spark on for >15 min, i.e. 45 residence times. This reduces the levels of residual H<sub>2</sub> in the system to negligible levels, and residual H<sub>2</sub> cannot account for the observed differences. The likely cause of the decreased charge ratio is partial hydrogenation of the Mg electrodes due to atomic hydrogen formed in the spark<sup>3</sup>. A small surface layer of MgH<sub>2</sub> on the electrode surface increases the persistence of hydrogen in the system: Only a small quantity of hydrogen is liberated with each spark, enhancing the H<sub>2</sub> concentration in the vapour cloud until the surface layer has been completely etched away.

The presence of H<sub>2</sub> in noble gases influences the charge distribution because the hydrogen atom is weakly electronegative with an electron affinity

---

<sup>3</sup>In a separate experiment, a second spark generator with two Nb electrodes was placed 12 cm downstream of the first spark [123]. See also chapter 6. We observed catastrophic failure of the Nb electrodes due to hydrogen embrittlement when sparking Mg in 5% H<sub>2</sub>, even though the Nb electrodes were at room temperature, grounded and inactive.

of  $\sim 0.754$  eV, and readily forms a negative ion [56]. As such, one can expect the charge distribution in  $\text{H}_2/\text{Ar}$  mixtures to more closely resemble the bipolar charge distribution (Figure 5.4). The addition of  $\text{H}_2$  results in a significant drop in total charge, likely because the increased  $\text{H}_2$  concentration enhances ion recombination. There is little difference between the various hydrogen concentrations, apart from a slight shift of the mode, which grows for both polarities by  $\sim 40\%$  from 25% to 100%  $\text{H}_2$ . The number of charges at 25 to 100%  $\text{H}_2$  qualitatively follows the production yield (Figure 5.2). Because the number concentration of neutral particles is unknown, it is not possible to draw strong conclusions about the charge fraction in the aerosol. Further work is needed to determine whether the apparent paradox of a growing mode with a constant charge-to-mass ratio is caused by a change in charge fraction, multiple charging, or particle morphology.

The modal sizes of the positive and negative particles in Figure 5.3 do not coincide for either data set. In the old dedicated  $\text{Mg} + \text{Ar}$  setup the mode of positive particles ( $\mu_+$ ) is smaller than that of the negative particles ( $\mu_-$ ), while the opposite result,  $\mu_+ > \mu_-$ , is observed in the gas mixing setup. Vons demonstrates that the low  $\mu_+$  is the result of a large fraction of multiply charged positive particles. However, multiply charged negative particles as an explanation for  $\mu_+ > \mu_-$  is unlikely, as positive charges are still in excess. Instead, it appears that the large particles are preferentially positively charged. This effect can be qualitatively understood if we consider the spark as a system where coagulation occurs simultaneously with diffusion charging by a finite supply of ions. As the vapour cloud generated by the spark starts to condense, collisions occur between atoms, particles and gas ions. Larger particles pick up charges faster than smaller particles [66], similar to bimodal coagulation (see chapter 7). At some point the negative ions are effectively depleted, while the remaining positive ions preferentially charge the larger size fraction of the growing aerosol.

### 5.5.2 Structural Characterization

The synthesized product is not pure  $\text{MgH}_2$ . At  $\sim 30$  to 70% m/m,  $\text{MgO}$  is present in comparable concentrations to when no  $\text{H}_2$  is present. The important contributions to oxidation in the system come from trace impurities in the carrier gas, and from outgassing and permeation of the materials (steel, glass, ceramic, PTFE, etc.) of the experimental system [30]. Additionally, even though the powders are handled under a protected atmosphere, the  $\sim 1$  m<sup>3</sup> glove box with  $< 0.1$  ppm  $\text{O}_2$  represents a problematic amount of oxygen for

small sample volumes. Working with larger product volumes and incorporating a closed loop gas recycle (chapter 2) tackle the largest sources of oxygen. Preferably, some form of encapsulation or passivation of the product to avoid further oxidation is included in further process design.

More hydrogen desorbed than detected in the form of crystalline  $\text{MgH}_2$ . Considering that  $\text{MgO}$  is inactive, and assuming there is no amorphous fraction, the  $\text{Mg-MgH}_2$  mixture would have an overall compositions of  $\text{MgH}_{1.77}$  and  $\text{MgH}_{2.2}$  for 50% and 75%  $\text{H}_2$ , respectively. This is very high when compared to the relative abundance of  $\text{Mg}$  and  $\text{MgH}_2$  obtained from XRD (Table 5.2). This excess hydrogen is either present as a solid solution within hexagonal  $\text{Mg}$ , or in the form of an amorphous hydride.

Since no catalysts were included, it is highly unlikely from a kinetics point of view that such a high  $\text{H}_2$ -loading was achieved by room temperature exposure of  $\text{Mg}$  nanoparticles on the collection filter. The  $\text{MgH}_2$  must have formed during the spark. A mechanism for the formation of  $\text{MgH}_2$  is provided in a following section.

From TEM results of Vons, Anastasopol, Legerstee, et al. [10], we know that  $\text{Mg}$  primary particles formed by spark discharge in pure Ar sinter to form chain-like agglomerates surrounded by a thin oxide shell. Two types of domain were identified: elongated structures 7 to 15 nm wide and up to 50 nm long, and in smaller numbers hexagonal domains of 20 to 200 nm. From the TEM results in this work, we can conclude that the presence of hydrogen during spark formation inhibits sintering. In the as-produced samples the hexagonal domains are mostly absent, and the surface of the agglomerates is not smooth, having protrusions 3 to 4 nm in diameter (Figure 5.5a, insert). An explanation lies in the nature of the  $\text{Mg-H}$  bond, which is considered to be somewhere between ionic and covalent. Compared to a metallic system, which is characterized by delocalized covalent bonds, the atoms in  $\text{MgH}_2$  have less freedom to move, resulting in increased melting and sintering temperatures versus  $\text{Mg}$  metal.

### 5.5.3 Production Rate and Yield

An increase in production rate has been observed for other metals in other plasma based systems for hydrogen concentrations up to 50%, among others by Tanaka and Watanabe [124] and Förster, Wolfrum, and Peukert [125]. In prior work, no compensation was done for any increased power input. Four causes are often proposed in literature to explain the increased production rate:

1. Bubbles formed through recombination of hydrogen atoms in molten metals,
2. High thermal conductivity of hydrogen,
3. Formation of intermediate compounds such as hydrides,
4. Activity modification by hydrogen in the molten metals.

In our case, the first three effects undoubtedly contribute to the increased production rate, but none can account for the observed decrease in production rate for pure H<sub>2</sub>.

Watanabe, Itoh, and Ishii [126] demonstrated that high heat conductivity of hydrogen and the recombination of H<sub>2</sub> within the metal play a minor role in the formation of nanoparticles by arc discharge. They instead attribute the enhanced evaporation rate to the formation of intermediate products, i.e. hydrides, or an “activity modification by hydrogen in molten metals”. However, they found no evidence of hydride formation in a H<sub>2</sub>/Ar arc, even for hydrogen active materials such as Ti and V. It is likely that in the current work a surface hydride formed on the electrodes, which affected the physical properties thereof. A lowered thermal conductivity and a reduction in Mg–Mg bond strength due to interstitial hydrogen would both contribute to an increased vaporization efficiency.

A similar trend with H<sub>2</sub> concentrations as in Figure 5.2 was observed for the vaporization rate with a constant current DC arc for Fe in He-H<sub>2</sub> mixtures by Noma, Ueshima, Fukui, et al. [127]; for Fe in Ar-H<sub>2</sub> insufficient data is provided to identify if a maximum exists [128]. The production rate in 0% and 50% H<sub>2</sub> in Ar increased by two orders of magnitude, but resulted in BET particle size growth from 9 nm to 33 nm. Simultaneously, the yield, calculated from published data, increases from  $9 \times 10^{-11}$  to  $7 \times 10^{-9}$  g J<sup>-1</sup> with increasing H<sub>2</sub> concentrations [128]. Molecular hydrodynamics simulations indicated the higher specific heat of H<sub>2</sub> results in a thermal pinch, focusing the plasma energy and raising the plasma temperature in H<sub>2</sub>/He mixtures. No explanation for the drop in production rate was provided.

The particle formation mechanism in spark discharge is still poorly understood, but two processes can provide for sufficient energy transfer from the plasma into the electrodes to explain the observed evaporation rates (Z. Geretovsky, personal communication, 23 Jan 2014). Joule heating rapidly raises the plasma temperature to 10<sup>4</sup> K, and the electrode temperature to the boiling point of the metal, leading to evaporation of the electrode material. The evaporation rate should be proportional to the energy input, and does not explain the drop in production yield. The second process is sputtering,

where ions in the plasma are accelerated by the oscillating electric field, and impinge on the electrode surface. The sputtering rate,  $\gamma_{\text{sput}}$ , depends on the kinetic energy of the impinging ion,  $E_i$ , and the weighted relative atomic numbers of the impinging and target atoms,  $\bar{Z}_t$ , according to [56]:

$$\gamma_{\text{sput}} \sim \frac{0.06}{E_t} \sqrt{\bar{Z}_t} \left( \sqrt{E_i} \sqrt{E_{\text{thr}}} \right), \text{ with} \quad (5.2)$$

$$\bar{Z}_t = \frac{2Z_t}{(Z_i/Z_t)^{2/3} + (Z_i/Z_t)^{2/3}},$$

where subscripts  $i$  and  $t$  denote the incident and target atom/ion, respectively,  $E_t$  is the surface binding energy, and  $E_{\text{thr}}$  is a threshold energy. Although Equation 5.3 was developed and tested for low pressure systems, it does provide an explanation for the observed dip in production yield.  $_{18}\text{Ar}^+$  and  $_{2}\text{He}^+$  have a  $\bar{Z}_t$  versus  $_{12}\text{Mg}$  of 11.6 and 6.7, respectively, while for  $_{1}\text{H}^+$   $\bar{Z}_t = 4.4$ . At very high H<sub>2</sub> concentrations sputtering becomes less effective due to the decrease in  $\bar{Z}_t$ , which under constant power conditions translates to a reduced production rate. While more research is required to quantify the relative contributions of Joule heating and sputtering to ablation rates, the current results show that sputtering cannot be neglected in spark discharge production of nanoparticles.

#### 5.5.4 Hydride formation

Metal hydrides can form in H<sub>2</sub>/Ar arcs, if the metal hydride is stable enough. Using Equation 5.1 we can define an equilibrium temperature,  $T_{\text{eq}}$ , at which the hydrogen partial pressure of the hydride matches that of the working gas. Table 5.4 shows  $\Delta H$ ,  $\Delta S$  and  $T_{\text{eq}}$  for metals that can form hydrides, and have been used in H<sub>2</sub>/Ar arcs. Under conditions<sup>4</sup> where metallic Mg is produced, the hydrides of TiH<sub>1.9</sub>, CeH<sub>2</sub>, and Sm<sub>3</sub>H<sub>7</sub> are produced [129, 130]. TiH<sub>2</sub>, CeH<sub>2</sub>, and Sm<sub>3</sub>H<sub>7</sub> are more stable than MgH<sub>2</sub>, while CeH<sub>3</sub> is less stable. The equilibrium temperatures of these hydrides obtained from the van 't Hoff relation (Equation 5.1), are presented in Table 5.4. The hydrides formed in the arc have equilibrium temperatures >640 K, while the hydrides with equilibrium temperatures <530 K did not form. The maximum temperature of a DC arc in 50 % H<sub>2</sub> in Ar is calculated to be about  $2.5 \times 10^4$  K [128], although the temperature at the evaporation zone is typically lower. Quench

<sup>4</sup>TiH<sub>1.9</sub> and Mg form under 50 % H<sub>2</sub>, CeH<sub>2</sub>, Mg, and Sm<sub>3</sub>H<sub>7</sub> under 20 % H<sub>2</sub>.

rates of  $10^4$  to  $10^5$  K s $^{-1}$  are quoted for this system [129]. The estimated time required to cool the cloud to below the equilibrium temperature of MgH $_2$  is then  $10^{-1}$  to  $10^{-2}$  s.

TABLE 5.4  $\Delta H$  and  $\Delta S$  and equilibrium temperatures of selected arc-generated metal hydrides.  $\Delta H$  and  $\Delta S$  from the provided references, given per mol H $_2$

Metal hydride	$\Delta H$ J mol $^{-1}$	$\Delta S$ J K $^{-1}$ mol $^{-1}$	Ref.	[H $_2$ ]	$T_{\text{eq.}}$ K	Hydride formed? <sup>a</sup>
CeH $_3$	-51	-114	[131]	20%	400	no
MgH $_2$	-74.4	-135	[117]	50%	501	no
MgH $_2$				20%	529	no
Sm $_3$ H $_7$	-78	-108	[132]	20%	641	yes
TiH $_2$	-142	-174	[133]	20%	790	yes
CeH $_2$	-156	-78	[131]	20%	1710	yes

<sup>a</sup> [129, 130]

In contrast, MgH $_2$  was obtained by spark discharge in 50% H $_2$  (Table 5.3). The peak temperature of  $\sim 2 \times 10^4$  K [31] lasts for a few  $\mu$ s, after which the plasma is quenched by turbulently mixing with with the carrier gas. Due to this discontinuous nature, the quench rates in spark discharge are estimated at  $-10^7$  K s $^{-1}$  [42], and the equilibrium temperature of MgH $_2$  is reached in  $10^{-4}$  to  $10^{-3}$  s. Considering the fact that excited species of atomic H, with energies of 10 to 11 eV, can have lifetimes of  $10^{-4}$  to  $10^{-1}$  s [118], we propose the following formation mechanism for hydrides in plasma evaporation systems.

Particles form by condensation as the metal vapour cloud formed by the plasma, comprising various species of metal, hydrogen, and possibly an inert gas, is supercooled. Metal hydrides can form as long as the partial pressure of H $_2$  exceeds the equilibrium pressure of the hydride (Equation 5.1). This often occurs at a relatively low temperature, which results in slowed reaction kinetics according to the Arrhenius relation. However, in cases where hydrogen splitting is the rate-limiting step, such as Mg, the presence of atomic H will result in an increased hydrogenation rate. This is exemplified by the two systems presented here: with arcs the equilibrium temperature is reached on the same time scale as the life time of the longest-lived species of atomic H, and only negligible formation of MgH $_2$  can be expected. In spark discharge the equilibrium temperature is reached much faster, resulting in longer reac-

tion times with larger concentrations of atomic H, allowing the formation of  $\text{MgH}_2$ .

## 5.6 Conclusion

$\text{MgH}_2$  nanoparticles were synthesized at atmospheric conditions by spark discharge in a 0 to 100 %  $\text{H}_2$  atmosphere. The product consists of  $\text{MgH}_2$  (partly crystalline, Scherrer size 9 nm, partly amorphous), Mg (20 nm), and MgO (<4 nm). Hydrogen desorption experiments show that the product contains at least 0.5 to 4.3 % m/m of  $\text{H}_2$ . The hydride forms early during the coagulation process, reducing the effect of sintering and yielding a reduced primary particle size. The presence of  $\text{H}_2$ , even in trace quantities, affects the self-charging process for spark discharge in purified Ar. When  $\text{H}_2$  is added the charge distribution shifts from positive excess towards neutral.

A maximum production yield is obtained at  $\text{H}_2$  concentrations of 50 to 75 %. The maximum is consistent with a non-negligible contribution of sputtering to the evaporation rate, in addition to the generally accepted Joule heating mechanism. The energy efficiency of the spark discharge process is a crucial commercial parameter, and further research on tuning the production yield with the gas composition, specifically to optimize sputtering efficiency, is recommended.

The formation of  $\text{MgH}_2$  is explained by the rapid cooling rate in spark discharge, and the longevity of certain species of excited atomic  $\text{H}_2$ . The atomic species enhance the hydrogenation rate, and  $\text{MgH}_2$  forms at temperatures where its formation is thermodynamically favourable, but otherwise kinetically limited. This observation implies that atomic hydrogen could be used to increase the low-temperature charging rates of existing metal hydride systems, and we strongly recommend future research into the use of plasma based refueling systems.

## Chapter 6

# Nanoscale Dispersion of Niobium and its Oxides in Nanostructured Metallic Magnesium

**N**ANOSTRUCTURED, HYDROGEN STORAGE CAPABLE niobium-catalyzed magnesium powders were produced using two spark generators in series. Niobium-rich clusters of 2 to 10 nm size are evenly dispersed within the nanoparticulate magnesium matrix down to a scale of 50 nm. Oxides of niobium were formed through the surface ablation of the native oxide layer on a niobium electrode. While the  $\text{NbO}_x$  nanoparticles are formed in an aerosol of nano-structured, pyrophoric magnesium, oxygen transfer to magnesium is not observed. Reduction of  $\text{NbO}_x$  occurs only after hydrogen cycling at elevated temperatures.

## 6.1 Introduction

The slow reaction kinetics of MgH<sub>2</sub> have inspired significant effort into finding suitable catalyst materials [134–139]. These studies however give little attention to the state in which the catalyst is dispersed, beyond the bulk composition and catalyst particle size. This is surprising, as the catalyst dispersion has a profound impact upon the performance of these composite materials: large catalyst particles, or even strongly clustered nanosized catalyst particles, will not be effectively utilized. Diffusion can play an important role when a shell of magnesium hydride forms during hydrogen sorption. Once this shell reaches a thickness of  $\approx 20$  nm, it becomes a blocking barrier due to the slow diffusion of hydrogen through MgH<sub>2</sub> [140]. This implies that only those Mg domains that lie within  $\approx 20$  nm of a catalyst particle will benefit from said catalyst. In-situ TEM investigations confirm that the hydriding reaction is localized around the catalyst particles [141].

Spark discharge particle generation is a direct method of synthesizing gas-borne high-purity metallic nanoparticles, and has been used to make hydrogen storage materials [10]. Mixing in low quantities of Pd significantly increased the ab- and desorption rates, although the Pd could only be found in as a Mg<sub>6</sub>Pd alloy in XRD. The particle generation process is similar to laser ablation, but the ablation energy is delivered by a high voltage discharge rather than a laser. The required electronic components are simple and cheap, providing better prospects with regards to scaling up production rates.

This chapter presents an approach to producing metal oxide nanoparticles in oxygen sensitive environments, using the spark generator. This study also intends to provide controllable means of distributing nanosized catalyst particles down to a nanometer scale within a nanoparticulate matrix. We use aerosol based processes in order to allow efficient mixing without the need for solvents. While we use a spark generator to provide our primary aerosol flow, we see no reason why this method of depositing catalyst particles could not be directly applicable to nanoparticulate aerosols produced by other means, such as electrospray, flame spray pyrolysis, and the like.

## 6.2 Theory

For a given aerosol, condensation and agglomeration result to a decrease in particle number and an increase in particle size, eventually resulting in a (self-preserving) lognormal distribution of particle sizes [66]. Particle growth

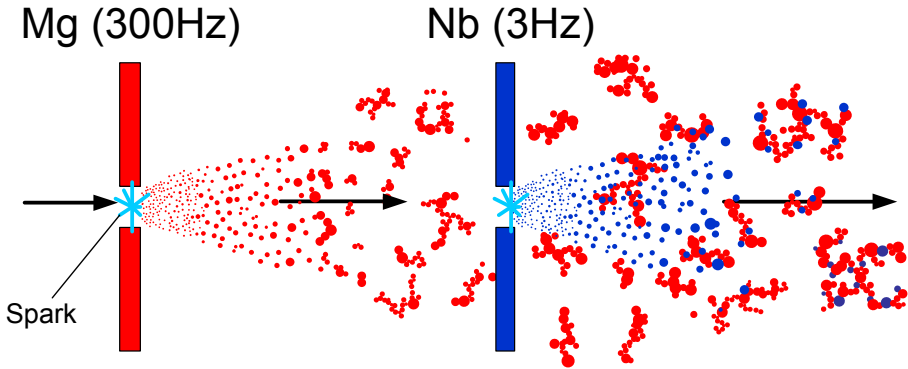


FIGURE 6.1 Schematic process of catalyst addition. A second, low-power spark produces Nb catalyst particles that are mixed with agglomerates of Mg synthesized in a first, high-power spark.

is defined by the number of particles and the time available for growth. Whether coalescence occurs or structured agglomerates are formed depends on the temperature history and the particle size. If a second aerosol is added at any stage during the first agglomeration process, the newly added particles will participate in the agglomeration process. This bimodal coagulation is described in chapter 7 in context of coating spherical particles.

As we're primarily interested in the scale down to which catalyst particles can be mixed homogeneously within the Mg matrix, it suffices to know the size the agglomerates have grown to by the time they reach the second spark. The particle number concentration  $N$  in an aerosol decreases according to

$$\frac{dN}{dt} = -KN^2, \quad (6.1)$$

where the coagulation kernel  $K$  depends on the collision diameter of the particles, and their diffusion coefficients. For particles 1 to 100 nm in diameter  $K$  has a value of  $3 \times 10^{-16}$  to  $1 \times 10^{-15} \text{ m}^3 \text{ s}^{-1}$ . For a given metal, we can know the mass ablated by the spark using data on ablation efficiencies from literature [42]. From the total ablated mass  $m_0$ , the number of particles, and assuming bulk density, the mean particle volume is

$$\bar{V}_p = \frac{m_0}{N(t)} * \rho, \quad (6.2)$$

from which, in the case of spherical particles, the particle size is easily obtained. As  $K$  is mostly independent of particle size, the particle volume of

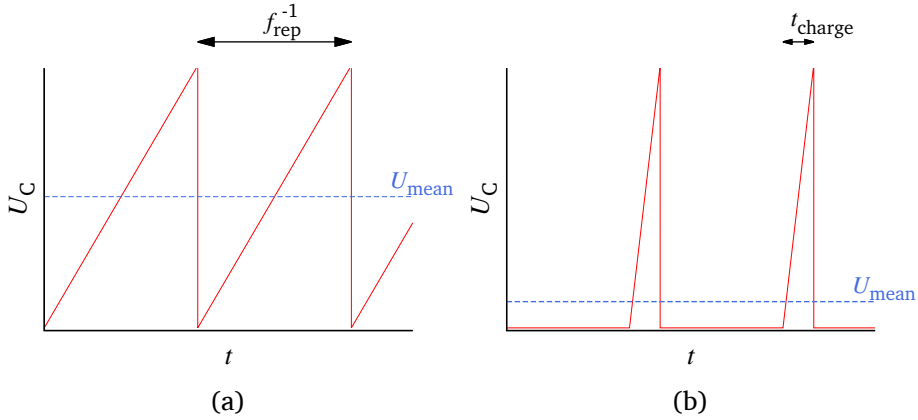


FIGURE 6.2 Capacitor voltage vs. time and mean capacitor voltage for (a) classic and (b) pulsed operation modes.

Equation 6.2 is a function only of coagulation time and the ablated mass, which can be modified experimentally by changing the carrier gas flow rate or the distance between sparks, or by changing the power input into the spark, respectively.

Because the residence time of the particles in the spark chamber is six orders of magnitude larger than the 10  $\mu\text{s}$  spark event, a mean electric field in the chamber results in electrostatic losses in the time between sparks. In the classic system, a constant current  $I$  repetitively charges a high voltage capacitor  $C$  the breakdown voltage of the gas (Figure 6.2a). The discharge frequency  $f_{\text{rep}}$  is then determined through the discharge voltage  $U_d$  by

$$f = I/U_d C, \quad (6.3)$$

resulting in an oscillating high voltage field with a mean voltage of  $U_d/2$  within the spark chamber.

To reduce electrostatic losses of primary aerosol in the second spark we can operate said spark in a ‘pulsed’ mode by periodically stopping the current from the power supply. The resulting waveform is depicted in Figure 6.2b. In an ideal system, the mean voltage in the gap is reduced by a factor  $t_{\text{charge}} \times f_{\text{rep}}$ , while the same discharge voltage and spark energy are achieved. In practice, fluctuations in discharge voltage lead to an instability in the system, and the mean field is higher.

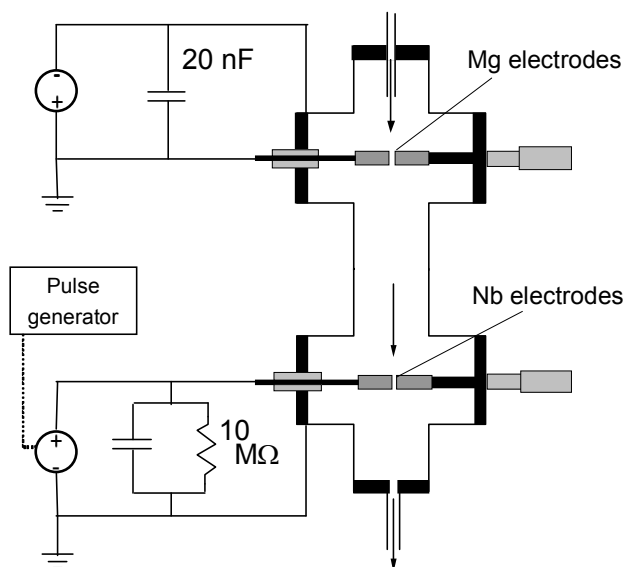


FIGURE 6.3 Schematic of the double spark generator.

### 6.3 Experimental

The setup comprises two spark generators in series, as described by Vons, Anastasopol, Legerstee, et al. for the production of a Mg-Pd composite [10]. The key novelty with regards to the spark generators commonly in use today [22], lies in the capacitor charging system used in the second spark. A 20 nF capacitor is charged with a current pulse of 1 to 10 ms, followed by a dead time where no electric field presides in the spark chamber. Pulses were generated using a Technix CCR high voltage current source controlled by a function generator, and a 10 MΩ resistor parallel to the capacitor was used to dissipate any charge remaining in the capacitor after each discharge. This operating method allowed us to both directly control the discharge frequency and reduce the mean electric field in the second spark chamber by 70 to 99% for frequencies of 10 to 300 Hz.

Niobium and magnesium (99.9%, MaTeck GmbH) rods of 6.35 mm OD were used as electrodes. The Nb electrodes had been exposed to air for several months, resulting in the formation of a native oxide layer. The gap distance in the Mg spark was varied between 1.0 mm and 2.0 mm as noted in Table 6.1. The Nb electrode pair was placed 12 cm downstream of the Mg electrodes.

TABLE 6.1 Operating conditions for Mg and Nb sparks, and Nb content measured by ICP and EDX. The conditions under #6 are the same as in Anastasopol, Pfeiffer, Schmidt-Ott, et al. [123].  $d_{\text{gap}}$  was 1.8 mm for sample #10, and 1.0 mm in all other cases.

ID #	Mg		Nb		Nb content g Nb/g Mg	
	$d_{\text{gap}}$ mm	$I_C$ mA	$f_{\text{rep}}$ Hz	$I_C$ mA	ICP	EDX <sup>a</sup>
1	2.0	12.5	10	1.9	0.25	-
2	2.0	12.5	20	1.5	<0.03	-
3	2.0	12.6	40	0.9	0.17	-
4	2.0	12.4	40	1.3	0.08	0.14
5	1.8	12.4	10	0.3	0.13	-
6	1.8	12.4	40	1.2	0.05	0.12
7	1.8	12	100	3.0	1.46	-
8	1.0	8.8	30	1.2	0.24	-
9	1.0	8.1	60	1.9	0.71	4
10	1.8	10.8	100	4.6	-	1.1

<sup>a</sup> From the ratio of integrated peak areas ( $\propto \text{mol mol}^{-1}$ ), average of measurements with a  $\sim 1000$  nm spot size, except for sample #6, for which a 50 nm spot size was used.

The gap distance of the Nb spark was kept constant at 1.0 mm unless otherwise noted. 1 L min<sup>-1</sup> of 99.999% argon, further purified to minimize oxide formation as previously described [10], was used as the carrier gas.

An SMPS system was used to measure mobility distributions of self-charged agglomerates, i.e. without the use of a neutralizer. Particles were collected on a membrane filter (Millipore HVHP0047) at typical rates of 0.1 to 0.3 mg h<sup>-1</sup>, yielding samples of 1 to 2 mg for further analyses. X-ray diffraction patterns were recorded on a PANalytic X-pert Pro diffractometer at the Cu(K <sub>$\alpha$ ,1</sub>) spectral line,  $\lambda = 0.15415$  nm.

The local distribution of catalyst particles was investigated using a transmission electron microscope fitted with a EDX probe (FEI monochromated Tecnai 200STEM-FEG). Calibration of the EDX was inadequate for quantitative analysis, therefore the distribution of niobium in the samples was evaluated by the ratio of the integrated areas of the peaks of Mg K <sub>$\alpha$</sub>  and Nb L <sub>$\alpha$</sub> , which each are proportional to the molar contents of said element. While we could not determine the absolute concentrations in the samples, we can com-

pare the relative abundance of niobium at different locations within a given sample. This provides an indication of how homogeneously Nb is distributed throughout the sample. To determine Mg and Nb contents the samples were dissolved overnight in piranha solution (1:4 H<sub>2</sub>O<sub>2</sub>:H<sub>2</sub>SO<sub>4</sub>), and analyzed with ICP-OES (PerkinElmer Optima 5300DV). Except for ICP-OES, all actions were performed under inert atmosphere (O<sub>2</sub>, H<sub>2</sub>O <0.1 ppm).

## 6.4 Results and discussion

### 6.4.1 Electrostatic losses

For a Mg spark under the high purity conditions as applied here, positively charged particles comprise >50 % of the total aerosol [30]. In this work, negatively charged particles were  $\sim 20 \times$  less abundant than positive particles, in agreement with prior work [30]. Because of this large charged fraction, the total production rate of the spark discharge method can be significantly affected by electrostatic losses. The impact of the pulsed charging mode on electrostatic losses was monitored using a DMA. Figure 6.4 shows mobility size distributions from the double spark for pure and mixed aerosols of Mg (200 Hz, 2 mm gap) and Nb (300 Hz, 2 mm gap). At these conditions the production rate and size distributions of Mg and Nb were approximately equal. A slight increase in number concentration was found for a single spark running in the pulsed mode as compared to the continuous mode, where the mean electric field in the second spark was reduced from 1.0 kV for the continuous mode to 0.2 kV for the pulsed mode (Figure 6.2a).

For two spark generators in series operated in the non-pulsed mode (Figure 6.4b, filled circles), the overall yield was equal to or lower than that of the single spark generators (Nb: Figure 6.4a, filled circles, Mg: Figure 6.4b, open diamonds)). When the second spark was pulsed (half-filled circles in Figure 6.4b) the number concentration doubled, i.e. negligible losses of positively charged Mg agglomerates occurred. The count mean diameter of the mixed aerosol shifted slightly from 42 nm to 49 nm when the Nb spark was pulsed. This growth has to be attributed to coagulation between charged and neutral (agglomerates of) particles. Spark generated agglomerates tend to have open structures, with fractal dimensions,  $D_f$ , as low as 1.8 [39]. Mg agglomerates in this size range have a  $D_f$  of 2.1 to 2.4 [30], and we can estimate that the shift in particle size corresponds to a growth of 30 to 40 % by volume. This likely is the result of large, neutral Mg agglomerates that

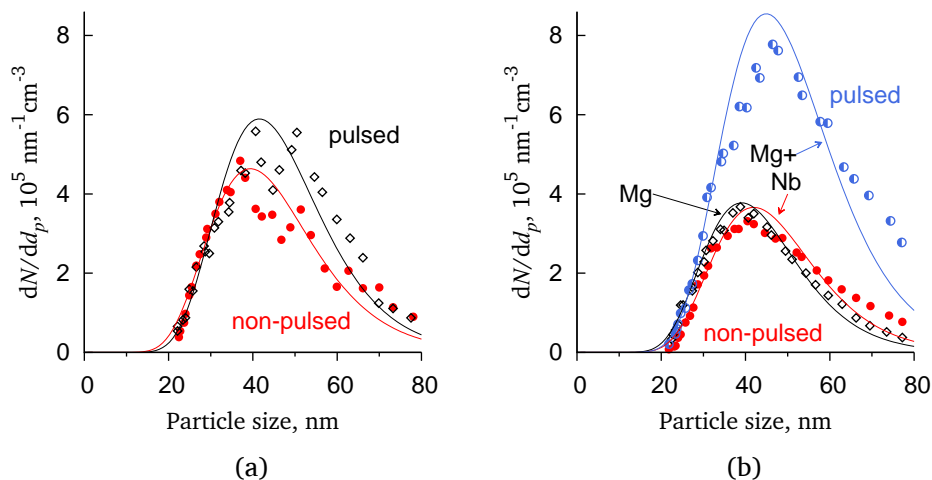


FIGURE 6.4 Effect of pulsing the Nb spark on the size distributions of positively self-charged agglomerates. (a) Nb only, 2 mm gap, 300 Hz  $f_{\text{rep}}$ ; filled circles  $t_{\text{charge}} = f_{\text{rep}}^{-1}$ , open diamonds  $t_{\text{charge}} = 0.3 \mu\text{s}$ . (b) open diamonds Mg only, 2 mm gap, 200 Hz  $f_{\text{rep}}$ ; filled circles Mg + Nb,  $t_{\text{charge}} = f_{\text{rep}}^{-1}$ , half circles Mg + Nb,  $t_{\text{charge}} = 0.3 \mu\text{s}$ . Lines represent lognormal fits

obtain a charge through collision with charged Nb particles, rather than the growth of a new mode. The mobility measurements paint only a general picture of the agglomeration process in the dual spark. No correlation was found between mobility measurements and the Nb content of the nanocomposites discussed below.

#### 6.4.2 Bulk composition

ICP measurements show that Nb:Mg ratios of 0.03 to 1.46 g g<sup>-1</sup> were obtained (Table 6.1). Figure 6.5 compares the measured Nb:Mg ratio (points) with the values expected from the relative ablation efficiencies of Nb and Mg (dotted line). The discrepancy between predicted and measured values is probably related in part to electrostatic losses, i.e. samples with high Nb:Mg ratios have high losses of Mg. Samples #7 and #9 produced at 100 Hz and 60 Hz, respectively, fall in this category. In general the Nb:Mg ratio seems randomly distributed, and likely was significantly influenced by the poorly defined flow conditions within the reactor chamber, which lead a broad residence time distribution due to recirculation.

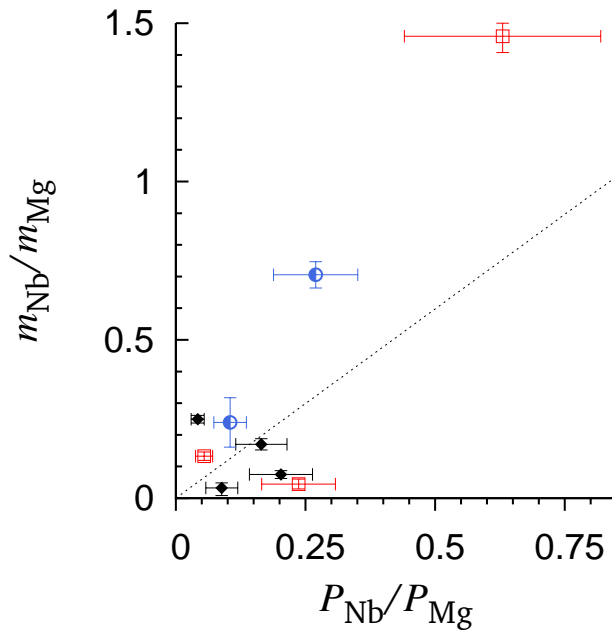


FIGURE 6.5 Mass ratio of Nb to Mg vs. relative power input. Nb gap: 1.0 mm (blue circles), 1.8 mm (red squares), and 2.0 mm (black diamonds). The dotted line indicates the expected ratio based on ablation efficiencies in literature [42].

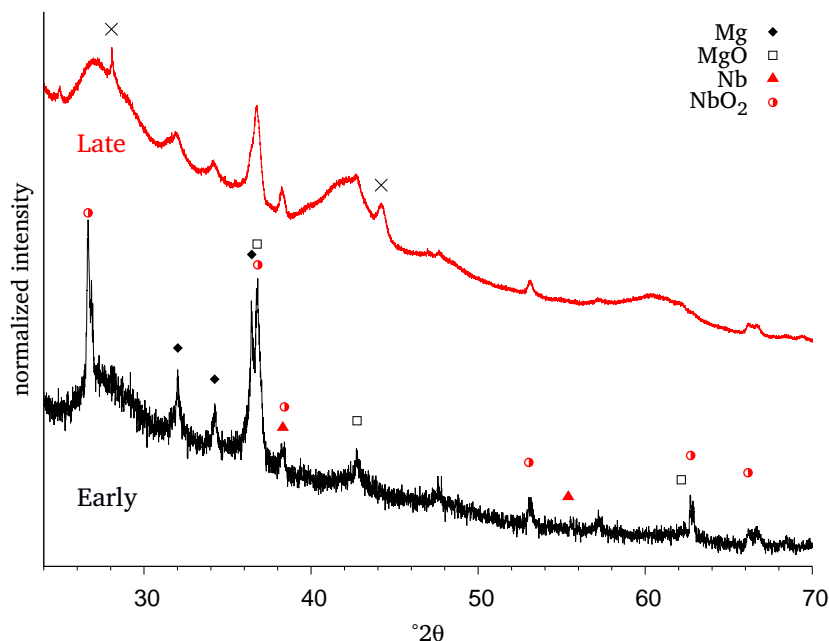


FIGURE 6.6 Normalized ( $y$ -axis  $\propto$  intensity) X-ray diffraction pattern of Mg + Nb composite powder from early (black) and late (red) production runs.

The powder diffractogram of several pooled samples synthesized under conditions of #5 in Table 6.1 is shown in Figure 6.6 (black line). Reflections belonging to Mg, MgO, Nb, NbO<sub>2</sub> and Nb<sub>2</sub>O<sub>5</sub> were identified through Rietveld analysis (Table 6.2). Mg is easily identified from its three characteristic peaks at 32.009° 2 $\theta$ , 34.226° 2 $\theta$  and 36.436° 2 $\theta$ . Metallic Nb Particle sizes were estimated using Scherrer's equation, giving 23 to 133 nm domain sizes for Mg and 45 nm for Nb. The broad bump at 42.953° 2 $\theta$  is characteristic of the MgO-shell of spark-generated Mg [30]. X-ray diffractograms of other samples show similar trends, but were of insufficient quality to allow Rietveld analysis.

From the results of Rietveld refinement of the XRD patterns, we learn that crystalline Mg and MgO are present in nearly equal amounts in the as-produced samples, in strong agreement with prior results [10]. It is important to stress the limitations in quantitative interpretation of XRD-patterns for nanoparticulate powders. Many metals produced in the spark generator contain a significant amorphous fraction, which can lead to their underestimation in quantitative analysis. Niobium oxides exist in a plethora of crystal structures,

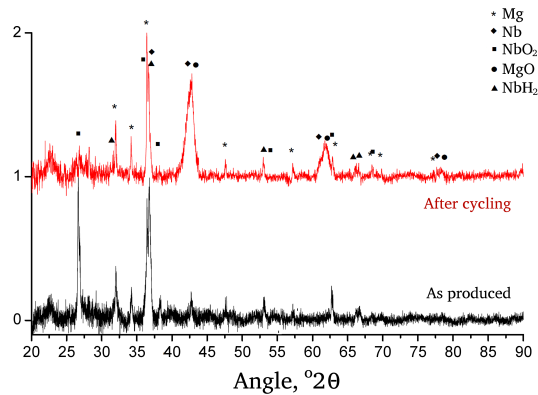


FIGURE 6.7 Normalized ( $y$ -axis  $\propto$  intensity), background-corrected X-ray diffraction pattern of Mg + Nb composite powder before (black) and after (red) hydrogen ab- and desorption.

TABLE 6.2 Results of Rietveld analysis before and after hydrogen sorption experiments for particles made from partially oxidized Nb rods, compared to the phase identification in particles made from clean Nb. Composition of the nanocomposite expressed in %-wt. of the crystalline fraction.

Phase		Native oxide		Clean Nb
		before	after	
Mg		15 %	10.8%	yes
MgO		15 %	70.2%	yes
Nb	FM3M	33.2%	0.5%	some
Nb	IM3M	0.7%	1.1%	some
NbO <sub>2</sub>		29.3%	2 %	no
Nb <sub>2</sub> O <sub>5</sub>		5.8%	8.1%	trace
MgH <sub>2</sub>	P42MNM	-	5.1%	no
NbH <sub>0.89</sub>	PNN2	-	2.2%	no

many with low symmetry that quickly disappear in the background noise. On the other hand, MgO will only assume a simple cubic structure, in domains as small as 0.5 nm (TEM), and must be considered highly crystalline.

The oxides of niobium are far more abundant than those of the more electropositive magnesium, whereas one would expect that the niobium would be reduced by the magnesium [142, 143]. Indeed, in the samples that were used for hydrogen storage experiments [123], the niobium oxides disappeared in lieu of MgO after cycling at 300 °C.

Under our pure conditions,  $>1 \times 10^4$  Mg atoms were ablated per oxygen molecule present in the carrier gas. The magnesium spark is placed up-stream of the niobium spark, and any gas phase oxygen is likely scavenged before it reaches the second electrode pair. Selective oxidation of niobium can therefore only occur if a second oxygen source, such as the ablated electrode surface, is present. During discharge, the shockwave caused by the forming plasma channel pushes away the magnesium aerosol, leaving a niobium vapour. Any oxygen evaporated from the surface is then present in high local concentrations of Nb, resulting in the preferred oxidation of Nb over Mg.

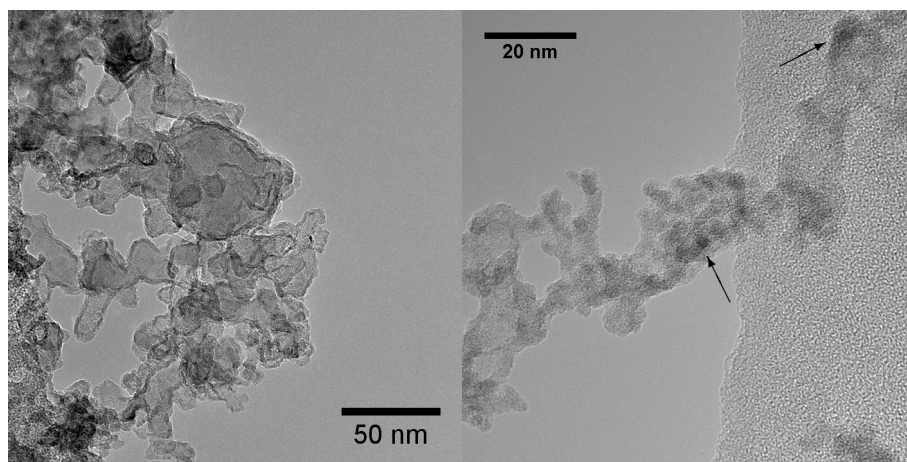
Many metals form native oxide layers when exposed to air, and in the case of niobium, a stable  $\approx 6$  nm Nb<sub>2</sub>O<sub>5</sub> layer develops over the course of several days [144]. The volume ablated by a single spark can be estimated from the mass loss per spark event ( $\approx 1 \times 10^8$  g spark<sup>-1</sup> [42]) and the diameter of the hot spot of the spark ( $\approx 50$  μm [145]). The ablated volume can be approximated as a 1 μm-thick disc 50 μm in diameter, i.e. much thicker than the native oxide layer. For such thin layers, one expects to find a mixture of different oxides and the metal, but only for a brief time, as the native oxide layer is rapidly cleared by the sparks. However, during the growth of the Nb<sub>2</sub>O<sub>5</sub> layer, defects can form to the large volume expansion associated with the pentoxide growth; oxygen penetrates deeper into the surface along these defects and NbO<sub>x</sub>, with  $x \approx 1$  up to 100 nm and  $x \approx 0.2$  up to 1 to 10 μm are formed [146]. Unpolished rods with a 'rough' surface texture were used here, allowing the oxide to penetrate deeper into the rod. One can expect that the volume occupied by the μm-thick oxide layer was sufficiently thick to result in a high oxygen content in the vapour plume.

On the other hand, the surface of the magnesium electrodes had been thoroughly refreshed through >100 h of prior use in a low-oxygen environment, and can be considered essentially oxygen free. As the electrodes wear down through continued use in the spark generator, the oxygen layer on the Nb electrode depletes. This is seen in later samples, where the niobium oxides has mostly disappeared from the product (Figure 6.7, red line). Two things

can be concluded. Firstly, electrodes should undergo surface treatment to remove surface oxides, if metal nanoparticles are desired. Secondly, (partially) oxidized electrodes, formed by deliberately exposure to air, anodization, or compaction of powders [47], could be used to produce of metal oxide nanoparticles *in the presence of less noble metals*.

#### 6.4.3 Local composition - catalyst distribution

TEM shows typical structures observed for magnesium nanoparticles produced by spark discharge [10]. Domains of coalesced primary particles are encased in a  $\approx 2$  nm thick oxide shell. The size of these primary domains can be approximated with a lognormal distribution with a count median Feret's diameter of 13 to 20 nm ( $\sigma_g = 1.5$ ), in agreement with the Scherrer crystallite sizes obtained from XRD. Dark particles of 3 nm ( $\sigma_g = 1.45$ ) in size were identified as niobium compounds using EDX. Small quantities of niobium were also be found in some of the lighter areas in some samples, although no specific domains were observed.



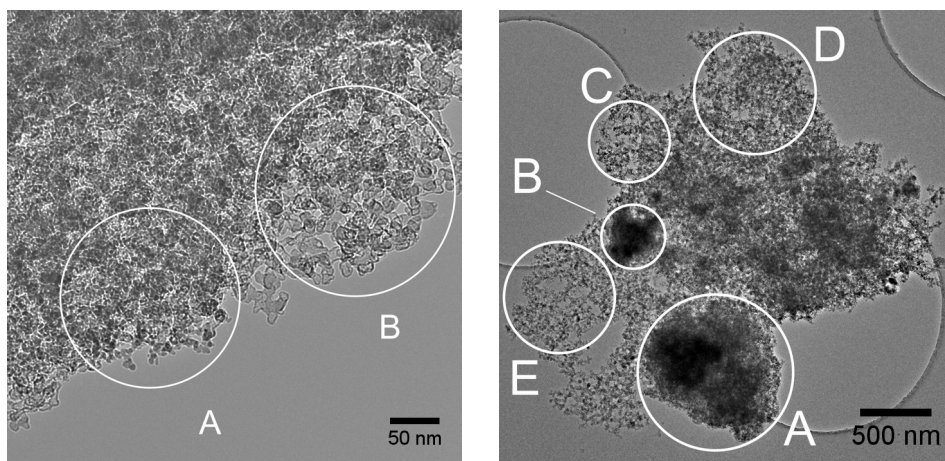
(a) Mg 1.8 mm, Nb 40 Hz.

(b) Mg 1.0 mm, Nb 60 Hz. Nb dots visible.

FIGURE 6.8 TEM images of Mg-Nb composites.

The local degree of catalyst distribution was qualitatively evaluated using TEM/EDX. Due to the lack of calibrated EDX, no one-to-one relation between the EDX and ICP was obtained for the Nb:Mg ratios (Table 3.1). The relative abundance of Nb and Mg was measured on selected areas ranging from 10

to 1000 nm in size (Figure 6.9). On a scale of 100 to 1000 nm, niobium is mostly distributed evenly within each investigated sample, although some areas with either lack or excess of niobium can be found. Throughout sample #6 ( $d_{\text{gap,Mg}} = 1.8 \text{ mm}$ ,  $f_{\text{rep,Nb}} = 40 \text{ Hz}$ ) the abundance of niobium observed with a 50 nm spot size was independent of location at a ratio of  $0.032 \pm 0.002 \text{ Nb/Mg}$  ( $(0.112 \pm 0.004) \text{ g g}^{-1}$ ). When the same sample is observed with a 10 nm spot size a ratio of  $0.107 \pm 0.065 \text{ (g g}^{-1}\text{)}$  was found, indicating that the niobium was no longer distributed homogeneously.



(a) Mg 2.0 mm, Nb 40 Hz. EDX Nb/Mg ratios: A = 0.19, B = 0.00  $\text{g g}^{-1}$ .

(b) Mg 1.8 mm, Nb 100 Hz. EDX Nb/Mg ratios A-E: 1.60, 1.19, 1.43, 1.15 and 0.11  $\text{g g}^{-1}$ .

FIGURE 6.9 Elemental composition of Mg-Nb agglomerates by TEM/EDX.

Particles of unequal sizes show enhanced coagulation in comparison to equally sized particles (see chapter 7), and it is reasonable to expect that Nb particles rapidly deposit on the surface of Mg agglomerates when both aerosols are mixed. The scale down to which Nb can be distributed within the Mg matrix is then directly related to the size the Mg agglomerates have grown to as they reach the Nb spark. The residence time of the aerosol between the two electrode pairs was  $\sim 16 \text{ s}$ . From Smoluchowski theory [66], we estimate a particle number concentration of  $10^{14} \text{ m}^{-3}$  for Mg at the Nb spark. The ablation rate of the Mg spark is  $1 \times 10^{-9}$  to  $1 \times 10^{-8} \text{ mol s}^{-1}$ , as estimated from evaporation efficiency data [42]. The average cluster thus comprised  $6 \times 10^5$  to  $3 \times 10^6$  atoms of Mg, giving a mass equivalent sphere of 30 to 50 nm.

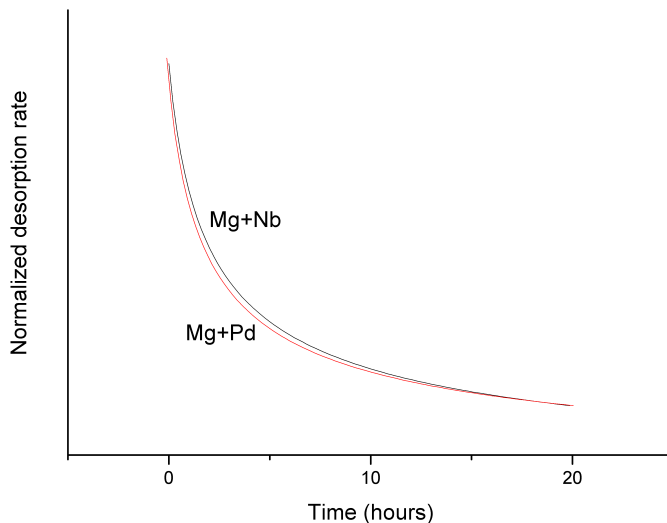


FIGURE 6.10 Normalized fits of hydrogen desorption of spark-generated  $\text{MgH}_2$  doped with Nb (red) and Pd (blue) catalyst.

The particles formed by the spark are not spheres, but agglomerates with a fractal dimension,  $D_f$ , of 2.1 to 2.4 [30], consistent with growth by Diffusion Limited Aggregation (DLA) [147]. The radius of gyration  $R_g$  of the fractal-like agglomerate is calculated from  $R_g = r_{pp} (N_{pp}/k_f)^{1/D_f}$ , where  $k_f$  is a pre-factor and  $r_{pp}$  and  $N_{pp}$  the radius and number of primary particles in the agglomerate, respectively. Using Eggersdorfer, Kadau, Herrmann, et al.'s values for DLA,  $D_f = 2.25$  and  $k_f = 0.82$ ,  $R_g$  of the Mg agglomerates is estimated at 18 to 40 nm. This is consistent with the observation that Nb no longer was homogeneously distributed at a scale below 50 nm

#### 6.4.4 Hydrogen storage properties

The hydrogen ab- and desorption kinetics of the Mg-Nb nanocomposite are similar to those obtained for palladium-catalysed magnesium, desorbing most of the stored  $\text{H}_2$  in 20 h (Figure 6.10). A detailed analysis of the hydrogen storage properties of these spark generated catalyzed materials is reported by Anastasopol, Pfeiffer, Schmidt-Ott, et al. [101, 123].

In short, the observed desorption rates could not be adequately explained through the conventional homogeneous nucleation and growth mechanism as seen in bulk and thin films. Nucleation and growth of MgH<sub>2</sub> were strongly affected by the nanostructure of the material. Instead of assigning a single rate constant to domain growth, a better description of the desorption behaviour was found if a distribution of rate constants was used. This distribution of rate constants reflects the non-homogeneous nature of particulate systems, which are defined by the properties (size, shape, structure, etc.) of the primary particles, and their interfaces.

## 6.5 Conclusions

Catalyst nanoparticles in the form of niobium and niobium oxides could be homogeneously dispersed down to a scale of 50 nm in a magnesium matrix, forming a functional hydrogen storage material. Although one could expect the catalyst content to be related to the relative production rates of the two sparks, no significant correlation was found. This can be attributed in part to poor design of the reactor, which is inducive of diffusional and electrostatic losses. A better defined mixing zone, perhaps such as described in chapter 7, and higher flow rates would benefit process control.

Even though niobium oxides were formed in the presence of metallic magnesium, no significant oxygen transfer to the more electropositive magnesium was observed. After hydrogen cycling at elevated temperatures the NbO<sub>2</sub> reflection at 26.70° 2θ disappears, and the signal for MgO increases.

The degree of distribution of Nb throughout the composite was evaluated using TEM/EDX. The ratio of Nb:Mg is constant down to a scale of ~50 nm throughout the studied samples. This is consistent with the estimated size of Mg-agglomerates as they reach the Nb spark.

## Chapter 7

# Coating of Nanoparticles using Spark Discharge

**A** PPLYING WELL-DEFINED COATINGS to nanoparticles allows novel functions to be introduced to nanostructured material designs. Existing methods rarely focus on small ( $<50$  nm) nanoparticles, and often are poorly transferable to other substrate and coating materials.

A physical method of coating nanoparticles as small as 10 nm with a 1 to 2 nm thin metal coating is described. The vaporized metal deposits on substrate particles in a bimodal coagulation process. There, the deposited domains can grow by surface diffusion, finally yielding smooth or patchy coatings depending on the surface energies,  $\gamma$ , of the two materials. The coating is smooth if the substrate particle is also a metal, and fully surrounds the core if  $\gamma_{\text{coat}} < \gamma_{\text{substrate}}$ .

Aerosols of spherical nanoparticles of Ag, Au or polystyrene latex (PSL) were mixed with supersaturated metal vapours in a hollow electrode spark generator. Au deposits on 80 nm PSL in the form of mostly unagglomerated  $<10$  nm clusters, while it forms a single patch on 20 nm Ag cores. The method employs mild operating conditions and is – apart from the coating morphology – independent of material properties, allowing it to be easily applied for a broad range of substrate and coating materials.

---

Based on T. V. Pfeiffer, P. Kedia, M. Valvo, M. Messing and A. Schmidt-Ott “Coating of nanoparticles using Spark Discharge” *Some Journal* (2014), *manuscript in preparation*.

## 7.1 Introduction

Many applications for nanoparticles benefit from surface functionalization, in the form of protective, conductive, or chemically (in)active coatings, or improved dispersion in or adhesion to a final product matrix [148]. The functionalization can be performed by chemical conversion, such as the partial oxidation of metallic nanoparticles [149], or the formation of a CdSe shell in PbSe quantum dots by ion exchange [150]. Particles suspended in a liquid can also be coated by reduction of metal ions [151, 152]. Gas phase methods have the environmental benefit of not requiring solvents or surfactants. In chemical vapour deposition (CVD), gaseous precursor molecules are decomposed to form condensing species. Typical substrates are metal oxides such as  $\text{SiO}_2$  and  $\text{TiO}_2$ , which are coated by decomposition of organometallic complexes, forming oxides such as  $\text{SiO}_2$  [153] and  $\text{Fe}_2\text{O}_3$  [154], or noble metals such as Pt [155]. Carbon encapsulated particles can be made by decomposition of hydrocarbons [156, 157].

The use of complex precursors is avoided with physical vapour deposition (PVD), i.e. the evaporation or sublimation of a material, and its subsequent condensation onto a substrate. Evaporation furnaces are suitable if the melting point of the substrate particle is significantly higher than that of the coating material, such as for the deposition of Ga on Au [158], or L-leucine on NaCl or lactose [159]. Organic molecules can be deposited on silver nanoparticles, with lower melting point materials having the tendency to form more uniform coatings [160]. Methods that apply focused heating, such as the axial hot wire used to decorate 10 to 50 nm  $\text{SiO}_2$  particles with 1 to 3 nm Au domains, can in theory be used with lower melting point substrates [161].

Models describing CVD coating in the gas phase are based on bimodal approaches to Smoluchowski coagulation [162]. The large substrate particles preferentially scavenge the smaller coating particles. Jain, Fotou, and Kodas take both coagulation and reaction kinetics into account for the decomposition of  $\text{SiCl}_4$  on  $\text{TiO}_2$  particles 1  $\mu\text{m}$  in size [163]. Buesser and Pratsinis study the surface roughness of  $\text{SiO}_2$  coatings, taking into account the decomposition of precursor, growth of coating particles and dilution quenching of the flame [164].

We can expect that the formation of a coating by PVD on a substrate particle will have similarities with the well-understood epitaxial growth of thin films by PVD [165]. The flat, thin films grow as coating atoms and clusters adsorb on the substrate and coagulate by surface diffusion. The morphology of the coating depends on growth kinetics and on the surface free

energy,  $\gamma$ , of the materials used<sup>1</sup>. If the surface free energy of the substrate is larger than that of the coating 2D growth is energetically more favourable, and a smooth layer forms. In the reverse case 3D growth occurs, and so called metal island films form. If the surface energies of both materials are similar, as is the case for Au ( $\gamma_{\text{Au}} \approx 1.50 \text{ eV}$  [166]) and Ag ( $\gamma_{\text{Ag}} \approx 1.25 \text{ eV}$  [166]), combined 2D-3D growth can occur [167]. Metals have high surface energies, while oxide and organic compounds have lower surface energies, implying that a smooth metal coating on an organic core is difficult to achieve. In certain cases thin layers form even if the two materials are deposited simultaneously rather than sequentially, such as evidenced by carbon/metal core shell structures formed by CVD [168] and PVD [32, 169]. In such cases, surface energy dominates.

At small sizes, metal nanoparticles are (partially) liquid at room temperature [170]. The depression of the melting point is caused by the large Laplace pressure due to the curvature of the particle surface. For Au and Ag, this is true for particles up to  $\approx 3 \text{ nm}$  in diameter [171]. This effect has been indirectly observed with spark discharge generated Au nanoparticles, which are spherical below  $5 \text{ nm}$  [38], and structured agglomerates above  $5 \text{ nm}$ . The liquid-like particles can be expected to have a large surface mobility, allowing smooth layers to form upon deposition.

This chapter discusses the coating of nanoparticles with metallic clusters formed by spark discharge. The method is similar to that used to add Pd and Nb catalyst particles to agglomerates of Mg (see chapter 6 and ref. [123]), except that substrate particles are brought in much closer proximity to the spark by means of hollow electrodes. A simple bimodal coagulation model that assumes perfect sintering due to the low melting point of small metallic clusters is compared with experimental results. Different coating morphologies are observed, and are related to the surface energy of substrate and coating. The main benefits of this method comprise a great flexibility with respect to coating material, due to the use of a spark as a vapour source, and a great flexibility in substrate materials due to the mild operating conditions in the system.

---

<sup>1</sup>In this text, the terms surface free energy (eV) and surface tension ( $\text{J m}^{-2}$ ) are (falsely) used interchangeably. For pure liquids, the surface tension is equal to the surface free energy; for solids, it is undefined. The error is mostly in semantics, and we use surface free energy to explain general trends for our  $<3 \text{ nm}$  clusters, which arguably are solid nor liquid proper.

## 7.2 Theory

### 7.2.1 Smoluchowski Coagulation

Coagulation in a monodisperse aerosol can be described using Smoluchowski's model, with the corrections suggested by Fuchs [66]. Brownian motion is responsible for particle collisions, and a coagulation rate

$$\frac{dN}{dt} = -KN^2 \quad (7.1)$$

can be calculated from the particle flux on the surface of a given particle [66].  $N$  is the number concentration of the aerosol.  $K$  is a size dependent parameter, the coagulation kernel. In the continuum regime ( $2\lambda_p < d_p$ ),  $K$  is given by the expression

$$K = 4\pi d_p D. \quad (7.2)$$

The diffusion coefficient  $D$  is calculated using the slip correction factor according to Allen, Bayles, Gile, et al.'s approximation [66, 172]. Hinds provides tabulated values for  $K$ , which vary from  $3 \times 10^{-16}$  to  $12 \times 10^{-16} \text{ m}^3 \text{ s}^{-1}$  for particles  $< 1 \mu\text{m}$  if Fuchs' correction is applied [66].

When considering coagulation of particles of two different sizes  $d_i$  and  $d_j$ , Equation 7.2 is expanded to

$$K_{ij} = \pi (d_i + d_j) (D_i + D_j) \quad (7.3)$$

Because  $d$  increases with decreasing  $D$ , the collision kernel for particles of unequal size is much greater than that of equally sized particles. The fact that smaller particles preferentially collect on big particles can be conveniently used to coat particles.

For the particle sizes in use here, the continuum model is invalid. Instead,  $K_{ij}$  is calculated using the Dahneke approximation for the transition regime and free molecular regime [173, 174].

$$K_{ij} = K_{\text{continuum}} \frac{2 + \kappa}{2 + \kappa(2 + \kappa)}, \quad (7.4)$$

where  $\kappa$  is the ratio of coagulation kernels in the continuum and free molecular regimes.

$$\kappa = \frac{K_{\text{continuum}}}{K_{\text{free molecular}}} = \frac{\pi (d_i + d_j) (D_i + D_j)}{\frac{\pi}{4} (d_i + d_j)^2 \sqrt{\bar{v}_i^2 + \bar{v}_j^2}} \quad (7.5)$$

$\bar{v}_i$  is the mean thermal velocity of a particle of mass  $m_i$

$$\bar{v}_i = \frac{8k_B T}{\pi m_i} \quad (7.6)$$

### 7.2.2 Coalescence of Metal Nanoparticles

When two particles touch, they will attempt to reduce their surface energy by coalescence or sintering. A small particle size and a large surface free energy both contribute to fast sintering [70]. In the case of small metal clusters, which have a lowered melting point compared to bulk [170], this can occur around room temperature. Because the small particles sinter faster than larger ones, and a small cluster deposited on a large substrate particle will rapidly spread out and disappear [147].

If the cluster is of different composition than the substrate particle, the difference in surface free energy,  $\gamma$ , must be taken into account. We can treat the substrate/coating/gas interfaces analogously to contact angle measurements on the solid/liquid/gas interface [175], where

$$\gamma_{sg} = \gamma_{ls} + \gamma_{lg} \cos \theta, \quad (7.7)$$

with the subscripts indicating the interface energy between the solid ( $s$ ), liquid ( $l$ ), and gas ( $g$ ) phase. To obtain a smooth coating the contact angle  $\theta$  must be less than  $90^\circ$ , i.e. the cluster must wet the surface. The liquid will spread out and fully cover the solid surface, providing a smooth and homogeneous coating, if  $\theta = 0^\circ$ , i.e.

$$\frac{\gamma_{sg} - \gamma_{sl}}{\gamma_{lg}} \geq 1. \quad (7.8)$$

Average values for the interface energies in pure elements are readily found in literature (Table 7.1). Some error is introduced when using the tabulated values at room temperature, but the temperature dependence of surface energies is  $\sim 10\%$  from 0 K to the melting point [176]. The difficulty lies in finding a value for  $\gamma_{sl}$  for different substances, which is poorly accessible by experiment. Considering that silver and gold readily alloy, that the bond strengths of Ag-Ag, Ag-Au and Au-Au are similar, and that they have approximately equal  $\gamma_{sl}$ 's in elemental form, we assume that  $\gamma_{\text{Ag-Au}}$  is similar to  $\gamma_{sl}$  of the elements, i.e.  $\sim 0.1 \text{ J m}^{-2}$ . The ratio of surface energies in

TABLE 7.1 Interface energies for silver and gold in  $\text{J m}^{-2}$ , at the melting point (*mp.*) or at 0 K.

Element	$\gamma_{lg,mp.}$ [177]	$\gamma_{sg,0}$ [176]	$\gamma_{sl,mp.}$ [178]
Ag	0.9	1.32	0.11
Au	1.1	1.54	0.13

Equation 7.8 is  $\sim 1.6$  for Ag on a Au substrate, and  $\sim 1.1$  for Au on a Ag substrate. Thus, provided no spontaneous alloy formation occurs, we can expect 2D growth of a smooth Ag film on Au, and combined 2D-3D growth for Au deposited on Ag

Polymers have much lower surface energies than metals, e.g.  $\gamma_{sg} = 0.04 \text{ J m}^{-2}$  for polystyrene [179]. This means that metals deposited on polymers usually have a contact angle  $> 90^\circ$  (Equation 7.8), and will not wet the polymer substrate.

### 7.2.3 Coating model

A substrate aerosol is coated by mixing in a supersaturated metal vapour in a small volume (Figure 7.1). For clarity, we'll refer to the smaller coating particles as clusters to distinguish them from the larger substrate particles. For simplicity, perfect mixing and immediate quenching is assumed, and the repetitive sparks are treated as a continuous vapour source. Bimodal coagulation results in growth of metal clusters and nanoparticles, as well as preferential coating of the substrate particles with the metal. We assume that clusters below 5 nm coalesce [38], and that they do so instantaneously, allowing us to consider all particles as perfect spheres. The final coating morphology is however determined by relative surface energies of the substrate particle and the coating metal as described in subsection 7.2.2.

Coagulation is tracked using the concentration of particles,  $N_i$ , and atoms  $n_i$ . The particles that form the coating are labelled with index 1, substrate particles with index 2. Index  $c$  refers to coating particles collected on the substrate particles. Collisions involving a cluster result in the consumption of one cluster, i.e. a cluster and a substrate particle yield one substrate particle.

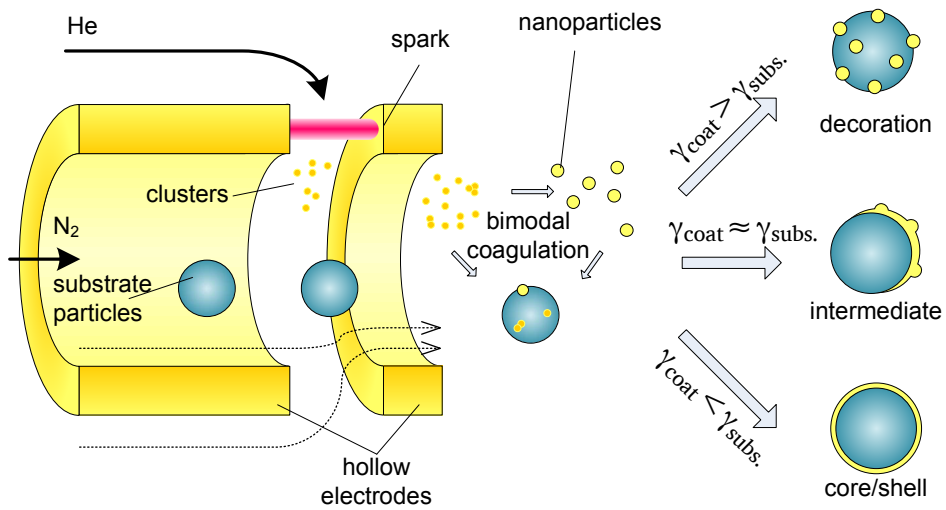


FIGURE 7.1 Schematic model of the coating procedure using a hollow spark. A vapour cloud formed by spark discharge is brought to the substrate aerosol using a He sheath flow. Coating morphology is determined by the surface energy of both materials.

Coagulation can be described with the four differential equations,

$$\frac{dN_1}{dt} = -K_{11}N_1^2 - 2K_{1,2}N_1N_2 - \frac{dN_{w,1}}{dt} \quad (7.9a)$$

$$\frac{dN_2}{dt} = -K_{22}N_2^2 - \frac{dN_{w,2}}{dt} \quad (7.9b)$$

$$\frac{dn_1}{dt} = -2\frac{n_1}{N_1}K_{12}N_1N_2 - \frac{n_1}{N_1}\frac{dN_{w,1}}{dt} = -2K_{12}n_1N_2 - \frac{n_1}{N_1}\frac{dN_{w,1}}{dt} \quad (7.9c)$$

$$\frac{dn_c}{dt} = 2\frac{n_1}{N_1}K_{12}N_1N_2, \quad = 2K_{12}n_1N_2 \quad (7.9d)$$

$\frac{dN_{w,i}}{dt}$  signifies a wall loss term, and  $K_{ij}$  is the coagulation kernel between particles  $i$  and  $j$  [66]. For  $N_2 \ll N_1$  the self-collision rate and diffusional losses of substrate particles are small, and Equation 7.9b is neglected in the calculations. Diffusional losses are estimated using Hinds' approximation of the empirical expression by Gormley and Kennedy for laminar flow [66],

$$\mathbb{P} = \frac{N_{\text{in}}}{N_{\text{out}}} = 1 - 5.50\mu^{2/3} + 3.77\mu, \quad \text{with} \quad (7.10)$$

$$\mu = \frac{DL}{Q}, \quad (7.11)$$

where  $\mathbb{P}$  is the fraction of particles passing through the tube,  $Q$  is the volumetric flow rate, and  $L$  is the length of the tube. Equation 7.11, which is accurate to  $<1\%$  for  $\mu < 0.009$ , is size-dependent, and is evaluated taking the variable size of the clusters into account.

The size of clusters, coated particles and coating thickness are given by

$$d_1 = \left( \frac{n_1}{N_1} \frac{M_1}{N_A \rho_1} \right)^{1/3},$$

$$d_2 = \left( V_{2,0} + \frac{n_c}{N_2} \frac{M_1}{N_A \rho_1} \right)^{1/3}, \quad \text{and}$$

$$\bar{x}_c = d_2 - d_{2,0}$$

respectively, where  $V_{2,0} = \pi/6 \times d_{2,0}^3$  is the initial volume of the substrate particles.

## 7.3 Experimental

### 7.3.1 Coating setup

The setup consists of three sections: substrate particle formation, coating, and particle collection (Figure 7.2).

Spherical substrate particles of Ag were formed by sintering of agglomerates formed by spark discharge [39, 42]. Sintering temperatures in the tube furnace were 1073 K for Ag and 1173 K for Au. Alternatively, 80 nm ( $\pm 18\%$ ) polystyrene-latex (PSL) spheres (Duke Scientific 5008A) were aerosolized from suspension using a pressurized jet atomizer, followed by a diffusion drier [66]. Size selecting the generated aerosol using a differential mobility analyzer (DMA) is possible at this stage, but requires a neutralizer after the DMA to avoid electrostatic losses in the coating zone. Nitrogen was used as a carrier gas with a flow rate of  $1.6 \text{ L min}^{-1}$ .

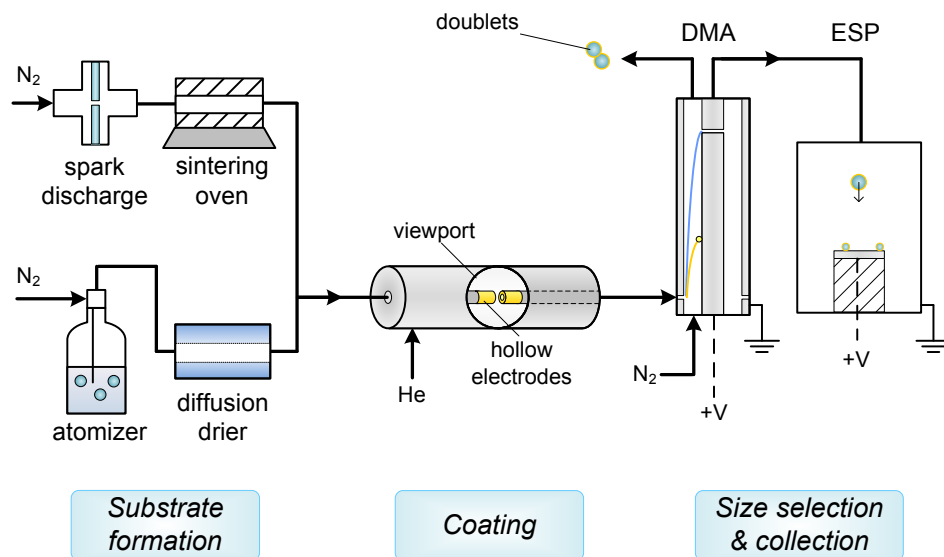


FIGURE 7.2 Process schematic including substrate particle generation, particle coating, and size selection and collection. DMA - Differential mobility analyzer, ESP - Electrostatic precipitator

The coating zone is built from stainless steel, and consists of a NW-35CF tee with two axially aligned tubes of 4 mm inner and 6 mm outer diameter. Cylinders  $\sim 1$  cm in length of Au and Ag (99.99%, MaTeck GmbH) of the same

diameters were attached to the tips of the steel tube by means of compression in a small brass ring. A sheath flow of  $2 \text{ L min}^{-1}$  He is introduced at the start of the tee. Otherwise, the spark is essentially identical to that described by [42], using a 2 nF capacitance, 15 mA charging current, and 0.3 kV (Ag) and 0.7 kV (Au) mean voltage. The coagulation zone consisted of 0.2 m steel tubing, giving a residence time of  $\sim 40$  ms.

After coating, the excess clusters are filtered out using a differential mobility analyzer (DMA) [180]. The DMA was operated at a broad transfer function (1:2 aerosol:sheath ratio) to ensure high transmission of the coated particles. The spark generator generated a sufficiently charged aerosol to avoid the need for a neutralizer. Particles were collected in an electrostatic precipitator on 200 mesh copper TEM grids with  $50 \mu\text{m}$  holey carbon foil (SPI Supplies) for off-line analysis.

### 7.3.2 Characterization

Aerosol concentrations and mobility size distributions of Ag and Au and PSL core particles were measured using the DMA as a Differential Mobility Particle Sizer (DMPS), with a CPC (TSI-3776) as detector. Transmission electron microscopy (TEM) was performed using a FEI monochromated Tecnai 200STEM-FEG operated at 200 kV, and a JEOL JEM 1400 operated at 100 kV. HRTEM and energy dispersive X-ray spectroscopy (EDX) were performed on a JEOL 300F with a FEG, operated at 300 kV. Image analysis was performed using the public domain ImageJ software package [86]. Coagulation simulations were performed using MATLAB software (The Mathworks, Inc.).

Raman spectroscopy was performed on a Renishaw inVia Raman microscope, using excitation wavelengths of 532 nm (0.5 mW) and 633 nm (0.05 mW). The spectra were recorded as 20 cumulative 20 s scans under 50x magnification, and were calibrated from the  $520.6 \text{ cm}^{-1}$  reflection of monocrystalline [100] Si.

## 7.4 Results

### 7.4.1 Coating model

Figure 7.3 shows the dependence of  $K_{12}$ , scaled to the monodisperse coagulation kernels, on the size ratio of substrate particle to coating particle. In the size range of interest, 10 to 100 nm,  $K_{12}$  exceeds  $K_{11}$  by one to four orders

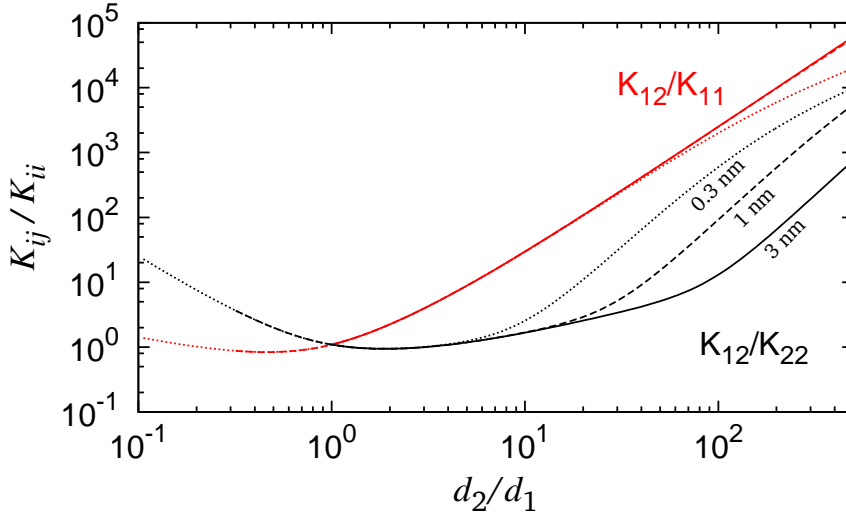


FIGURE 7.3  $K_{12}$  normalized to  $K_{11}$  (red) and  $K_{22}$  (black) vs. relative particle size.  $d_2 = 0.3$  nm (dotted lines),  $d_2 = 1$  nm (dashed lines) and  $d_2 = 3$  nm (solid lines). Substrate is Ag, coating is Au.

of magnitude, indicating that the substrate particles will scavenge the coating particles [162]. In practice  $N_1 \gg N_2$ , and the coagulation rate for 1-1 collisions will exceed that for 1-2 collisions (Equation 7.9a & 7.9b), resulting in non-negligible growth of the clusters.

The simulated growth of Au clusters and coating on 20 nm Ag particles is plotted in Figure 7.4 for initial concentrations of  $N_{1,0} = 2 \times 10^{20} \text{ m}^{-3}$ , and  $N_{2,0} = 1.5 \times 10^{13} \text{ m}^{-3}$ . The initial concentrations for coating and substrate particles mimic experimental concentrations as estimated from the ablation efficiency [42], and measured by DMPS, respectively. The number concentration and diameter of clusters evolves essentially identical for 10 to 80 nm substrate particles. Minor differences in coating thickness exist because small particles are more sensitive to volume change than the bigger particles. In fact,  $n_c$  scales with the square of the substrate particle size, i.e. the available surface area. For the  $\sim 40$  ms residence time of the experiment, a coating thickness of 0.6 to 0.8 nm is predicted, while clusters have grown to a size of 3.5 to 3.7 nm.

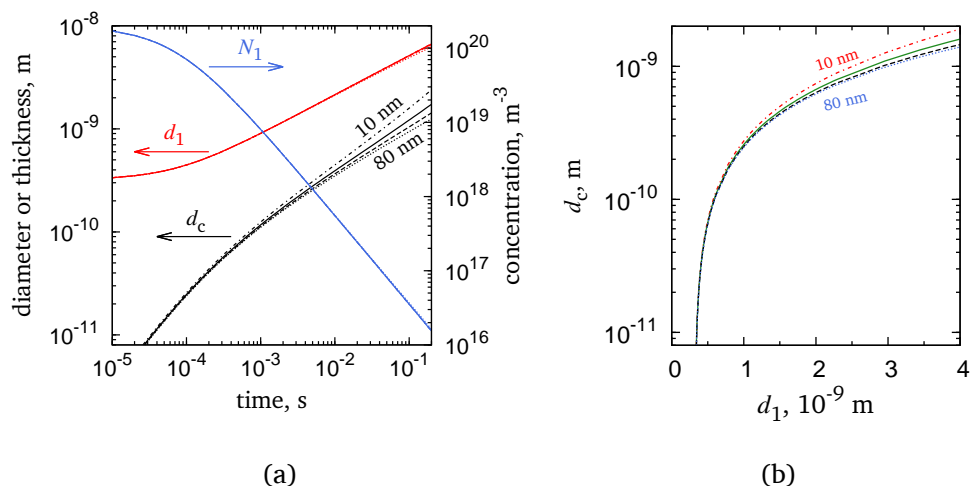


FIGURE 7.4 Coagulation results for Ag cores coated with Au.  $N_{1,0} = 2 \times 10^{20} \text{ m}^{-3}$ ,  $N_{2,0} = 1.5 \times 10^{13} \text{ m}^{-3}$ . (a) Cluster consumption (blue), cluster size (red) and coating thickness (black) vs. time. (b) Coating thickness vs. cluster size. *solid*:  $d_{2,0} = 10 \text{ nm}$ , *dash*: 20 nm, *dash-dot*: 40 nm, *dots*: 80 nm.

#### 7.4.2 Au on PSL

Figure 7.5 shows TEM micrographs of gold coated PSL spheres collected during one hour. The PSL substrate spheres had diameters of  $(67 \pm 6) \text{ nm}$ , i.e. in the lower end of the stated 80 nm particle size. The large difference in density between PSL and Au results in high contrast, and dark Au domains are clearly visible on the PSL spheres. The dark domains show lattice spacings of 0.23 to 0.24 nm. No size-selection was performed, resulting in a large (25%) surface coverage of Au on the carbon film. The majority of PSL particles has deposited on top of the carbon film, or as agglomerates (Figure 7.5a, insert), making it impossible to distinguish on what surface the Au cluster has deposited. These particles are ignored, and measurements are performed on PSL particles suspended over the holes in the carbon film. This gives a surface coverage of Au on PSL of 12.5%, measured over  $1.1 \times 10^4 \text{ nm}^2$ , i.e.  $\sim 3$  particles.

The surface equivalent particle size of deposited Au clusters was obtained from their projected surface area. Figure 7.5c shows size distributions of Au deposited on PSL particles for spherical (circularity  $> 0.8$ ) primary particles and non-spherical (circularity  $\leq 0.8$ ) agglomerates. ‘Agglomerates’ below  $\sim 1.3 \text{ nm}$  in size are included for consistency, although the image resolution

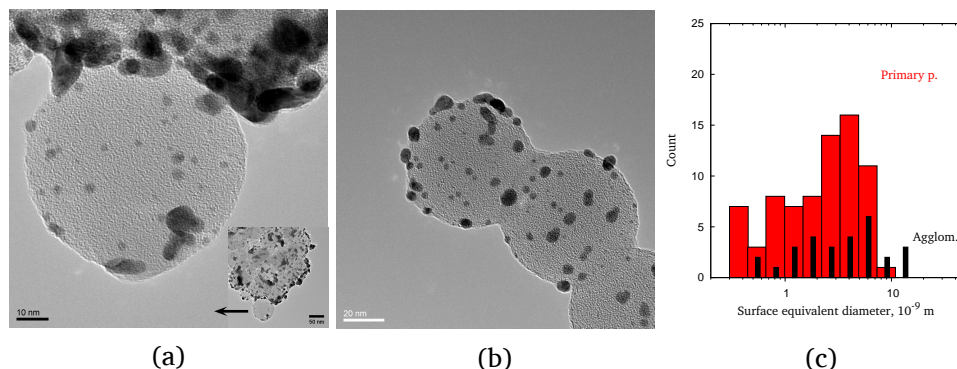


FIGURE 7.5 Gold-decorated PSL spheres. (a) and (b) TEM micrographs, scale bars 10 nm and 20 nm. (c) Size distribution of spherical and agglomerated clusters deposited on PSL.

through the 80 nm PSL particle precludes an accurate shape measurement. The size distributions for Au particles deposited on the film are shown in Figure 7.6. The image resolution provided a lower cut-off at 2.2 nm, resulting in an estimated modal primary particle size of 2 to 4 nm. Part of the agglomerates will have formed on the TEM grid, by particles depositing on already deposited particles. In addition to the single PSL spheres, indication of necking was observed on a number of PSL spheres (Figure 7.5b). It is uncertain whether this neck formed by sintering in the spark, or under influence of the electron beam.

Several unexpected structures were observed during the TEM investigations, that warrant a separate discussion. Firstly, Figure 7.7a shows a fibrous structure several micrometers in length, with a mean diameter of 50 nm. The large size of the fiber indicates that it is an entrained agglomerate that formed on the reactor walls. The dense packing and alignment suggests the fiber formed under influence of an electric field [181], probably just downstream of the electrode gap.

Secondly, at high spark energy several spherical gold particles, formed by melt pool ejection [42], were observed (Figure 7.7b). The Au spheres were 0.1 to 0.5  $\mu\text{m}$  in diameter, and were decorated with 5 to 20 nm Au particles. These 'wetting droplets' had partially sintered with the larger particle, consistent with a liquid-like surface of small particles. Lattice fringes with a periodicity of 0.2355 nm, corresponding to the [111] plane of Au, were observed for the smaller particles. These results confirm that there is an upper limit, <5 nm, to the coating cluster size, if a smooth coating is desired.

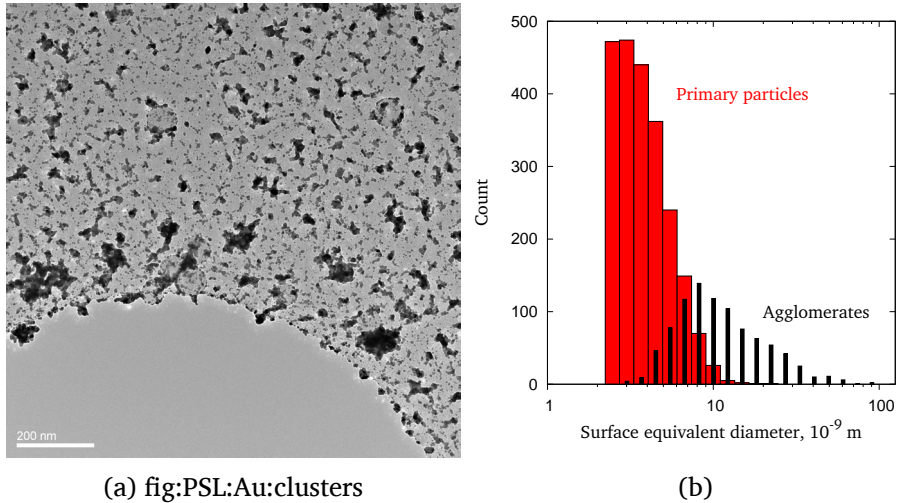


FIGURE 7.6 Clusters and agglomerates of Au, and several PSL spheres collected on carbon foil. (a) TEM micrograph, 200 nm scale bar, (b) size distributions of Au primary particles and agglomerates.

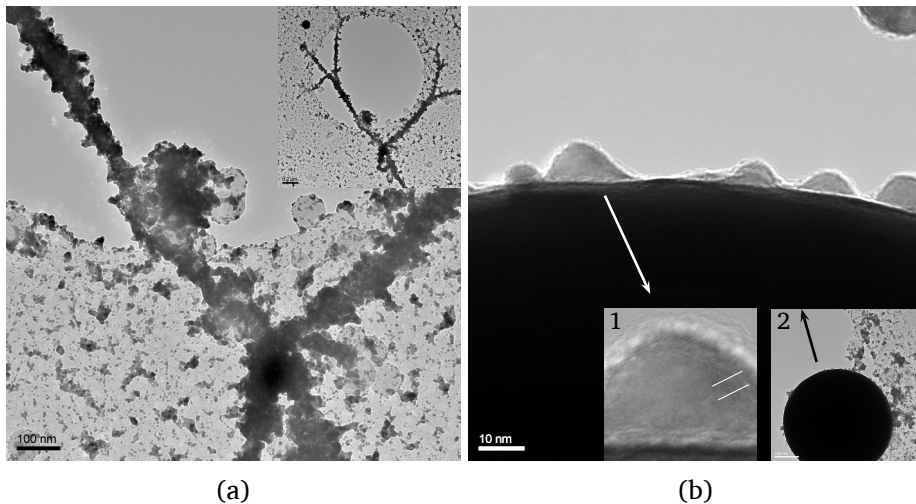


FIGURE 7.7 Other observed structures. (a) Branched wires, insert: overview. (b) 'Splashed' microdroplet of Au with Au coating, inserts: (1) detail: [111] lattice fringes, (2) overview. Scale bars (a) 100 nm (insert: 200 nm), (b) 10 nm (insert 2: 100 nm).

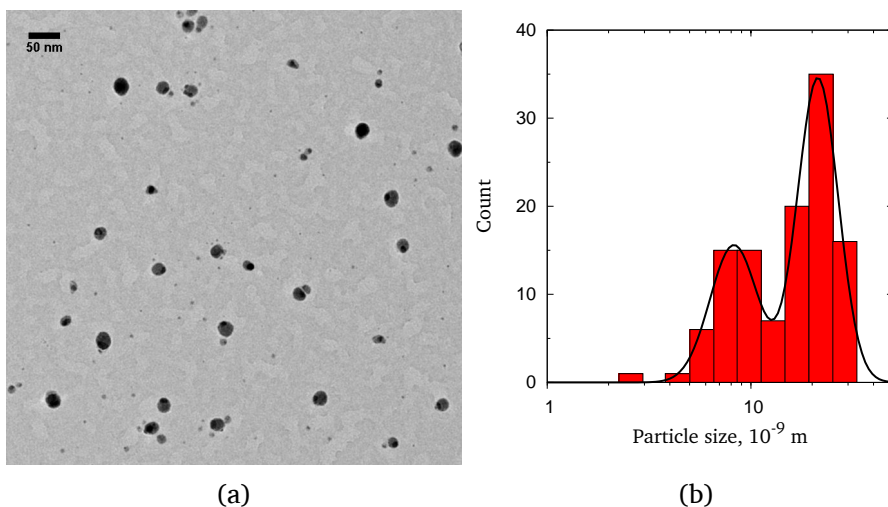


FIGURE 7.8 Au-coated Ag nanoparticles observed by TEM. (a) TEM micrograph, scale bar 50 nm. (b) Corresponding size distribution of Ag substrate particles. The solid line is a log-normal approximation. Size distribution of Ag substrate particles observed via TEM. The solid line is a log-normal approximation.

#### 7.4.3 Au on Ag

Figure 7.8 shows Ag core particles partially coated with a cap of Au, visible as a dark patch on a lighter core. The size distribution of 116 particles with well-resolved coatings appears to be bimodal, with mean sizes of 8.2 nm and 21 nm (Figure 7.8b). A significant number of small particles with a count median diameter of 3.6 nm can be seen throughout the samples (Figure 7.9a). These are identified as gold clusters that have passed through the DMA due to the broad transfer function of the DMA and their high diffusivity. The clusters are approximately equal in number to the coated particles (Figure 7.8b).

High resolution images of the patchy particles are given in Figure 7.9. EDX of the light zones shows the presence of Ag and S, as well as some Au. Excluding sulfur, 10 individual particles had a Au content of  $(17 \pm 13)\%$ , with no notable correlation between particle size and Au content. The particles contain Ag and S in an atomic ratio ranging from 1.1:1 to 3.2:1, on average corresponding to the composition of  $\text{Ag}_2\text{S}$ . As the samples were stored in air prior to analysis, and silver easily tarnishes in air to form  $\text{Ag}_2\text{S}$  (see chapter 4), it is likely that the sulfide formed after synthesis. Partial sulfidation during synthesis could however not be excluded. Lattice spacings of 0.167 nm in the

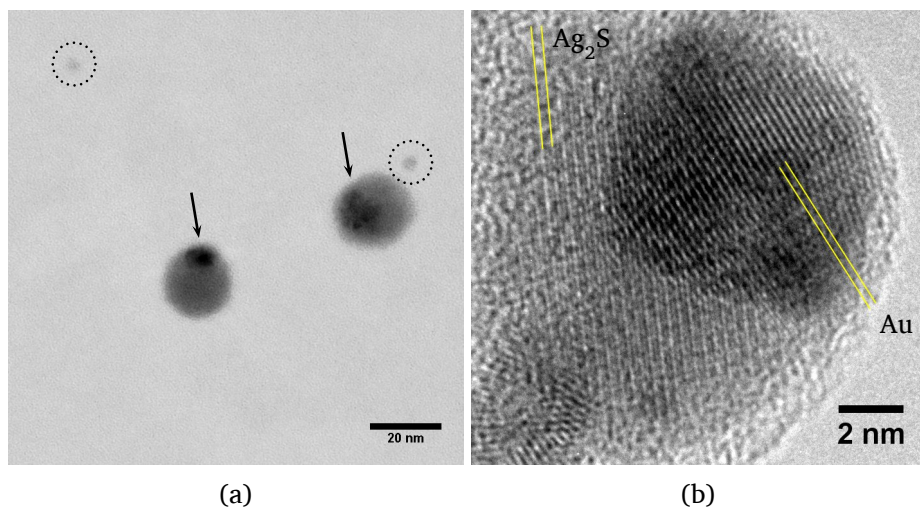


FIGURE 7.9 HRTEM micrographs of Au-coated Ag nanoparticles. (a) 20 nm Ag, with dark Au patch (arrow), and smaller Au clusters (circled), scale bar 20 nm. (b) Lattice fringes, scale bar 2 nm.

light zones, assigned to either the [041] or [033] plane of  $\text{Ag}_2\text{S}$ , confirm that the substrate particles consist of sulfidated silver (Figure 7.9b).

The dark spots were observed on all particles larger than 7 nm, the majority of which had exactly one spot per particle. The dark spots cover 10 to 90 % of the projected surface area of their substrate particle. Elemental analysis on the dark spots confirms the presence of gold. Unlike silver, gold is known not to form a tarnish, even when alloyed [182]. The observation of lattice fringes with a spacing of 0.231 nm, assigned to the [111] plane of either Ag or Au, confirms that the dark spots comprise metallic gold (Figure 7.9b).

From particles where the dark spot is on the edge of the particle, and appears to envelop the silver core, we conclude that the dark spots are a coating of the heavy Au on the lighter Ag cores, as opposed to doublets aligned parallel to the electron beam. This is consistent with observations by SEM.

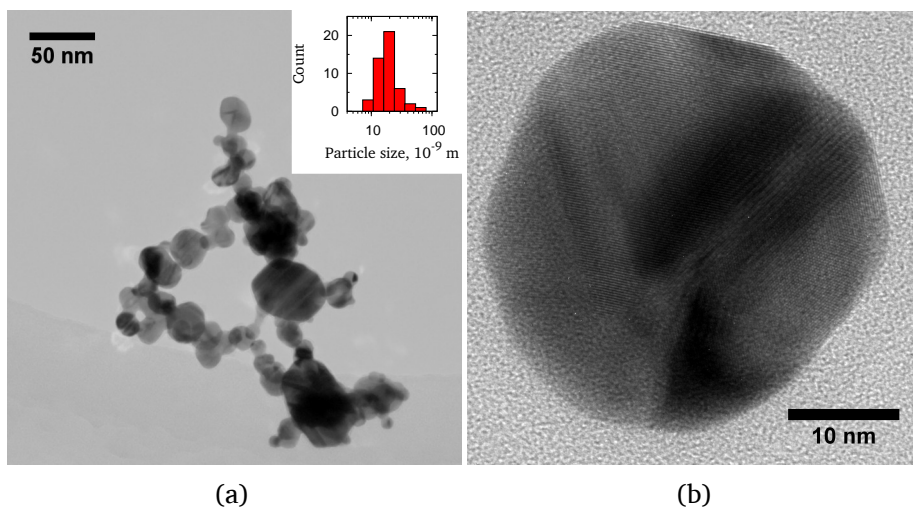


FIGURE 7.10 TEM micrographs of Ag-coated Au-core nanoparticles. (a) Agglomerate; *insert*: size distribution within the agglomerate, (b) Singlet. Scale bars indicate 50 nm and 10 nm.

#### 7.4.4 Ag on Au

TEM shows that the Ag-coated Au particles consist of a large fraction of agglomerates (Figure 7.10a), and a small number of spheroid singlets and doublets (Figure 7.10b). The inter-particle connections within the agglomerates are in various states of sintering, indicating that agglomeration was occurring in the sintering oven, as well as after the sintering oven. The continued coagulation is due to the high aerosol concentration of Au, which has larger ablation efficiency in spark discharge than Ag [42]. EDX and lattice fringe measurements confirm that the particles are Au. No silver was detected by EDX on single particles.

Some of the Au particles appeared to be surrounded by a smooth shell,  $(1.5 \pm 0.3)$  nm thick (Figure 7.11). The Au particles appear to always touch (Figure 7.11c), suggesting that the layer surrounds the agglomerates, rather than the primary particles. This would indicate the layer formed after coagulation. Since the layer could not be detected under high resolution TEM, and no silver was detected, this layer is considered an organic contaminant that formed by decomposition of volatile species on the Au surface.

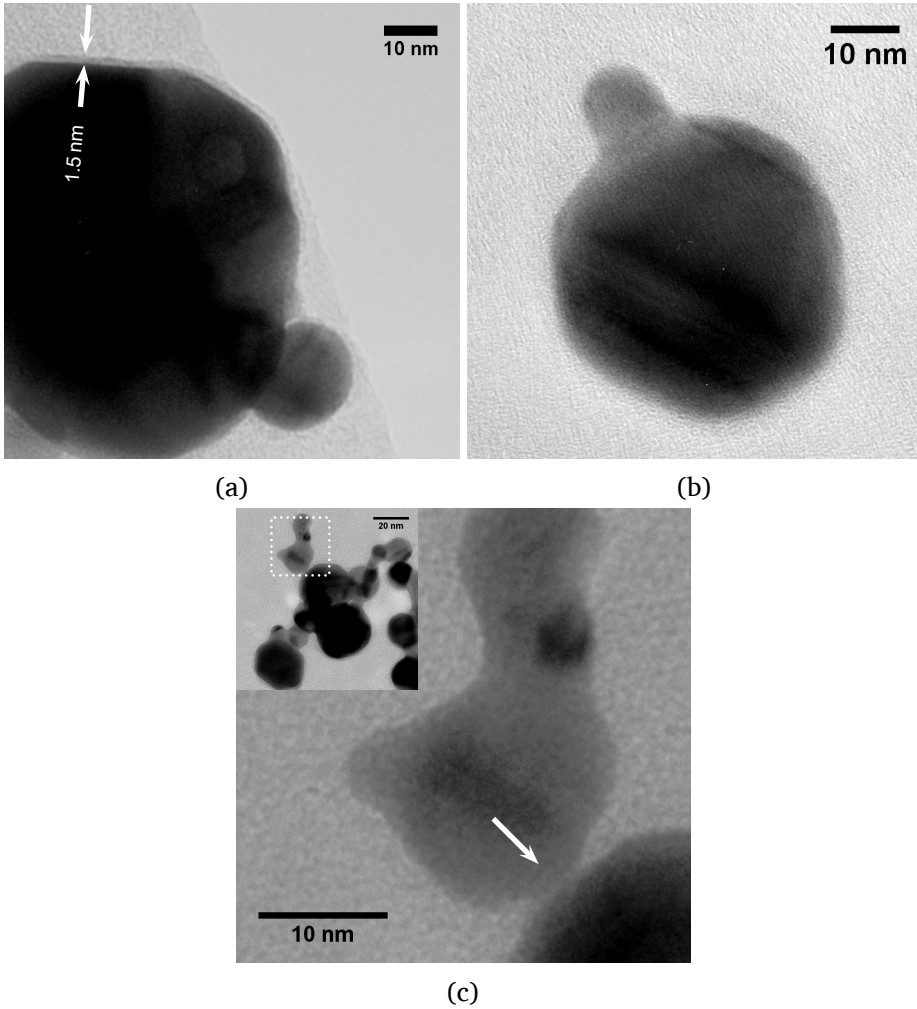


FIGURE 7.11 TEM micrographs of the Ag-coating on Au nanoparticles. (a) particle with thin shell, (b) Scale bars indicate 10 nm (insert: 20 nm).

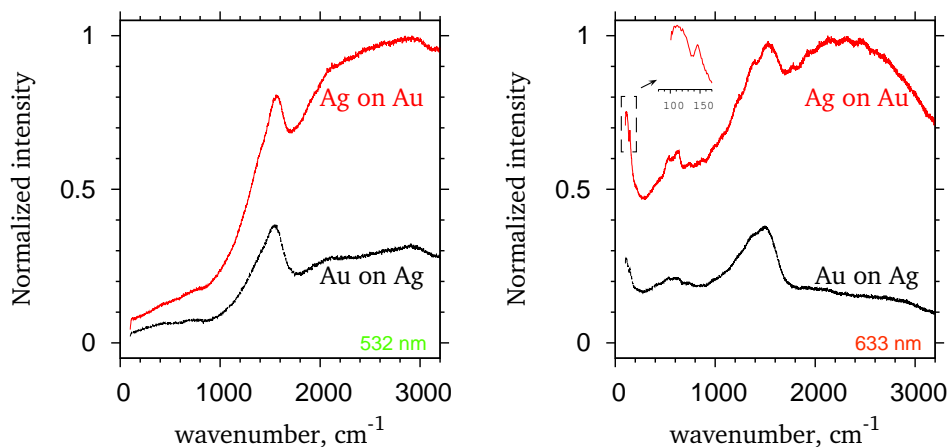


FIGURE 7.12 Background corrected, normalized Raman spectra for Au-coated Ag and vice versa. (a) 532 nm excitation, (b) 633 nm excitation.

#### 7.4.5 Raman spectroscopy

To test if any silver below the detection limit of EDX had deposited on the gold substrate particles, Raman spectroscopy was performed on the collected particles. Our approach is similar to in surface-enhanced Raman spectroscopy, where the excitation of the surface plasmon resonance of metal nanoparticles results in strongly enhanced Raman scattering by molecules adsorbed on their surface [183]. Upon exposure to air, any Ag deposited on a Au core particle will tarnish, forming e.g.  $\text{Ag}_2\text{O}$  or  $\text{Ag}_2\text{S}$  (chapter 4). If the Raman scattering of the silver tarnish compound is sufficiently enhanced, even low Ag concentrations could be detected, demonstrating that some Ag deposited on the Au particles.

Both types of Ag-Au composite particles show a strong Raman signal under 532 nm and 633 nm excitation. Under 532 nm excitation, the Ag and Au core particles show a dominant mode at  $1755\text{ cm}^{-1}$  and  $1540\text{ cm}^{-1}$ , respectively. Under 633 nm excitation, vibrational modes at (111), 146, 539, 635, (1243),  $\sim 1396$  and  $1529\text{--}1550\text{ cm}^{-1}$  can be identified for the Au cores. The stronger of these features are for the Ag cores, shifted by  $\sim 5\text{ cm}^{-1}$  to lower wavenumbers. The Au core particles show a broad fluorescence in the range  $1800$  to  $3000\text{ cm}^{-1}$  under both excitation wavelengths.

The main Raman features of the silver tarnish compounds  $\text{Ag}_2\text{S}$ ,  $\text{Ag}_2\text{O}$  and  $\text{AgCl}$  occur in the range  $100$  to  $500\text{ cm}^{-1}$  [184–186]. Getting a good

Raman spectrum for these compounds is difficult, as they have weak vibration modes and are prone to photo-degradation under the excitation laser [186]. The characteristic band around  $220\text{ cm}^{-1}$  of  $\text{Ag}_2\text{O}$  is absent (Figure 7.12). The signals at  $111\text{ cm}^{-1}$  and  $146\text{ cm}^{-1}$  match well with Ag lattice vibrations in  $\text{Ag}_2\text{S}$  and  $\text{Ag}_2\text{SO}_3$ , but no Ag-S modes were observed [187]. The higher wavenumber signals could not be attributed to any specific species, but are considered to originate from organic surface contaminants. Given that  $\text{Ag}_2\text{S}$  was observed by TEM on the Ag core particles (Figure 7.9b), it is plausible that the vibrations at  $111\text{ cm}^{-1}$  and  $146\text{ cm}^{-1}$  indeed correspond to  $\text{Ag}_2\text{S}$ .

## 7.5 Discussion

The simulations show strong competition between 1-1 and 1-2 collisions, resulting in rapid growth of the coating clusters. In order to achieve a homogeneous coating, it is important that these coating clusters stay sufficiently small to be mobile. This should be the case for clean gold and silver clusters smaller than about 2.5 nm, at which size they have a melting point around room temperature [170, 171]. Thus, from Figure 7.4b we can expect smooth coatings up to 0.8 to 1.0 nm in thickness for a wetting coating. The experimental cluster size of 2 to 5 nm (Figure 7.5c) fits well with the 3.6 nm obtained from the model. The presence of  $<1$  nm clusters confirms that cluster growth and substrate coating occur simultaneously.

From the TEM results we find that the volume of gold clusters deposited on PSL spheres is  $4.8 \times 10^3$  to  $6.9 \times 10^3\text{ nm}^3$ , or  $1 \times 10^5$  atoms per sphere. The model slightly overestimates coating on PSL spheres, predicting  $7 \times 10^5$  atoms per particle. The size of the Au patches on Ag core particles as determined by EDX corresponds to a conformal shell with a thickness of 1.1 to 1.3 nm. Comparison with Figure 7.4 shows that the model underestimated the coating rate for silver cores.

Several factors contribute to the observed deviations from theory. The presence of large agglomerates of PSL spheres, which scavenge a disproportionate amount of Au, and the substrate size being slightly smaller than modeled, both explain why less gold than expected deposited on PSL. On the other hand, the Ag substrate particles are rather small. This could lead to the model underestimating their loss by diffusion to the wall, increasing the Au:Ag ratio, i.e. coating thickness, of the final product. More importantly, the model does not take polydispersity into account. From the decent agreement between model and observation we do however conclude that conceptual ap-

proach of the simple model, i.e. bimodal coagulation of a metal vapour with substrate particles, is valid.

It is unlikely that *no* Ag deposited on the Au cores. Low concentrations of silver on the Au cores can be understood from its lower ablation rate [42]. The Ag vapor concentration in the hollow spark is estimated to be  $2 \times 10^{19} \text{ m}^{-3}$ , a factor 10 lower than that of Au. At the same time, again due to the difference in ablation rates, the Au core particles were both larger in size and more abundant. The net result is less coating material being spread out over a larger surface area, resulting in a thinner coating. One or a few layers of Ag or  $\text{Ag}_2\text{S}$  would be impossible to detect via TEM, and the contribution of Ag to the EDX signal would be negligible compared to the bulk of the Au core particles. Thus, despite the possible presence of  $\text{Ag}_2\text{S}$  in the Raman spectra, the presence of Ag on the Au substrate particles could not be confirmed conclusively.

The Ag coating on Au particles is homogeneous and smooth, and we conclude that the freshly deposited Ag clusters are (partially) liquid-like, allowing their constituent atoms to spread over the substrate. The ‘wetting droplet’ features found on the Au splash droplet (Figure 7.7b) likely consist of a single Au particle that collided with the substrate particle; surface diffusion of multiple clusters would result in flatter structures. This shows that even  $\sim 6 \text{ nm}$  Au clusters are not rigid solids under the conditions in the system. It is somewhat striking that unagglomerated  $< 1 \text{ nm}$  Au clusters could be observed on PSL, indicating that the surface mobility of Au on PSL is low.

In contrast, gold forms a single but smooth patch on silver. These observations match well with the predictions of Equation 7.8, which shows that Ag fully wets Au, while the contact angle of Au cluster on a Ag substrate has a contact angle close to  $0^\circ$ , resulting in combined 2D/3D growth to form the observed partial coating. The case of silver on gold, which should form a homogeneous layer that fully covers the substrate particle, was not observed due to the low silver content.

The temperature history of the coated aerosol will affect both substrate and coating morphology. The aerosol is at room temperature when it enters the coating zone, and is rapidly heated up by the spark. About 20% of the spark energy is converted to thermal energy of the plasma [29], and under the assumption of ideal mixing and no heat conduction through the tube walls we find that the mean temperature of the gas cannot exceed 330 K. The PSL spheres appear to be largely unaffected by sintering effects, with only minor apparent necking occurring (Figure 7.5b). The glass transition temperature of PSL is  $\sim 373 \text{ K}$  [188], and it is unlikely that heat from the spark caused the

observed sintering. The sintering is most likely caused by the UV radiation emitted by the spark, which is strongly absorbed by polystyrene and leads to physical and chemical changes [188].

The transmission of charged particles through the coating setup is very poor due to the electric field around the gap, requiring the use of a neutralizer downstream of the atomizer. To obtain a more narrow distribution of coated particles, it is desirable to place a DMA before the coating zone. A bipolar charger downstream of that DMA will be effective to neutralize aerosols with particle sizes  $\leq 100$  nm [89]. A significant fraction of the particles exiting the coating chamber is partially charged, a phenomenon typical of spark discharge [42], which allowed size selection and particle collection without applying additional charging.

A final remark must be made on the efficiency of the coating process. For the conditions used in this paper, 0.1 to 5 % of the ablated coating material deposits on the substrates, 21 % is lost by diffusion to the reactor walls, and 74 to 79 % of the ablated mass ends up in the form of free clusters. The coating efficiency can be improved by increasing the available substrate area through  $d_p$  or  $N_2$ . Increasing the residence time will result in a further growth of the coating clusters, and can adversely affect the quality of the coating.

## 7.6 Conclusion

Ag and Au coatings of  $\sim 1$  nm thickness were deposited on substrate particles using a novel hollow spark configuration. The morphology of the film is defined by the surface energies of the different materials: high surface energy metals will form a multitude of small clusters on a low surface energy organic substrate, while metals of similar surface energy will form smooth coatings. In the case of Au deposited on Ag an incomplete but smooth coating covers the substrate like a cap. The inverted case, which would give a conformal coating, could not be confirmed.

The simple coagulation model shows that particles from 10 nm to several hundreds of nanometers in diameter can be coated, and that the coating efficiency is only weakly dependent on material properties. Combined with the spark as a flexible vapour source, this in principle allows the method to be extended to the deposition of any metal. Despite the high temperature in the spark, quenching is sufficient to result in near room temperature deposition. This allows the use of 'soft' substrates, in addition to any of the more usual substrate materials.

# Bibliography

- [1] *International Energy Outlook 2013* U.S. Energy Information Administration, 2013
- [2] K. E. TRENBERTH, J. T. FASULLO, and J. KIEHL “Earth’s Global Energy Budget” *Bulletin of the American Meteorological Society* **90**: (2009), 311–323 DOI: 10.1175/2008BAMS2634.1
- [3] O. P. R. VAN VLIET, T. KRUIHOF, W. C. TURKENBURG, and A. P. C. FAAIJ “Techno-economic comparison of series hybrid, plug-in hybrid, fuel cell and regular cars” *Journal of Power Sources* **195**: (2010), 6570–6585 DOI: 10.1016/j.jpowsour.2010.04.077
- [4] *Elektrisch rijden* Rijksdienst voor Ondernemend Nederland 2013 URL: <http://www.rvo.nl/onderwerpen/duurzaam-ondernemen/energie-en-milieu-innovaties/elektrisch-rijden/> (visited on 02/28/2014)
- [5] *Motorvoertuigen; aantal voertuigen en autodichtheid per provincie* Centraal Bureau voor de Statistiek 2013 URL: <http://statline.cbs.nl/> (visited on 02/28/2014)
- [6] V. S. KOLOSNIYSYN and E. V. KARASEVA “Lithium-sulfur batteries: Problems and solutions” en *Russian Journal of Electrochemistry* **44**: (2008), 506–509 DOI: 10.1134/S1023193508050029
- [7] J. CHRISTENSEN, P. ALBERTUS, R. S. SANCHEZ-CARRERA, T. LOHMANN, B. KOZINSKY, R. LIEDTKE, J. AHMED, and A. KOJIC “A Critical Review of Li/Air Batteries” en *Journal of The Electrochemical Society* **159**: (2012), R1–R30 DOI: 10.1149/2.086202jes
- [8] S. M. ACEVES, G. D. BERRY, J. MARTINEZ-FRIAS, and F. ESPINOSA-LOZA “Vehicular storage of hydrogen in insulated pressure vessels” *International Journal of Hydrogen Energy* **31**: (2006), 2274–2283 DOI: 10.1016/j.ijhydene.2006.02.019
- [9] B. SAKINTUNA, F. LAMARI-DARKRIM, and M. HIRSCHER “Metal hydride materials for solid hydrogen storage: A review” *International Journal of Hydrogen Energy* **32**: (2007), 1121–1140 DOI: 10.1016/j.ijhydene.2006.11.022
- [10] V. VONS, A. ANASTASOPOL, W. LEGERSTEE, F. MULDER, S. ELJT, and A. SCHMIDT-OTT “Low-temperature hydrogen desorption and the structural properties of spark discharge generated Mg nanoparticles” *Acta Materialia* **59**: (2011), 3070–3080 DOI: 10.1016/j.actamat.2011.01.047

- [11] C. MARAMBIO-JONES and E. M. V. HOEK “A review of the antibacterial effects of silver nanomaterials and potential implications for human health and the environment” en *Journal of Nanoparticle Research* **12**: (2010), 1531–1551 DOI: 10.1007/s11051-010-9900-y
- [12] H. SHIRAKAWA, E. J. LOUIS, A. G. MACDIARMID, C. K. CHIANG, and A. J. HEEGER “Synthesis of electrically conducting organic polymers: halogen derivatives of polyacetylene,  $(\text{CH})_x$ ” en *Journal of the Chemical Society, Chemical Communications* (1977), 578–580 DOI: 10.1039/C39770000578
- [13] D. BULGIN “Electrically Conductive Rubber” *Rubber Chemistry and Technology* **19**: (1946), 667–695 DOI: 10.5254/1.3543222
- [14] A. S. ARICÒ, P. BRUCE, B. SCROSATI, J.-M. TARASCON, and W. VAN SCHALKWIJK “Nanostructured materials for advanced energy conversion and storage devices” *Nature Materials* **4**: (2005), 366–377 DOI: 10.1038/nmat1368
- [15] S. SINGH, S. EIJT, J. HUOT, W. KOCKELMANN, M. WAGEMAKER, and F. MULDER “The  $\text{TiCl}_3$  catalyst in  $\text{NaAlH}_4$  for hydrogen storage induces grain refinement and impacts on hydrogen vacancy formation” *Acta Materialia* **55**: (2007), 5549–5557 DOI: 10.1016/j.actamat.2007.06.028
- [16] M. GRÄTZEL “Dye-sensitized solar cells” *Journal of Photochemistry and Photobiology C: Photochemistry Reviews* **4**: (2003), 145–153 DOI: 10.1016/S1389-5567(03)00026-1
- [17] H. TAN, R. SANTBERGEN, G. YANG, A. SMETS, and M. ZEMAN “Combined Optical and Electrical Design of Plasmonic Back Reflector for High-Efficiency Thin-Film Silicon Solar Cells” *IEEE Journal of Photovoltaics* **3**: (2013), 53–58 DOI: 10.1109/JPHOTOV.2012.2220528
- [18] J. LANG and J. HUOT “A new approach to the processing of metal hydrides” *Journal of Alloys and Compounds* **509**: (2011), L18–L22 DOI: 10.1016/j.jallcom.2010.09.173
- [19] A. ZALUSKA, L. ZALUSKI, and J. STRÖM-OLSEN “Structure, catalysis and atomic reactions on the nano-scale: a systematic approach to metal hydrides for hydrogen storage” *Applied Physics A Materials Science & Processing* **72**: (2001), 157–165 DOI: 10.1007/s003390100783
- [20] F. KRUIS, H. FISSAN, and A. PELED “Synthesis of nanoparticles in the gas phase for electronic, optical and magnetic applications—a review” *Journal of Aerosol Science* **29**: (1998), 511–535 DOI: 10.1016/S0021-8502(97)10032-5
- [21] G. BISKOS, V. A. VONS, C. U. YURTERI, and A. SCHMIDT-OTT “Generation and Sizing of Particles for Aerosol-Based Nanotechnology” *KONA Powder and Particle Journal* **30**: (2008), 13–35
- [22] S. SCHWYN, E. GARWIN, and A. SCHMIDT-OTT “Aerosol generation by spark discharge” *Journal of Aerosol Science* **19**: (1988), 639–642 DOI: 10.1016/0021-8502(88)90215-7
- [23] H. HERTZ “Ueber einen Einfluss des ultravioletten Lichtes auf die elektrische Entladung” *Annalen der Physik und Chemie* **267**: (1887), 983–1000 DOI: 10.1002/andp.18872670827

- [24] A. FRIDMAN *Plasma Chemistry* 1st ed. Cambridge University Press, 2008 1022 pp.
- [25] E. M. BAZELYAN and Y. P. RAIZER *Spark Discharge* 1st ed. CRC-Press, 1998
- [26] F. BRUCE “A review of spark discharge phenomena” *Journal of the British Institution of Radio Engineers* **11**: (1951), 121–135 DOI: 10.1049/jbire.1951.0026
- [27] J. M. MEEK “A Theory of Spark Discharge” *Physical Review* **57**: (1940), 722 DOI: 10.1103/PhysRev.57.722
- [28] J. W. FLOWERS “The Channel of the Spark Discharge” *Physical Review* **64**: (1943), 225 DOI: 10.1103/PhysRev.64.225
- [29] H. MARTINEN and H. THOLL “Untersuchung der Temperatur un der Expansion von Funkenkanälen in H<sub>2</sub> bei variabele Energiezufuhr” German *Zeitschrift für Naturforschung* **25a**: (1970), 430–439
- [30] V. VONS “Spark Discharge Generated Nanoparticles for Hydrogen Storage Applications” ISBN: 978-90-55335-308-0 Delft University of Technology, 2010
- [31] R. REINMANN and M. AKRAM “Temporal investigation of a fast spark discharge in chemically inert gases” *Journal of Physics D: Applied Physics* **30**: (1997), 1125
- [32] J. H. BYEON and J.-W. KIM “Production of carbonaceous nanostructures from a silver-carbon ambient spark” *Applied Physics Letters* **96**: (2010), 153102 DOI: 10.1063/1.3396188
- [33] N. T. JENKINS and T. W. EAGAR “Submicron particle chemistry: Vapor condensation analogous to liquid solidification” *JOM* **55**: (2003), 44–47 DOI: 10.1007/s11837-003-0138-3
- [34] T. V. PFEIFFER, J. FENG, and A. SCHMIDT-OTT “New developments in spark production of nanoparticles” *Advanced Powder Technology* **25**: (2014), 56–70 DOI: 10.1016/j.ap.t.2013.12.005
- [35] A. MAISSER, K. BARMPOUNIS, M. B. ATTOUI, G. BISKOS, and A. SCHMIDT-OTT “Generation of sub-Nanometer Atomic Clusters in the Aerosol Phase using Spark Discharge Generation (SDG)” in: European Aerosol conference Prague, Czech Republic, 2013, 531
- [36] M. D. BARANKIN, K. BARMPOUNIS, G. BISKOS, T. BOSBOOM, A. MAISSER, T. V. PFEIFFER, and A. SCHMIDT-OTT “The Spark Generator as a Simple Source of sub-Nanometer Atomic Clusters” in: European Aerosol Conference Grana, 2012, 1399
- [37] D. E. BERGERON, P. J. ROACH, A. W. CASTLEMAN, N. O. JONES, and S. N. KHANNA “Al Cluster Superatoms as Halogens in Polyhalides and as Alkaline Earths in Iodide Salts” en *Science* **307**: (2005) PMID: 15653497, 231–235 DOI: 10.1126/science.1105820
- [38] J. FENG, A. MAISSER, T. PFEIFFER, G. BISKOS, and A. SCHMIDT-OTT “Size Controlled Synthesis of Spherical Nanoparticles by Spark Discharge” in: European Aerosol Conference Prague, 2013, 222

- [39] A. WEBER, U. BALTENSPERGER, H. GÄGGLER, and A. SCHMIDT-OTT “In situ characterization and structure modification of agglomerated aerosol particles” *Journal of Aerosol Science* **27**: (1996), 915–929 DOI: 10.1016/0021-8502(96)00013-4
- [40] S. KALA, M. ROUENHOFF, R. THEISSMANN, and F. E. KRUIS “Synthesis and Film Formation of Monodisperse Nanoparticles and Nanoparticle pairs” in: *Nanoparticles from the Gasphase: Formation, Structure, Properties* ed. by A. LORKE, M. WINTERER, R. SCHMECHEL, and C. SCHULZ NanoScience and Technology Springer, 2012, 99–119
- [41] V. VONS, L. DE SMET, D. MUNAO, A. EVIRGEN, E. KELDER, and A. SCHMIDT-OTT “Silicon nanoparticles produced by spark discharge” *Journal of Nanoparticle Research* **13**: (2011), 4867–4879 DOI: 10.1007/s11051-011-0466-0
- [42] N. S. TABRIZI, M. ULLMANN, V. A. VONS, U. LAFONT, and A. SCHMIDT-OTT “Generation of nanoparticles by spark discharge” *Journal of Nanoparticle Research* **11**: (2009), 315–332 DOI: 10.1007/s11051-008-9407-y
- [43] N. S. TABRIZI, Q. XU, N. M. VAN DER PERS, U. LAFONT, and A. SCHMIDT-OTT “Synthesis of mixed metallic nanoparticles by spark discharge” *Journal of Nanoparticle Research* **11**: (2008), 1209–1218 DOI: 10.1007/s11051-008-9568-8
- [44] C. ROTH, G. A. FERRON, E. KARG, B. LENTNER, G. SCHUMANN, S. TAKENAKA, and J. HEYDER “Generation of Ultrafine Particles by Spark Discharging” *Aerosol Science and Technology* **38**: (2004), 228 DOI: 10.1080/02786820490247632
- [45] R. L. WATTERS, J. R. DEVOE, F. H. SHEN, J. A. SMALL, and R. B. MARINENKO “Characteristics of aerosols produced by the spark discharge” *Analytical Chemistry* **61**: (1989), 1826–1833 DOI: 10.1021/ac00192a009
- [46] D. E. EVANS, R. M. HARRISON, and J. G. AYRES “The Generation and Characterization of Metallic and Mixed Element Aerosols for Human Challenge Studies” *Aerosol Science and Technology* **37**: (2003), 975 DOI: 10.1080/02786820300897
- [47] U. LAFONT, L. SIMONIN, N. S. TABRIZI, A. SCHMIDT-OTT, and E. M. KELDER “Synthesis of Nanoparticles of Cu, Sb, Sn, SnSb and Cu<sub>2</sub>Sb by Densification and Atomization Process” *Journal of Nanoscience and Nanotechnology* **9**: (2009), 2546–2552 DOI: 10.1166/jnn.2009.dk13
- [48] N. S. TABRIZI, Q. XU, N. M. PERS, and A. SCHMIDT-OTT “Generation of mixed metallic nanoparticles from immiscible metals by spark discharge” *Journal of Nanoparticle Research* **12**: (2010), 247–259 DOI: 10.1007/s11051-009-9603-4
- [49] J. H. BYEON, J. H. PARK, and J. HWANG “Spark generation of monometallic and bimetallic aerosol nanoparticles” *Journal of Aerosol Science* **39**: (2008), 888–896 DOI: 10.1016/j.jaerosci.2008.05.006
- [50] D. Z. PAI “Nanomaterials synthesis at atmospheric pressure using nanosecond discharges” *Journal of Physics D: Applied Physics* **44**: (2011), 174024 DOI: 10.1088/0022-3727/44/17/174024

- [51] Z. LIU, S. C. KIM, J. WANG, W. G. SHIN, H. FISSAN, and D. Y. H. PUI “Measurement of Metal Nanoparticle Agglomerates Generated by Spark Discharge Using the Universal Nanoparticle Analyzer (UNPA)” *Aerosol Science and Technology* **46**: (2011), 333–346 DOI: 10.1080/02786826.2011.626002
- [52] J. M. MÄKELÄ, P. AALTO, B. Z. GORBUNOV, and P. KORHONEN “Size distributions from aerosol spark generator” *Journal of Aerosol Science* **23**: (1992), 233–236 DOI: 10.1016/0021-8502(92)90392-9
- [53] A. E. BERKOWITZ and J. L. WALTER “Spark erosion: A method for producing rapidly quenched fine powders” *Journal of Materials Research* **2**: (1987), 277–288 DOI: 10.1557/JMR.1987.0277
- [54] N. S. TABRIZI “Generation of Nanoparticles by Spark Discharge” Delft University of Technology, 2009
- [55] V. VONS, H. LEEGWATER, W. LEGERSTEE, S. EIJT, and A. SCHMIDT-OTT “Hydrogen storage properties of spark generated palladium nanoparticles” *International Journal of Hydrogen Energy* **35**: (2010), 5479–5489 DOI: 10.1016/j.ijhydene.2010.02.118
- [56] M. A. LIEBERMAN and A. J. LICHTENBERG *Principles of Plasma Discharges and Materials Processing*, 2nd Edition 2nd ed. Wiley-Interscience, 2005
- [57] L. CHRISTOPHOROU “Insulating gases” *Nuclear Instruments and Methods in Physics Research Section A: Accelerators, Spectrometers, Detectors and Associated Equipment* **268**: (1988), 424–433 DOI: 10.1016/0168-9002(88)90550-5
- [58] G. A. KACHICKAS and L. H. FISHER “Formative Time Lags of Uniform Field Breakdown in Argon” *Physical Review* **91**: (1953), 775–779 DOI: 10.1103/PhysRev.91.775
- [59] G. A. KACHICKAS and L. H. FISHER “Formative Time Lags of Uniform Field Breakdown in N<sub>2</sub>” *Physical Review* **88**: (1952), 878–883 DOI: 10.1103/PhysRev.88.878
- [60] D. MITLIN *Advance Technical Data sheet* 2004
- [61] C. PEINEKE and A. SCHMIDT-OTT “Production and deposition of well defined aerosol nanoparticles for studies of basic properties” en ISBN 978-90-9022872-3 Delft University of Technology, 2008
- [62] N. JIDENKO, M. PETTIT, and J. P. BORRA “Electrical characterization of microdischarges produced by dielectric barrier discharge in dry air at atmospheric pressure” *Journal of Physics D: Applied Physics* **39**: (2006), 281–293 DOI: 10.1088/0022-3727/39/2/008
- [63] J. HOU, N. JIDENKO, J.-P. BORRA, and A. P. WEBER “Production of Metal Nanoparticles in Asymmetrical Dielectric Barrier Discharge-Plasma Reactor at Atmospheric Pressure” en *Chemie Ingenieur Technik* **83**: (2011), 2161–2169 DOI: 10.1002/cite.201100057
- [64] E. BOURGEOIS, N. JIDENKO, and J.-P. BORRA “Nano-particles production by dielectric barrier discharge” in: International Aerosol Conference Helsinki, 2010

- [65] M. STEIN, D. KIESLER, and F. E. KRUIS “Effect of carrier gas composition on transferred arc metal nanoparticle synthesis” en *Journal of Nanoparticle Research* **15**: (2013), 1–14 DOI: 10.1007/s11051-012-1400-9
- [66] W. C. HINDS *Aerosol Technology: Properties, Behavior, and Measurement of Airborne Particles* 2nd ed. Wiley-Interscience, 1999
- [67] R. K. SINNOTT *Chemical Engineering Design* eng ed. by J. M. COULSON and J. F. RICHARDSON 3rd ed. **6** Coulson & Richardson’s Chemical Engineering Oxford: Butterworth-Heinemann, 1999
- [68] T. HAWA and M. R. ZACHARIAH “Coalescence kinetics of unequal sized nanoparticles” *Journal of Aerosol Science* **37**: (2006), 1–15 DOI: 10.1016/j.jaerosci.2005.02.007
- [69] E. HONTAÑÓN, J. M. PALOMARES, M. STEIN, X. GUO, R. ENGELN, H. NIRSCHL, and F. E. KRUIS “The transition from spark to arc discharge and its implications with respect to nanoparticle production” en *Journal of Nanoparticle Research* **15**: (2013), 1–19 DOI: 10.1007/s11051-013-1957-y
- [70] M. L. EGGERSDORFER and S. E. PRATSINIS “Restructuring of aggregates and their primary particle size distribution during sintering” en *AIChE Journal* **59**: (2013), 1118–1126 DOI: 10.1002/aic.14043
- [71] G. J. V. AMERONGEN “The Permeability of Different Rubbers to Gases and Its Relation to Diffusivity and Solubility” *Journal of Applied Physics* **17**: (1946), 972–985 DOI: 10.1063/1.1707667
- [72] H. A. ATWATER and A. POLMAN “Plasmonics for improved photovoltaic devices” *Nature Materials* **9**: (2010), 205–213 DOI: 10.1038/nmat2629
- [73] R. SANTBERGEN, H. TAN, T. PFEIFFER, X. LI, T. FRIJNTS, A. SMETS, A. SCHMIDT-OTT, and M. ZEMAN “Plasmonic Solar Cells with Embedded Silver Nanoparticles from Vapor Condensation” *MRS Online Proceedings Library* **1391**: (2012) mrsf11-1391-j06-07, pages DOI: 10.1557/opl.2012.691
- [74] V. E. FERRY, M. A. VERSCHUUREN, H. B. T. LI, E. VERHAGEN, R. J. WALTERS, R. E. I. SCHROPP, H. A. ATWATER, and A. POLMAN “Light trapping in ultrathin plasmonic solar cells” *Optics Express* **18**: (2010), A237–A245 DOI: 10.1364/OE.18.00A237
- [75] D. DERKACS, S. H. LIM, P. MATHEU, W. MAR, and E. T. YU “Improved performance of amorphous silicon solar cells via scattering from surface plasmon polaritons in nearby metallic nanoparticles” *Applied Physics Letters* **89**: (2006), 093103 DOI: 10.1063/1.2336629
- [76] S. HE, J. YAO, P. JIANG, D. SHI, H. ZHANG, S. XIE, S. PANG, and H. GAO “Formation of Silver Nanoparticles and Self-Assembled Two-Dimensional Ordered Superlattice” *Langmuir* **17**: (2001), 1571–1575 DOI: 10.1021/1a001239w
- [77] J. HARRA, J. MÄKITALO, R. SIKANEN, M. VIRKKI, G. GENTY, T. KOBAYASHI, M. KAURANEN, and J. M. MÄKELÄ “Size-controlled aerosol synthesis of silver nanoparticles for plasmonic materials” en *Journal of Nanoparticle Research* **14**: (2012), 1–10 DOI: 10.1007/s11051-012-0870-0

- [78] S. ZIHLMANN, F. LÜÖND, and J. K. SPIEGEL “Generation of heterogeneously nucleated, monodisperse silver nanoparticles” *arXiv:1401.7554 [cond-mat, physics:physics]* (2014)
- [79] K. KITAZAWA and R. L. COBLE “Chemical Diffusion in Polycrystalline Al<sub>2</sub>O<sub>3</sub> as Determined from Electrical Conductivity Measurements” en *Journal of the American Ceramic Society* **57**: (1974), 250–253 DOI: 10.1111/j.1151-2916.1974.tb10880.x
- [80] H. TAN, E. PSOMADAKI, O. ISABELLA, M. FISCHER, P. BABAL, R. VASUDEVAN, M. ZEMAN, and A. H. M. SMETS “Micro-textures for efficient light trapping and improved electrical performance in thin-film nanocrystalline silicon solar cells” *Applied Physics Letters* **103**: (2013), 173905 DOI: 10.1063/1.4826639
- [81] P. LAVEN *MiePlot: A computer program for scattering of light from a sphere using Mie theory & the Debye series* 2014 URL: <http://www.philiplaven.com/mieplot.htm>
- [82] C. F. BOHREN and D. R. HUFFMANN *Absorption and scattering of light by small particles* English New York: Wiley, 1983
- [83] J.-P. SCHÄFER “Implementierung und Anwendung analytischer und numerischer Verfahren zur Lösung der Maxwellgleichungen für die Untersuchung der Lichtausbreitung in biologischem Gewebe” Ulm University, 2011
- [84] P. B. JOHNSON and R. W. CHRISTY “Optical Constants of the Noble Metals” *Physical Review B* **6**: (1972), 4370–4379 DOI: 10.1103/PhysRevB.6.4370
- [85] J. M. BENNETT, J. L. STANFORD, and E. J. ASHLEY “Optical Constants of Silver Sulfide Tarnish Films” *Journal of the Optical Society of America* **60**: (1970), 224–231 DOI: 10.1364/JOSA.60.000224
- [86] C. A. SCHNEIDER, W. S. RASBAND, and K. W. ELICEIRI “NIH Image to ImageJ: 25 years of image analysis” en *Nature Methods* **9**: (2012), 671–675 DOI: 10.1038/nmeth.2089
- [87] C. HELSPER, W. MÖLTER, F. LÖFFLER, C. WADENPOHL, S. KAUFMANN, and G. WENNINGER “Investigations of a new aerosol generator for the production of carbon aggregate particles” *Atmospheric Environment. Part A. General Topics* **27**: (1993), 1271–1275 DOI: 10.1016/0960-1686(93)90254-V
- [88] T. J. KRINKE, K. DEPERT, M. H. MAGNUSSON, F. SCHMIDT, and H. FISSAN “Microscopic aspects of the deposition of nanoparticles from the gas phase” *Journal of Aerosol Science* **33**: (2002), 1341–1359 DOI: 10.1016/S0021-8502(02)00074-5
- [89] A. WIEDENSOHLER “An approximation of the bipolar charge distribution for particles in the submicron size range” *Journal of Aerosol Science* **19**: (1988), 387–389 DOI: 10.1016/0021-8502(88)90278-9
- [90] H. E. BENNETT “Formation and Growth of Tarnish on Evaporated Silver Films” *Journal of Applied Physics* **40**: (1969), 3351 DOI: 10.1063/1.1658187
- [91] J. P. FRANNEY, G. W. KAMMLOTT, and T. E. GRAEDEL “The corrosion of silver by atmospheric sulfurous gases” *Corrosion Science* **25**: (1985), 133–143 DOI: 10.1016/0010-938X(85)90104-0

- [92] S. BOUQUET, C. BODIN, and C. FIAUD “Influence relative des composés soufrés et chlorés sur le ternissement de l’argent en milieu atmosphérique” *Français Comptes rendus de l’Académie des sciences. II: Mécanique, physique, chimie, sciences de l’univers, sciences de la terre* **316**: (1993), 459–464
- [93] J. KANGASLUOMA, H. JUNNINEN, K. LEHTIPALO, J. MIKKILÄ, J. VANHANEN, M. ATTOUI, M. SIPILÄ, D. WORSNOP, M. KULMALA, and T. PETÄJÄ “Remarks on Ion Generation for CPC Detection Efficiency Studies in Sub-3-nm Size Range” *Aerosol Science and Technology* **47**: (2013), 556–563 DOI: 10.1080/02786826.2013.773393
- [94] “Production of high purity alumina” US4634581 D. M. BLAKE, E. L. CAMBRIDGE, R. O. LOUTFY, and J. C. WITHERS 1987
- [95] H. SCHEIBEL and J. PORSTENDÖRFER “Generation of monodisperse Ag- and NaCl-aerosols with particle diameters between 2 and 300 nm” *Journal of Aerosol Science* **14**: (1983), 113–126 DOI: 10.1016/0021-8502(83)90035-6
- [96] C. PEINEKE, M. ATTOUI, and A. SCHMIDT-OTT “Using a glowing wire generator for production of charged, uniformly sized nanoparticles at high concentrations” *Journal of Aerosol Science* **37**: (2006), 1651–1661 DOI: 10.1016/j.jaerosci.2006.06.006
- [97] M. DALE and S. M. BENSON “Energy Balance of the Global Photovoltaic (PV) Industry - Is the PV Industry a Net Electricity Producer?” *Environmental Science & Technology* **47**: (2013), 3482–3489 DOI: 10.1021/es3038824
- [98] E. HONTAÑÓN and F. E. KRUIS “A Differential Mobility Analyzer (DMA) for Size Selection of Nanoparticles at High Flow Rates” *Aerosol Science and Technology* **43**: (2009), 25–37
- [99] M. D. MCMAHON, R. LOPEZ, H. M. MEYER III, L. C. FELDMAN, and R. F. HAGLUND JR. “Rapid tarnishing of silver nanoparticles in ambient laboratory air” en *Applied Physics B* **80**: (2005), 915–921 DOI: 10.1007/s00340-005-1793-6
- [100] H. B. T. LI, R. H. FRANKEN, J. K. RATH, and R. E. I. SCHROPP “Structural defects caused by a rough substrate and their influence on the performance of hydrogenated nano-crystalline silicon n-i-p solar cells” *Solar Energy Materials and Solar Cells* **93**: (2009), 338–349 DOI: 10.1016/j.solmat.2008.11.013
- [101] A. ANASTASOPOUL “Kinetic and Thermodynamic Aspects of Mg and Mg-Ti hydride Nanomaterials” Delft University of Technology, 2014
- [102] J. HUOT, D. RAVNSBÆK, J. ZHANG, F. CUEVAS, M. LATROCHE, and T. JENSEN “Mechanochemical synthesis of hydrogen storage materials” *Progress in Materials Science* **58**: (2013), 30–75 DOI: 10.1016/j.pmatsci.2012.07.001
- [103] B. MOLINAS, A. GHILARDUCCI, M. MELNICHUK, H. CORSO, H. PERETTI, F. AGRESTI, A. BIANCHIN, S. LO RUSSO, A. MADDALENA, and G. PRINCIPI “Scaled-up production of a promising Mg-based hydride for hydrogen storage” *International Journal of Hydrogen Energy* **34**: (2009), 4597–4601 DOI: 10.1016/j.ijhydene.2008.09.076

- [104] D. A. SHEPPARD, M. PASKEVICIUS, and C. E. BUCKLEY “The Mechanochemical synthesis of magnesium hydride nanoparticles” *Journal of Alloys and Compounds* **492**: (2010), L72–L74 DOI: 10.1016/j.jallcom.2009.12.006
- [105] B. BOGDANOVIC “Magnesium hydride: A homogeneous-catalysed synthesis and its use in hydrogen storage” *International Journal of Hydrogen Energy* **9**: (1984), 937–941 DOI: 10.1016/0360-3199(84)90159-9
- [106] E. J. SETIJADI, C. BOYER, and K.-F. AGUEY-ZINSOU “Remarkable hydrogen storage properties for nanocrystalline MgH<sub>2</sub> synthesised by the hydrogenolysis of Grignard reagents” en *Physical Chemistry Chemical Physics* **14**: (2012), 11386–11397 DOI: 10.1039/C2CP41140G
- [107] S. HARDER, J. SPIELMANN, J. INTEMANN, and H. BANDMANN “Hydrogen Storage in Magnesium Hydride: The Molecular Approach” en *Angewandte Chemie International Edition* **50**: (2011), 4156–4160 DOI: 10.1002/anie.201101153
- [108] K.-J. JEON, H. R. MOON, A. M. RUMINSKI, B. JIANG, C. KISIELOWSKI, R. BARDHAN, and J. J. URBAN “Air-stable magnesium nanocomposites provide rapid and high-capacity hydrogen storage without using heavy-metal catalysts” en *Nature Materials* **10**: (2011), 286–290 DOI: 10.1038/nmat2978
- [109] S. ZHANG, A. F. GROSS, S. L. V. ATTA, M. LOPEZ, P. LIU, C. C. AHN, J. J. VAJO, and C. M. JENSEN “The synthesis and hydrogen storage properties of a MgH<sub>2</sub> incorporated carbon aerogel scaffold” en *Nanotechnology* **20**: (2009), 204027 DOI: 10.1088/0957-4484/20/20/204027
- [110] C. ZLOTEA, C. CHEVALIER-CÉSAR, E. LÉONEL, E. LEROY, F. CUEVAS, P. DIBANDJO, C. VIX-GUTERL, T. MARTENS, and M. LATOCHE “Synthesis of small metallic Mg-based nanoparticles confined in porous carbon materials for hydrogen sorption” en *Faraday Discussions* **151**: (2011), 117–131 DOI: 10.1039/C0FD00016G
- [111] P. E. D. JONGH, R. W. P. WAGEMANS, T. M. EGGENHUISEN, B. S. DAUVILLIER, P. B. RADSTAKE, J. D. MEELDIJK, J. W. GEUS, and K. P. D. JONG “The Preparation of Carbon-Supported Magnesium Nanoparticles using Melt Infiltration” *Chemistry of Materials* **19**: (2007), 6052–6057 DOI: 10.1021/cm702205v
- [112] A. F. GROSS, C. C. AHN, S. L. V. ATTA, P. LIU, and J. J. VAJO “Fabrication and hydrogen sorption behaviour of nanoparticulate MgH<sub>2</sub> incorporated in a porous carbon host” en *Nanotechnology* **20**: (2009), 204005 DOI: 10.1088/0957-4484/20/20/204005
- [113] L. PASQUINI, E. CALLINI, M. BRIGHI, F. BOSCHERINI, A. MONTONE, T. R. JENSEN, C. MAURIZIO, M. VITTORI ANTISARI, and E. BONETTI “Magnesium nanoparticles with transition metal decoration for hydrogen storage” *Journal of Nanoparticle Research* **13**: (2011), 5727–5737 DOI: 10.1007/s11051-011-0509-6
- [114] C. ZHU, H. HAYASHI, I. SAITA, and T. AKIYAMA “Direct synthesis of MgH<sub>2</sub> nanofibers at different hydrogen pressures” *International Journal of Hydrogen Energy* **34**: (2009), 7283–7290 DOI: 10.1016/j.ijhydene.2009.06.080

- [115] C. PLATZER-BJÖRKMAN, T. MONGSTAD, J. MÆHLEN, A. BALDI, S. KARAZHANOV, and A. HOLT “Deposition of magnesium hydride thin films using radio frequency reactive sputtering” *Thin Solid Films* **519**: (2011), 5949–5954 DOI: 10.1016/j.tsf.2011.03.033
- [116] H. SHAO, Y. WANG, H. XU, and X. LI “Hydrogen storage properties of magnesium ultrafine particles prepared by hydrogen plasma-metal reaction” *Materials Science and Engineering: B* **110**: (2004), 221–226 DOI: 10.1016/j.mseb.2004.03.013
- [117] J. F. STAMPFER, C. E. HOLLEY, and J. F. SUTTLE “The Magnesium-Hydrogen System” *Journal of the American Chemical Society* **82**: (1960), 3504–3508 DOI: 10.1021/ja01499a006
- [118] M. GUNDERSEN and S. GUHA “Formation of metastable species in hydrogen thyratrons” *Journal of Applied Physics* **53**: (1982), 1190–1192 DOI: doi:10.1063/1.330569
- [119] Z. MACHALA, E. MARODE, C. O. LAUX, and C. H. KRUGER “DC Glow Discharges in Atmospheric Pressure Air” *Journal of Advanced Oxidation Technologies* **7**: (2004), 133–137
- [120] A. FRIDMAN, A. CHIROKOV, and A. GUTSOL “Non-thermal atmospheric pressure discharges” *Journal of Physics D: Applied Physics* **38**: (2005), R1–R24 DOI: 10.1088/0022-3727/38/2/R01
- [121] V. I. MIKHEEVA and N. N. MAL’TSEVA “Infrared absorption spectra of some simple hydrides” *Journal of Structural Chemistry* **4**: (1964), 643–646 DOI: 10.1007/BF00747652
- [122] J. STOBER, B. SCHLEICHER, and H. BURTSCHER “Bipolar Diffusion Charging of Particles in Noble Gases” *Aerosol Science and Technology* **14**: (1991), 66–73 DOI: 10.1080/02786829108959471
- [123] A. ANASTASOPOL, T. V. PFEIFFER, A. SCHMIDT-OTT, F. M. MULDER, and S. W. H. EIJT “Fractal disperse hydrogen sorption kinetics in spark discharge generated Mg/NbO<sub>x</sub> and Mg/Pd nanocomposites” *Applied Physics Letters* **99**: (2011), 194103 DOI: 10.1063/1.3659315
- [124] M. TANAKA and T. WATANABE “Vaporization mechanism from Sn–Ag mixture by Ar–H<sub>2</sub> Arc for nanoparticle preparation” *Thin Solid Films* **516**: (2008), 6645–6649 DOI: 10.1016/j.tsf.2007.11.096
- [125] H. FÖRSTER, C. WOLFRUM, and W. PEUKERT “Experimental study of metal nanoparticle synthesis by an arc evaporation/condensation process” *Journal of Nanoparticle Research* **14**: (2012), 1–16 DOI: 10.1007/s11051-012-0926-1
- [126] T. WATANABE, H. ITOH, and Y. ISHII “Preparation of ultrafine particles of silicon base intermetallic compound by arc plasma method” *Thin Solid Films* **390**: (2001), 44–50 DOI: 10.1016/S0040-6090(01)00923-3
- [127] J. NOMA, Y. UESHIMA, T. FUKUI, H. ABE, K. YAMAMOTO, M. TANAKA, and M. NAITO “Generation of Fe nanoparticles by He-H<sub>2</sub> arc plasma” *Quarterly Journal of the Japan Welding Society* **29**: (2011), 27s–30s DOI: 10.2207/qjws.29.27s

- [128] J. NOMA, H. ABE, M. NAITO, K. YAMAMOTO, S. TASHIRO, and M. TANAKA “Influence of Hydrogen Induced Thermal Pinch on Nanoparticle Formation in Arc Plasma” *Quarterly Journal of the Japan Welding Society* **27**: (2009), 13s–16s
- [129] T. LIU, Y. ZHANG, and X. LI “Preparations and characteristics of Ti hydride and Mg ultrafine particles by hydrogen plasma–metal reaction” *Scripta Materialia* **48**: (2003), 397–402 DOI: 10.1016/S1359-6462(02)00444-X
- [130] T. LIU, H. SHEN, Y. LIU, L. XIE, J. QU, H. SHAO, and X. LI “Scaled-up synthesis of nanostructured Mg-based compounds and their hydrogen storage properties” *Journal of Power Sources* **227**: (2013), 86–93 DOI: 10.1016/j.jpowsour.2012.11.011
- [131] F. D. MANCHESTER and J. M. PITRE “The Ce-H (Cerium-Hydrogen) system” en *Journal of Phase Equilibria* **18**: (1997), 63–77 DOI: 10.1007/BF02646759
- [132] F. D. MANCHESTER and J. M. PITRE “The H-Sm system (hydrogen-samarium)” en *Journal of Phase Equilibria* **17**: (1996), 432–441 DOI: 10.1007/BF02667636
- [133] W.-E. WANG “Thermodynamic evaluation of the titanium-hydrogen system” *Journal of Alloys and Compounds* **238**: (1996), 6–12 DOI: 10.1016/0925-8388(96)02264-5
- [134] G. BARKHORDARIAN, T. KLASSEN, and R. BORMANN “Effect of Nb<sub>2</sub>O<sub>5</sub> content on hydrogen reaction kinetics of Mg” *Journal of Alloys and Compounds* **364**: (2004), 242–246 DOI: 10.1016/S0925-8388(03)00530-9
- [135] H. G. SCHIMMEL, J. HUOT, L. C. CHAPON, F. D. TICHELAAR, and F. M. MULDER “Hydrogen Cycling of Niobium and Vanadium Catalyzed Nanostructured Magnesium” *Journal of the American Chemical Society* **127**: (2005), 14348–14354 DOI: 10.1021/ja051508a
- [136] G. BARKHORDARIAN, T. KLASSEN, and R. BORMANN “Catalytic Mechanism of Transition-Metal Compounds on Mg Hydrogen Sorption Reaction” *The Journal of Physical Chemistry B* **110**: (2006), 11020–11024 DOI: 10.1021/jp0541563
- [137] F. DOLCI, M. DI CHIO, M. BARICCO, and E. GIAMELLO “The interaction of hydrogen with oxidic promoters of hydrogen storage in magnesium hydride” *Materials Research Bulletin* **44**: (2009), 194–197 DOI: 10.1016/j.materresbull.2008.03.006
- [138] Z. WRONSKI, G. CARPENTER, T. CZUJKO, and R. VARIN “A new nanonickel catalyst for hydrogen storage in solid-state magnesium hydrides” *International Journal of Hydrogen Energy* **36**: (2011), 1159–1166 DOI: 10.1016/j.ijhydene.2010.06.089
- [139] O. FRIEDRICHS, J. SÁNCHEZ-LÓPEZ, C. LÓPEZ-CARTES, T. KLASSEN, R. BORMANN, and A. FERNÁNDEZ “Nb<sub>2</sub>O<sub>5</sub> ”pathway effect” on hydrogen sorption in Mg” *Journal of Physical Chemistry B* **110**: (2006), 7845–7850
- [140] G. FRIEDLMEIER and M. GROLL “Experimental analysis and modelling of the hydriding kinetics of Ni-doped and pure Mg” *Journal of Alloys and Compounds* **253–254**: (1997), 550–555 DOI: 10.1016/S0925-8388(96)03003-4

- [141] X. TAN, B. ZAHIRI, C. M. HOLT, A. KUBIS, and D. MITLIN “A TEM based study of the microstructure during room temperature and low temperature hydrogen storage cycling in MgH<sub>2</sub> promoted by Nb–V” *Acta Materialia* **60**: (2012), 5646–5661 DOI: 10.1016/j.actamat.2012.06.009
- [142] “Capacitor Powder” WO/2001/099130 K. REICHERT and C. SCHNITTER 2001
- [143] O. FRIEDRICHS, F. AGUEY-ZINSOU, J. A. FERNÁNDEZ, J. SÁNCHEZ-LÓPEZ, A. JUSTO, T. KLASSEN, R. BORMANN, and A. FERNÁNDEZ “MgH<sub>2</sub> with Nb<sub>2</sub>O<sub>5</sub> as additive, for hydrogen storage: Chemical, structural and kinetic behavior with heating” *Acta Materialia* **54**: (2006), 105–110 DOI: 10.1016/j.actamat.2005.08.024
- [144] M. GRUNDNER and J. HALBRITTER “XPS and AES studies on oxide growth and oxide coatings on niobium” *Journal of Applied Physics* **51**: (1980), 397 DOI: 10.1063/1.327386
- [145] F. L. JONES “Electrode Erosion by Spark Discharges” *British Journal of Applied Physics* **1**: (1950), 60–65 DOI: 10.1088/0508-3443/1/3/302
- [146] J. HALBRITTER “On the oxidation and on the superconductivity of niobium” *Applied Physics A Solids and Surfaces* **43**: (1987), 1–28 DOI: 10.1007/BF00615201
- [147] M. L. EGGERSDORFER, D. KADAU, H. J. HERRMANN, and S. E. PRATSINIS “Multiparticle Sintering Dynamics: From Fractal-Like Aggregates to Compact Structures” *Langmuir* **27**: (2011), 6358–6367 DOI: 10.1021/1a200546g
- [148] T. A. EGERTON “The Modification of Fine Powders by Inorganic Coatings” *KONA Powder and Particle Journal* **16**: (1998), 46–59
- [149] Z. TURGUT, N. T. NUHFER, H. R. PIEHLER, and M. E. MCHENRY “Magnetic properties and microstructural observations of oxide coated FeCo nanocrystals before and after compaction” *Journal of Applied Physics* **85**: (1999), 4406–4408 DOI: 10.1063/1.369799
- [150] J. M. PIETRYGA, D. J. WERDER, D. J. WILLIAMS, J. L. CASSON, R. D. SCHALLER, V. I. KLIMOV, and J. A. HOLLINGSWORTH “Utilizing the Lability of Lead Selenide to Produce Heterostructured Nanocrystals with Bright, Stable Infrared Emission” *Journal of the American Chemical Society* **130**: (2008), 4879–4885 DOI: 10.1021/ja710437r
- [151] D. E. GHEORGHE, L. CUI, C. KARMONIK, A. BRAZDEIKIS, J. M. PENALOZA, J. K. YOUNG, R. A. DREZEK, and M. BIKRAM “Gold-silver alloy nanoshells: a new candidate for nanotherapeutics and diagnostics” en *Nanoscale Research Letters* **6**: (2011) PMID: 21995302, 554 DOI: 10.1186/1556-276X-6-554
- [152] H. BAO, T. BIHR, A.-S. SMITH, and R. N. K. TAYLOR “Facile colloidal coating of polystyrene nanospheres with tunable gold dendritic patches” en *Nanoscale* (2013) DOI: 10.1039/C3NR04016J
- [153] A. TELEKI, B. BUESSER, M. C. HEINE, F. KRUMEICH, M. K. AKHTAR, and S. E. PRATSINIS “Role of Gas – Aerosol Mixing during in Situ Coating of Flame-Made Titania Particles” *Industrial & Engineering Chemistry Research* **48**: (2009), 85–92 DOI: 10.1021/ie800226d
- [154] J. R. SCHEFFE, A. FRANCÉS, D. M. KING, X. LIANG, B. A. BRANCH, A. S. CAVANAGH, S. M. GEORGE, and A. W. WEIMER “Atomic layer deposition

- of iron(III) oxide on zirconia nanoparticles in a fluidized bed reactor using ferrocene and oxygen” *Thin Solid Films* **517**: (2009), 1874–1879 DOI: 10.1016/j.tsf.2008.09.086
- [155] A. BINDER and M. SEIPENBUSCH “Stabilization of supported Pd particles by the application of oxide coatings” *Applied Catalysis A: General* **396**: (2011), 1–7 DOI: 10.1016/j.apcata.2010.12.030
- [156] Z. J. LIU, Z. Y. YUAN, W. ZHOU, Z. XU, and L. M. PENG “Controlled Synthesis of Carbon-Encapsulated Co Nanoparticles by CVD” en *Chemical Vapor Deposition* **7**: (2001), 248–251 DOI: 10.1002/1521-3862(200111)7:6<248::AID-CVDE248>3.0.CO;2-M
- [157] H. FÖRSTER and W. PEUKERT “In-situ synthesis and functionalisation of metal nanoparticles in a spark discharge process” in: European Aerosol Conference Helsinki, Finland, 2010, 1234
- [158] M. N. A. KARLSSON, K. DEPERT, M. H. MAGNUSSON, L. S. KARLSSON, and J.-O. MALM “Size- and Composition-Controlled Au–Ga Aerosol Nanoparticles” *Aerosol Science and Technology* **38**: (2004), 948–954 DOI: 10.1080/027868290511254
- [159] A. LÄHDE, J. RAULA, and E. I. KAUPPINEN “Combined synthesis and in situ coating of nanoparticles in the gas phase” en *Journal of Nanoparticle Research* **10**: (2008), 121–130 DOI: 10.1007/s11051-008-9399-7
- [160] L. ZHANG, M. RANADE, and J. GENTRY “Formation of organic coating on ultrafine silver particles using a gas-phase process” *English Journal of Aerosol Science* **35**: (2004), 457–471 DOI: 10.1016/j.jaerosci.2003.10.009
- [161] A. BOIES, P. LEI, S. CALDER, W. G. SHIN, and S. GIRSHICK “Hot-Wire Synthesis of Gold Nanoparticles” *Aerosol Science and Technology* **45**: (2011), 654–663 DOI: 10.1080/02786826.2010.551145
- [162] S. FRIEDLANDER, W. KOCH, and H. MAIN “Scavenging of a coagulating fine aerosol by a coarse particle mode” *Journal of Aerosol Science* **22**: (1991), 1–8 DOI: 10.1016/0021-8502(91)90088-Y
- [163] S. JAIN, G. P. FOTOU, and T. T. KODAS “A Theoretical Study on Gas-Phase Coating of Aerosol Particles” *Journal of Colloid and Interface Science* **185**: (1997), 26–38 DOI: 10.1006/jcis.1996.4558
- [164] B. BUESSER and S. PRATSINIS “Design of aerosol particle coating: Thickness, texture and efficiency” *English Chemical Engineering Science* **65**: (2010), 5471–5481 DOI: 10.1016/j.ces.2010.07.011
- [165] H. BRUNE “Microscopic view of epitaxial metal growth: nucleation and aggregation” *Surface Science Reports* **31**: (1998), 125–229 DOI: 10.1016/S0167-5729(99)80001-6
- [166] L. VITOS, A. RUBAN, H. SKRIVER, and J. KOLLÁR “The surface energy of metals” *Surface Science* **411**: (1998), 186–202 DOI: 10.1016/S0039-6028(98)00363-X
- [167] J. HAYOZ, T. PILLO, R. FASEL, L. SCHLAPBACH, and P. AEBI “Experimental evidence for kinetically determined intermixed Volmer-Weber growth in thin-film deposition of Au on Ag(110)” *Physical Review B* **59**: (1999), 15975–15989 DOI: 10.1103/PhysRevB.59.15975

- [168] A. EL-GENDY, E. IBRAHIM, V. KHAVRUS, Y. KRUPSKAYA, S. HAMPEL, A. LEONHARDT, B. BÜCHNER, and R. KLINGELER “The synthesis of carbon coated Fe, Co and Ni nanoparticles and an examination of their magnetic properties” *Carbon* **47**: (2009), 2821–2828 DOI: 10.1016/j.carbon.2009.06.025
- [169] J. H. BYEON, J. H. PARK, K. Y. YOON, and J. HWANG “Ambient spark generation to synthesize carbon-encapsulated metal nanoparticles in continuous aerosol manner” en *Nanoscale* **1**: (2009), 339–343 DOI: 10.1039/B9NR00058E
- [170] P. BUFFAT and J.-P. BOREL “Size effect on the melting temperature of gold particles” *Physical Review A* **13**: (1976), 2287 DOI: 10.1103/PhysRevA.13.2287
- [171] T. CASTRO, R. REIFENBERGER, E. CHOI, and R. P. ANDRES “Size-dependent melting temperature of individual nanometer-sized metallic clusters” *Physical Review B* **42**: (1990), 8548 DOI: 10.1103/PhysRevB.42.8548
- [172] G. ALLEN, R. BAYLES, W. GILE, and W. JESSER “Small particle melting of pure metals” *Thin Solid Films* **144**: (1986), 297–308 DOI: 10.1016/0040-6090(86)90422-0
- [173] B. DAHNEKE “Simple kinetic theory of Brownian diffusion in vapors and aerosols” English in: *Theory of dispersed multiphase flow* ed. by R. E. MEYER New York: Academic Press, 1983, 97–133
- [174] T. M. TRZECIAK “Brownian coagulation at high particle concentrations” English ISBN: 978-94-6191-251-0 Delft, the Netherlands: Delft, 2012
- [175] P. W. ATKINS “Physical chemistry” eng in: 6th ed. New York: Freeman, 1998
- [176] W. TYSON and W. MILLER “Surface free energies of solid metals: Estimation from liquid surface tension measurements” *Surface Science* **62**: (1977), 267–276 DOI: 10.1016/0039-6028(77)90442-3
- [177] G. LANG “Surface Tension of Liquid Elements” in: *Handbook of Chemistry and Physics* ed. by R. C. WEAST 54th ed. CRC Press, 1973, F-19
- [178] J. J. HOYT and M. ASTA “Atomistic computation of liquid diffusivity, solid-liquid interfacial free energy, and kinetic coefficient in Au and Ag” *Physical Review B* **65**: (2002), 214106 DOI: 10.1103/PhysRevB.65.214106
- [179] A. J. KINLOCH “Adhesion and adhesives: science and technology” eng in: London: Chapman and Hall, 1987
- [180] E. KNUTSON and K. WHITBY “Aerosol classification by electric mobility: apparatus, theory, and applications” *Journal of Aerosol Science* **6**: (1975), 443–451 DOI: 10.1016/0021-8502(75)90060-9
- [181] B. SCHLEICHER and S. FRIEDLANDER “Fabrication of aerogel-like structures by agglomeration of aerosol particles in an electric field” English *Journal of Colloid and Interface Science* **180**: (1996), 15–21 DOI: 10.1006/jcis.1996.0268
- [182] D. M. BASTIDAS, E. CANO, A. G. GONZÁLEZ, S. FAJARDO, R. LLERAS-PÉREZ, E. CAMPO-MONTERO, F. J. BELZUNCE-VARELA, and J. M. BASTIDAS “An XPS study of tarnishing of a gold mask from a pre-Columbian culture” *Corrosion Science* **50**: (2008), 1785–1788 DOI: 10.1016/j.corsci.2008.04.009

- [183] S. NIE and S. R. EMORY “Probing Single Molecules and Single Nanoparticles by Surface-Enhanced Raman Scattering” en *Science* **275**: (1997) PMID: 9027306, 1102–1106 DOI: 10.1126/science.275.5303.1102
- [184] B. MINCEVA-SUKAROVA, M. NAJDOSKI, I. GROZDANOV, and C. J. CHUN-NILALL “Raman spectra of thin solid films of some metal sulfides” *Journal of Molecular Structure* **410–411**: (1997), 267–270 DOI: 10.1016/S0022-2860(96)09713-X
- [185] N. IWASAKI, Y. SASAKI, and Y. NISHINA “Raman Study of Photoelectrochemical Oxidation of Silver Electrode in NaOH Solution” en *Journal of The Electrochemical Society* **135**: (1988), 2531–2534 DOI: 10.1149/1.2095370
- [186] G. L. BOTTFER and C. V. DAMSGARD “Second order Raman spectra of AgCl and AgBr crystals” *Solid State Communications* **9**: (1971), 1277–1280 DOI: 10.1016/0038-1098(71)90077-9
- [187] I. MARTINA, R. WIESINGER, and M. SCHREINER “Micro-Raman investigations of early stage silver corrosion products occurring in sulfur containing atmospheres” en *Journal of Raman Spectroscopy* **44**: (2013), 770–775 DOI: 10.1002/jrs.4276
- [188] B. ELLIS *Polymers: A Property Database (online)* CRC Press, 2013



# Samenvatting

Ondanks de duidelijke voordelen van duurzame energie vormen hernieuwbare bronnen slechts een klein deel van onze huidige energievoorziening. Fossiele brandstoffen zijn gemakkelijk en vooralsnog goedkoop, terwijl elke strategie voor duurzame energie haar eigen unieke set problemen en technische uitdagingen heeft. De kern van het probleem voor de meeste strategieën voor duurzame energie ligt in het vinden van het juiste materiaal. Vaak is een zeer specifieke combinatie van fysische, mechanische, optische, elektronische en/of magnetische eigenschappen nodig, en vaak is het zo dat dit ideale materiaal *nog* niet bestaat.

Als we accepteren dat we niet kunnen specialiseren, maar een aantal complementaire strategieën moeten adopteren, zien we dat het onaantrekkelijk is om te proberen door middel van trial-en-error voor iedere toepassing afzonderlijk het perfecte materiaal te vinden. Liever ontwikkelt de ingenieur het gewenste materiaal door bouwstenen met specifieke functies te combineren, om zo een materiaal met de juiste samenstelling van eigenschappen te ontwerpen. Zulk een aanpak is met name aantrekkelijk als de bouwstenen in ten minste één dimensie slechts nanometers groot is: Bij deze grootte, ten hoogste enkele tientallen atomen dik, spelen oppervlakteinteracties een dominante rol, wat vaak leidt tot een dramatische verschuiving in materiaaleigenschappen. De ingenieur is in dit ontwikkelingsproces gebaat bij flexibele methoden om haar bouwstenen, nanodeeltjes, in een verscheidenheid aan samenstellingen, vormen en grootten te produceren.

Vonkverdamming of vonkablatie is een veelzijdige methode voor het genereren van nanodeeltjes in een continu proces. Een vonk is een tijdelijk, hoog-energetisch elektrisch plasma met een temperatuur van  $2 \times 10^4$  tot  $6 \times 10^4$  K, en heeft een levensduur van enkele microseconden. Door de hoge temperatuur kan elk materiaal worden verdampt tot een damp van atomen. Gebruikelijk worden geleidende materialen, in het bijzonder metalen, toegepast. De korte levensduur leidt tot snelle afkoeling van de gevormde metaaldamp, re-

sulterend in nucleatie en groei van bijzonder kleine deeltjes. Afhankelijk van de omstandigheden waaronder de vonk wordt gedoofd, kan een aerosol met een deeltjesgrootte reikend van een enkel atoom tot enkele tientallen nanometers worden verkregen. Vonkverdamping is in principe een fysisch proces, waarbij een vaste stof omgeven door een inert gas met behulp van slechts elektrische energie wordt omgevormd tot nanodeeltjes. Als zodanig is het een inherent groen proces, waar geen oplosmiddelen of vervuilende bijproducten bij betrokken zijn.

In de aerosolfase kunnen deze nanodeeltjes op vele manieren gemanipuleerd en gemodificeerd worden. Men kan aerosoldeeltjes laten agglomereren, om grote, pluizige fractaal-achtige structuren te vormen, en die vervolgens weer omsmelten tot bolvormige deeltjes; hun oppervlakte modifieren, bijv. door chemische conversie of fysische depositie van een deklaagje van een ander materiaal; ze sorteren op basis van hun mobiliteit, een aan de deeltjesgrootte gekoppelde grootte, om een smallere deeltjesgrootteverdeling te verkrijgen. Wellicht het allerbelangrijkst is dat aerosol nanodeeltjes eenvoudig op of in een substraat afgezet kunnen worden, om zo een nanogestructureerd functioneel materiaal te vormen, dat de unieke grootteafhankelijke eigenschappen van de nanoschaal overbrengt naar de macroscopische wereld.

Dit proefschrift dekt twee aspecten van industriële toepasbaarheid van vonkverdamping: Is het schaalbaar, en is het nuttig? Het behandelt een werkend prototype van een in het tijdsdomein opgeschaalde generator, en het toepassen van met vonken gevormde deeltjes in nanogestructureerde, functionele materialen voor duurzame energie.

In hoofdstukken twee en drie wordt een opgeschaalde vonkgenerator gepresenteerd. De opschaalstrategie bestaat uit het verhogen van het aantal vonken per tijd, waarbij het typische korte, snel oscillerende gedrag van de vonk behouden blijft. Dit is bereikt door de spanning op de condensator los te koppelen van de doorslagspanning, met behulp van een serie van schakelaars. Het blijkt dat de gebruiksspanning van het systeem significant verlaagd kan worden, wat het gebruik van goedkopere componenten mogelijk maakt, door een 'gloeistroom' toe te passen.

De gloeistroom houdt lading vast in de vonkzone, zodat er altijd een overmaat van elektronen aanwezig is wanneer het elektrisch veld wordt opgelegd. Als de afstand tussen de elektrodes klein genoeg is, zorgt de hoge achterblijvende ruimtelading ervoor dat vonken vormen zonder tussenkomst van een voorontlading (*streamer*). Twee types gloeistroom zijn waargenomen: een quasi-stabiele gloei en herhaalde micro-ontladingen.

De maximaal haalbare herhalingsfrequentie is niet langer bepaald door de eigenschappen van het plasma, maar door het ontwerp van het elektronisch circuit en de thermische stabiliteit van de componenten. Het gebouwde prototype werkte stabiel bij een herhalingsfrequentie van 8 kHz, terwijl er gedurende korte tijd een maximum herhalingsfrequentie van 17 kHz is behaald. Bij hogere herhalingsfrequenties moet het debiet van koelgas proportioneel meegeschaald worden om te zorgen dat de elektrodes voldoende gekoeld worden. De productiesnelheid schaal linear met de verhoogde herhalingsfrequentie, terwijl de typische productmorfologie –agglomeraten van <10 nm primaire deeltjes– behouden blijft. Om lucht-gevoelige nanomaterialen te kunnen maken, moet de opstelling wel in een handschoenenkast worden ingebouwd.

Hoofdstuk 4 toont een aerosolaanpak voor het produceren van laagjes die oppervlakte-plasmonresonantie tonen. Door condensatie van een zilverdamp geproduceerde agglomeraten zijn gesinterd in een oven om  $\sim 100$  nm sferoiden te vormen, die vervolgens elektrostatisch zijn neergeslagen op zonnecellen van amorf silicium. De plasmonresonante deeltjes zijn effectieve lichtverstrooiers, die licht in de zonnecellen vangen. De werkzame doorsnede van de deeltjes is dusdanig groot dat een oppervlaktebedekking van 10 % voldoende is om de stroom bij belichting van de cel te verhogen.

De verstrooiingseigenschappen verslechteren door onzuiverheden in de deeltjes. Een deel van de vervuiling is afkomstig van de initiële dampbron, waar deze verdamp van de warme oppervlakten in de reactor. Door als dampbron in plaats van een buisoven een vonkgenerator, waarbij alleen het bronmateriaal verwarmd, toe te passen kan deze vorm van vervuiling met een ordegrrootte verlaagd worden. De tweede vorm van vervuiling vindt plaats bij blootstelling aan lucht, door de hoge reactiviteit van het oppervlak van nanodeeltjes. Op de zilverdeeltjes vormt zich een aanslag van  $\text{Ag}_2\text{S}$ , wat leidt tot een roodverschuiving van de plasmonresonantie en een verlaagde verstrooiingsintensiteit.

Naast de matige verstrooiing door de onzuiverheden in de deeltjes, hebben de zonnecellen matige elektrische eigenschappen. De lage spanning bij open circuit en de lage shuntweerstand tonen aan dat er defecten zijn ontstaan in de zonnecel. Hierdoor is er, ondanks de verhoogde stroom bij belichting, geen netto verbetering in de prestaties van de zonnecel. Naar verwachting kan er een significante verbetering behaald worden door blootstelling aan de buitenlucht te voorkomen, bij voorkeur door het nieuwe neerslagproces te integreren in het vacuumsysteem waar de zonnecellen geproduceerd worden.

Het gebruik van vonkverdamming om op magnesium gebaseerde waterstofopslagmaterialen te produceren staat beschreven in hoofdstukken vijf en zes.

Ten eerste is  $\text{MgH}_2$  gesynthetiseerd door vonkverdamping van Mg in mengsels van Ar met  $\text{H}_2$ . Magnesium hydride is stabiel bij kamertemperatuur, maar vormt niet door de langzame reactiekinetiek met moleculair waterstof. In de vonk worden waterstofmoleculen opgebroken tot atomair waterstof, wat de vorming van  $\text{MgH}_2$  nanodeeltjes tijdens het doven van het plasma mogelijk maakt. In vergelijking met vonkgeproduceerde Mg nanodeeltjes is de deeltjesgrootte iets kleiner. Het product bevat tot 4.3 % m/m waterstof; meer dan verwacht uit de met röntgendiffractie bepaalde  $\text{MgH}_2$  concentratie. Er wordt verondersteld dat de overmaat van waterstof aanwezig kan zijn als een amorf Mg-H fase, of in de vorm van een vaste oplossing.

Ten tweede is er een nanocomposiet van op Nb gebaseerde waterstofsplijtende katalysatoren in een matrix van Mg gevormd. Om diffusielimitatie binnen het metaalhydride te voorkomen, behoort de katalysator homogeen door het product verspreid te zijn. Door twee vonkgenerators in serie te plaatsen, worden de deeltjes die van beide vonken komen gemengd in verschillende stadia van hun groei. In dit geval vormen de katalysatordeeltjes zich in de aanwezigheid van Mg-agglomeraten met diameters van  $\sim 50$  nm. De katalysatordeeltjes en de Mg-agglomeraten agglomereren verder om zo een fractaalachtig composietproduct te vormen waar de verhouding Mg/Nb constant is op een schaal van 50 nm en groter, d.w.z. tot de grootte van het oorspronkelijke Mg agglomeraat. Echter, het wisselende elektrisch veld binnen de reactorkamer van de vonkgenerator leidt in combinatie met een ongedefinieerd stromingsveld tot onvoorspelbare elektrostatische verliezen, wat het ingewikkeld maakt om de algehele productsamenstelling te sturen.

Opmerkelijk is dat niobium oxide en magnesium metaal naast elkaar bestaan in het product, hoewel niobium oxide alsnog door Mg gereduceerd wordt na opwarmen of bij op- en ontladen van waterstof. Gezien dat de Mg vonk bovenstreams is geplaatst, en dat Mg sterk elektropositief is, zou men verwachten dat de vers gevormde Mg damp alle beschikbare zuurstof opneemt. De zuurstof in de niobiumoxides is afkomstig van de oxidelaag die zich bij blootstelling aan lucht op het oppervlak van de Nb elektrode had gevormd. Mettertijd is deze oxidelaag uitgeput, wat leidt tot een verschuiving naar metallisch Nb.

Hoofdstuk zeven beschrijft hoe aerosol nanodeeltjes bedekt kunnen worden met metalen in een vonkgenerator met holle elektrodes, door een proces dat conceptueel vergelijkbaar is met dat van hoofdstuk zes. Door de axiale configuratie worden de kerndeeltjes met diameters van een tiental nanometers dicht bij de bekleedende damp gebracht. Het neerslaan van de damp op de kerndeeltjes is beschreven met een bimodaal coagulatiemodel. Clusters van

de bekledende damp groeien en nemen deel in het bekledingsproces. Als deze clusters voldoende klein zijn, –in het geval van Ag en Au  $\sim 3$  nm– gedragen zij zich als een vloeistof, en kunnen ze over het oppervlak van het deeltje migreren. Deze clustergrootte beperkt de dikte van de deklaag die verkregen kan worden tot ongeveer 1 nm in een enkele stap, hoewel meerdere vonken in serie geplaatst zouden kunnen worden om dikkere deklaagen te verkrijgen.

Met goud, zilver, en polystyreenlatex is aangetoond dat de morfologie van de deklaag –gedispergeerde deeltjes, een kap, of volledig dekkend– afhankelijk is van de relatieve oppervlakte-energie van de beide materialen.

Veel toepassingen, waaronder de omzetting van zonne-energie, waterstofopslag, katalyse, batterijen, enzovoorts, worden beperkt door de eigenschappen van beschikbare materialen. Vonkverdamping produceert deeltjes die dusdanig klein zijn dat materiaaleigenschappen drastisch veranderen ten opzichte van de bulk. Via hun grootte, vorm, samenstelling en structuur kunnen we deze deeltjes afstemmen op specifieke functies, en vervolgens de verschillende deeltjes combineren om functionele materialen te ontwerpen. De nieuwe vonkgenerator maakt de bouwstenen direct uit de elementen, zonder vervuilende bijproducten, en in dusdanig grote hoeveelheden dat ze toegepast kunnen worden in reële toepassingen. De kracht van de techniek ligt in de flexibiliteit met betrekking tot zowel materiaalkeuze als de wijze waarop de bouwstenen gecombineerd worden, wat het een krachtig gereedschap maakt in het ontwerpen van materialen.



## Summary

Despite the obvious benefits of renewable energy, renewable sources make up only a small fraction of our current energy supply. Fossil fuels are convenient and still cheap, while each renewable energy strategy has its unique set of complications and technical challenges. A core issue for most renewable energy strategies lies in finding the right material. Often very specific mix of physical, mechanical, optical, electronic and/or magnetic properties is needed, and often the ideal material does not exist. Yet.

Considering that we cannot specialize, but must adopt a number of complementary strategies, a trial-and-error approach to finding the perfect material for each application is unattractive. Preferably, the desired material is engineered by combining building blocks with specific functions, to end up with a material with the right mix of properties. The engineering approach is especially attractive if these building blocks have at least one dimension as small as a few nanometers: At this size, at most a few tens of atoms thick, surface interactions play a dominant role, often resulting in a dramatic shift in material properties. Such an engineering approach benefits from flexible methods to produce its building blocks, nanoparticles, in a wide variety of compositions, shapes and sizes.

Spark discharge or spark ablation is a versatile method for generating nanoparticles in a continuous manner. A spark is a transient, high energy electric plasma with a core temperature of  $2 \times 10^4$  to  $6 \times 10^4$  K, and a lifetime of several microseconds. Because of the high temperature, any material can be ablated and evaporated down to its constituent atoms. Generally, conductive materials, in particular metals, are used. The short lifetime leads to rapid quenching of the ablated metal vapour cloud, resulting in the nucleation and growth of extremely small particles. Depending on the quenching conditions, an aerosol with a particle size ranging from a single atom to several tens of nanometers can be obtained. Spark ablation is in principle a physical process, where a bulk solid is reshaped into nanoparticles, using only electric

energy in an inert gas environment. As such it is an inherently green process, devoid of solvents and pollutant by-products.

In the aerosol phase, these nanoparticles can be manipulated and modified in a myriad of ways. Aerosol particles can be left to agglomerate, forming big, fluffy fractal-like structures which in turn can be reshaped to spheres; their surface can be modified, e.g. by chemical conversion or physical deposition of a coating material; they can be selected on their mobility, a size-dependent property, to obtain a more narrow size distribution. Perhaps most importantly, aerosol nanoparticles are readily deposited onto or into a substrate, to form a nanostructured functional material that transfers the unique size-dependent features of the nanoscale into the macroscopic world.

This dissertation covers two aspects of the industrial applicability of spark discharge: Is it scalable, and is it useful? A working prototype of a generator scaled in the time domain is presented, and the application of spark generated particles in nanostructured, functional materials for renewable energy is discussed.

In chapters two and three, a scaled up spark generator is presented. The scale-up strategy consists of increasing the number of sparks per time, while retaining the typical short, rapidly oscillating nature of the discharge. This was achieved by decoupling the capacitor voltage and discharge voltage, using a series of switches. It was found that the operating voltage of the system could be significantly reduced, allowing the use of cheaper components, by use of a 'glow' current. The glow current retains charge in the spark gap, so that an excess of seed electrons is always available when the electric field is applied. At sufficiently small gap spacings, the high residual space charge allows sparks to form without a preceding streamer. Two modes were observed for the glow current: a quasi-stable glow and repeated microdischarges.

The maximum attainable repetition rate is no longer determined by the plasma properties, but by the design of the electronic circuit and the thermal stability of the components. The assembled prototype was operated stably at a repetition rate of 8 kHz, although a maximum of 17 kHz was achieved in short-term operation. At higher repetition rates, the quench flow rate should be scaled proportionately to make sure the electrodes are cooled adequately. The production scales linearly with the increased repetition rate, while the typical product morphology –agglomerates of <10 nm primary particles– is retained. In order to produce air-sensitive nanomaterials, the setup still needs to be incorporated into a glove box.

Chapter four presents an aerosol approach for producing surface plasmon resonant films. Agglomerates produced by condensation of a silver vapour are sintered in a furnace to form  $\sim 100$  nm spheroids, which are deposited electrostatically on amorphous silicon solar cells. The plasmon resonant particles scatter light effectively, trapping light in the solar cells. Due to their large scattering cross sections a 10 % surface coverage is sufficient to give an increased photocurrent.

The scattering properties degrade due to impurities in the silver particles. Part of the contaminants originates from the initial vapour source, where they evaporate from the hot surfaces in the reactor. This form of contamination is reduced by an order of magnitude compared to a tube furnace if a spark, in which only the target material is heated, is used as the vapour source. The second type of contamination occurs upon air exposure, due to the high reactivity of nanoparticle surfaces. The particles tarnish to form  $\text{Ag}_2\text{S}$ , leading to a redshift of the surface plasmon resonance, and lower scatter intensity.

In addition to the poor scattering due to the particle impurities, the solar cells have a poor electrical performance. In particular, the low open circuit voltage and the low shunt resistance indicate that there are defects in the solar cell. Thus, despite the increased photocurrent, there is no improvement in overall solar cell performance. It is expected that a significant improvement can be made by avoiding air exposure, preferably by incorporating the new deposition process in the vacuum system used to deposit the solar cells.

The use of spark discharge to produce magnesium-based hydrogen storage materials is described in chapters five and six. First,  $\text{MgH}_2$  was synthesized by spark ablation of Mg in mixtures of Ar and  $\text{H}_2$ . Magnesium hydride is stable at room temperature, but does not form due to the slow reaction kinetics with molecular hydrogen. In the spark, molecular hydrogen is converted to atomic hydrogen, allowing  $\text{MgH}_2$  nanoparticles to form as the plasma quenches. Compared to spark-generated Mg, slightly smaller particle sizes are obtained. The product contains up to 4.3 % m/m hydrogen; more than expected from the concentration of  $\text{MgH}_2$  detected by XRD. It is hypothesized that the excess hydrogen is present as an amorphous Mg-H phase, or as a solid solution.

Secondly, a nanocomposite of Nb-based hydrogen splitting catalysts in a matrix of Mg was formed. To avoid diffusion limitations within the metal hydride, the catalyst should be distributed homogeneously throughout the product. By placing two spark generators in series, particles originating from both sparks are mixed at different stages in their growth. In this case, the catalyst nanoparticles form in the presence of  $\sim 50$  nm agglomerates of Mg. The

catalyst and Mg particles agglomerate further to form a fractal-like composite product where the ratio of Mg/Nb is constant down to a scale of 50 nm, i.e. the size of the original Mg agglomerate. However, the varying electric field inside the spark generator chamber combined with an undefined flow field result in unpredictable electrostatic losses, making it complicated to control the overall product composition.

Remarkably, niobium oxides and metallic magnesium were found to coexist in the product, although the niobium oxide is reduced by Mg upon heating or hydrogen cycling. Given that the Mg spark was placed upstream, and that Mg is strongly electropositive, one would expect the freshly ablated Mg vapour to scavenge all the available oxygen. The source of the oxygen that ended up in the niobium oxides was the native oxide layer that had formed on the Nb electrode surface. With time, this oxide layer was depleted, resulting in a shift towards metallic Nb.

Chapter seven describes how aerosol nanoparticles can be coated with metals using a hollow electrode spark, in a process conceptually similar to that of chapter six. Due to the axial configuration, the core particles with diameters of several tens of nanometers are brought into close proximity of the coating vapour. The deposition of the vapour on the core particles is described by a bimodal coagulation model. Clusters of the coating vapour grow and participate in the coating process. If these clusters are sufficiently small –in the case of Ag and Au  $\sim 3$  nm– they show liquid-like behaviour, and can migrate and coalesce across the particle surface. Because of this size limitation a coating thickness of about 1 nm can be obtained in a single pass, although multiple sparks could be placed in series to achieve thicker coatings.

Using gold, silver and polystyrene latex, it is demonstrated that the coating morphology –dispersed particles, capped or conformal– is dependent on the relative surface energies of both materials.

Many applications, including solar conversion, hydrogen storage, catalysis, batteries, etc., are constrained by the properties of available materials. Spark ablation produces particles in the size range where their material properties shift drastically from their bulk counterparts. Through their size, shape, composition and structure we can tune these particles to perform specific functions, and then combine the different particles to design functional materials. The new spark generator makes the building blocks directly from the elements, without wasteful by-products, and at large enough quantities to be useful in real applications. Its true strength lies in flexibility regarding both material choice and the way in which the building blocks are combined, making it a powerful tool in materials design.

# Acknowledgments

Ik ben voor de revolutie,  
ik ben van de partij.  
Met z'n allen moet het lukken,  
maar het antwoord komt niet van mij.

---

R. Schenk, *Revolutie!*

After some 180 pages we're finally approaching an end. Before we get there though, the next few pages provide the author with the opportunity to thank those behind the scenes that aren't mentioned on the cover, but were essential to the completion of this booklet.

While some of the following findings may have been accrued under rather unscientific circumstances, they are truths to the best of my knowledge.

First of all, I must acknowledge the concentrated storm of focus and determination that perhaps contributed more to this work than I did. Chapters 5 and 6 would not exist without my partner in crime in the hydrogen project.

**Anca**, I still remember walking into the battery office on my first day back at the TU. Your enthusiasm never left you, even when you tried to convince me it had. I am grateful it was you that took my samples into her care; not only did it lead to wonderful papers, both published and in preparation, but it was a constant reminder that my efforts were not in vain. All the best for you, Nina and Joost.

*Primus inter pares*, yet without equal.

**Andreas**, Our story goes back to 2002, where your subtle guidance in the TG design competition resulted in the winning design (and wet ears for the team). When I came to you for a masters project you let me work on atomic clusters in Christian's care – a pivotal experience that lit my love for research. In 2009, I had no choice but to accept your offer to come back to the TU

and scale up the spark. And now, while closing this chapter, we're opening a whole new can of worms.

Working with you has been a something of a challenge. The wildfire of ideas that came up in our conversations was staggering: this booklet captures only a handful of thousands, but not for lack of trying. In this storm of ideas I often felt adrift, albeit on your always calm and stable life raft. Thank you for your relentless kindness and support, for sharing your love for science, and for the Feuerzangenbohnen.

Dear Stephan, you always made time to discuss the hydrogen storage aspects of this work. Your feedback on various drafts was of great value to me. Thank you.

Dear Fokko, in addition to helping me understand  $\text{MgH}_2$  in context of hydrogen storage, you helped me out with an excursion to Li-ion batteries. While the result did not end up in this thesis, it did result in a strong project proposal. To be continued.

Dear Professor Kruis, dear Einar, thank you for giving research in spark- and arc-generated aerosols the push towards critical momentum through the BUONAPART-E project. It is an honour to have you as part of this defense.

Professor Deppert, Professor Mädler, and Professor Züttel, thank you finding time to review this dissertation, and for your willingness to participate in the committee.

Petra, it was a pleasure to share a glovebox with you. You provided me with insight in the fabled world of MOFs. Too bad we never found (the time for) a good synergy between the spark and your frameworks. Maria D., Hans and Roel, for your efforts in the hydrogen project.

Vincent and Nooshin, everything I've learned about the spark derives from the knowledge you shared with me. Your dissertations, now tattered and worn, have been my primary reference works, and never left my side. It still baffles me how such a simple system persistently remains both straightforward and complex. Thank you for sharing your passion.

Dear Paul, thank you for endless discussions on the opening and closing of switches, and the futility of driving a spark gap with a switch. The prototype you built, and –sadly often– repaired, allowed me to flesh out my ideas into chapters 2 and 3.

Rudi, Tim, Xin, Jorge, and Hairen thank you for your faith in aerosol technology. Your efforts resulted in chapter 4, and a new application area for the spark. You made it a pleasure to take yet another detour outside of chemistry.

Marco, your helping Puneet led to the wonderful particles of chapter 7. Your support in the lab, with problems on the blocks, and with good food will not be forgotten. Julien, thanks for being a sounding board, and the perfect excuse for barging into the battery office. Thank you both for helping me stare down the crowd today. Dear Phaedra, thank you for the wonderful cover art!

Jicheng, your involvement in the BUONAPART-E project was a daily reminder that my work was a mere stepping stone in the development of the spark. Thank you for your insights into Chinese culture; I hope I've done my part in sharing the highlights of the Dutch one with you. Anne, you provided the important physicists' perspective to stubborn engineers. Thanks! Kostis, with you around designing and building things becomes surprisingly easy. Thank you for taking care of our lab. Micha, for teaching me plasma physics for dummies/chemical engineers. Dirk, your visits were always inspirational, and it was a pleasure to share frikadellen with you. Thank you for providing insight into a legislators' perspective. Cem, Martine, Thijs, Remko, Rogerio, Puneet (and again Tim, Xin and Jorge), it was a pleasure be a part of your thesis works. To all my LO1 and LO2 students: I hope you enjoyed your spectacular results and setbacks as much as I did.

Christian P., your guidance (and dissertation) provided the basis on which I could write this booklet. David L., thank you for the outsider perspective on my work, and for being a voice of reason. All the best to you and the ladies. David M., your brief return to Delft did not receive the appreciation it deserved, but I learned a lot, for which I am eternally grateful. Good luck with Sicily... Mario, thank you for the advice, the Raman, and for returnig the favour in listening to dissertation woes.

Ben, Marcel, Piet, Joost, Herman, Kees, Ruben, Duco. You provided both insight in practical aspects of lab work, and a lot of support to me and my students. Ugo, Patricia, Louw, Maria M., Qiang, without whom I would have been blind. *De werkplaats – geen droom die Nico, Ronald, Alex, David, Rien en consorten niet konden verwezenlijken.* Alex, Erwin, Nico voor onuitputbare gasvoorraden.

First there was NSM. Dr. Picken (incl. Elektrisch Kabinet), for many suggestions in improving the spark. Gabriele, it was a pleasure helping you out with the WCPT conference. Thank you for your endless support and network. Eduardo, Haining, Klaas, Piotr, Plamen, Sasha, Stephan, Iftikhar, and many more, for discussions, and many shared borrels and lunches. Erik, Corrado,

Esteban, Miguel, Raphael, and the rest of the battery group; you were there for me whenever I needed a fresh perspective.

Then there was MECS. Dear Bernard, thank you for welcoming the particle people in your group. It is wonderful to see how people begin to realize what miracles are performed at the other sides of the coffee table(s). Wilson, contrary to your advice, I did do what you told me. Your comments on my MC proposal not only improved the document, but changed the way I approach the problem of funding. Peter, thank you for the discussions we had trying to get to grips with the concept of a ‘career’ in academia. Bartek, Christiaan, Diana, Digda, Fatwa, Hans, Kohta, Lennard, Moreno, Ruud, Wim, and many others for the cold and warm beverages (+ taart) with complementary discussions on matters of mind, soul and stomach. Aaike, ik kijk uit naar ons nieuwe avontuur. Dank voor de tips.

Wil, Karin, en Heleen (en de rest), jullie zijn de olie die ChemE draaiende houdt. En nog altijd blijven lachen ook. Dank voor alle hulp met de vele grote en kleine obstakels. Adrie, Ben, Marcel, Piet, Stefan K, Stephan H., en vele anderen met hen, voor de wetenschap dat één kop koffie toereikend is om welk maatschappelijk probleem dan ook op te lossen.

Adam, Christian H., Fiona, Martin, Kaiqi and Marc, for a memorable time in Cambridge. You provided me the perfect distraction to brace myself for the last (first) pages.

John, Nanne en Ramses, voor de uitlaatklep in het begin; David M. en Jan, voor het spinnen ertussenin; Iedereen bij DelftsBleau, voor de uitlaatklep aan het einde. José en Peter, voor gastvrijheid met hoog trendement.

James, Jennifer, Maddalena, Ale, Maria, Ivano, Valentina, Mauro, Paula, (e David M, Giusi, Luca), tutti grazie per mia casa lontano da casa.

John, Mary Jo, Chris, Fae, Devon, and everyone else across the pond. Thanks so much for your unconditional support and love. Oscar en Cynthia voor last-minute correcties. Onno, steun en toeverlaat in geval van nood. Iwona, dank voor de mentale steun, de tongetjes, het proeflezen, en alles eromheen.

Kate, it seems that soon we’ll have survived through two PhDs. I don’t have to tell you how helpful it is to have someone to share the confusion with. Thank you for providing a perfect balance between pressure, comfort and understanding.

!PAH!

# Curriculum Vitae

Tobias Vincent Pfeiffer was born on January 3<sup>rd</sup> 1980 in Neuchâtel, Switzerland. In 1997 he graduated Voorbereidend Wetenschappelijk Onderwijs (VWO) at Gymnasium Haganum in the Hague, the Netherlands.

He obtained his BSc in Chemical Engineering at the Department of Chemical Engineering of the Applied Sciences faculty of Delft University of Technology. At the same Department he obtained his ir./MSc in Chemical Engineering in 2007, specializing in particle technology.

From 2007 to 2009 he worked as a process engineer at OctoPlus Technologies, an SME pharmaceutical company based in Leiden, the Netherlands, on scaling up a production process for controlled release medication.

In 2009 he started his PhD research at Delft University of Technology under the guidance of Prof. Andreas Schmidt-Ott, on scaling up the spark discharge process for energy conversion and storage applications, resulting in the booklet before you.



## Peer reviewed publications

- **T. V. Pfeiffer**, J. Ortiz-Gonzalez, R. Santbergen, H. Tan, A. Schmidt-Ott, M. Zeman, A. H. M. Smets “Plasmonic nanoparticle films for solar cell applications fabricated by size-selective aerosol deposition” *Energy Procedia*, accepted.
- **T. V. Pfeiffer**, J. Feng, and A. Schmidt-Ott “*New developments in spark production of nanoparticles*” *Advanced Powder Technology* 25: (2014), 56–70 DOI: 10.1016/j.appt. 2013.12.005
- A. Anastasopol, **T. V. Pfeiffer**, J. Middlekoop, U. Lafont, R. J. Canales-Perez, A. Schmidt-Ott, F. M. Mulder and S. W. H. Eijt “Reduced Enthalpy of Metal Hydride Formation for Mg–Ti Nanocomposites Produced by Spark Discharge Generation” (2013) *Journal of the American Chemical Society* 135:7891-7900, DOI: 10.1063/1.3659315.

- A. Anastasopol, **T. V. Pfeiffer**, A. Schmidt-Ott, F. M. Mulder and S. W. H. Eijt  
“Fractal disperse hydrogen sorption kinetics in spark discharge generated  
Mg/NbO<sub>x</sub> and Mg/Pd nanocomposites” (2011) *Applied Physics Letters* 99:194103  
DOI: 10.1063/1.3659315.

## Patents

- WO/2013/115644 “*Spark Ablation Device*” A. Schmidt-Ott and T. V. Pfeiffer (2013).